Advanced Logging Investigations of Aquifers iN Coastal Environments

ANNUAL SCIENTIFIC REPORT
Year 3 (2004)

May 5, 2005

Consortium Co-ordinator:
Dr. Pezard Philippe
(ISTEEM - CNRS, Montpellier, FRANCE)

Web: *http://www.isteem.univ-montp2.fr/LGHF/water/ALIANCE/index.html*

Advanced **L**ogging **I**nvestigations of **A**quifers i**N** **C**oastal **E**nvironments

European Commission Programme:

"Energy, Environment and Sustainable Development"

Water Key Action: Contract N° - EKV-2001-00039

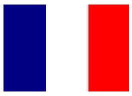

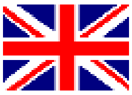

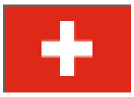

LIST OF ALIANCE CONTRIBUTORS

ALIANCE is co-ordinated by ISTEEM, CNRS - UNIVERSITÉ MONTPELLIER 2, FRANCE

P. A. Pezard, P. Gouze, D. Mainprice, G. Lods, R. Leprovost, S. Barry, G. Henry, T. Poidras, J.L. Seidel, A. Belghoul, Y. Maria-Sube, B. Marie
Institut des Sciences de la Terre, de l'Eau et de l'Espace de Montpellier (ISTEEM)
CC 56, Place Eugène Bataillon, 34 095 Montpellier cedex 05, France
e-mail : pezard@dstu.univ-montp2.fr

S. Löw, N. Van Meir, M. Herfort, D. Jaeggi
Engineering Geology - ETH Hönggerberg
CH-8093 Zürich, Switzerland
e-mail : simon.loew@erdw.ethz.ch

M. Riley, R. Greswell, P. Ellis, B. Isakov, R. Mackay
The School of Earth Sciences, The University of Birmingham
Edgbaston, Birmingham B15 2TT, UK
e-mail : m.riley@bham.ac.uk

M. Montoto, F. Mateos, R.-M. Esbert, A. Martinez
Facultad de Geología, Departamento de Geología
Area de Petrología y Geoquímica, Campus de Llamaquique
Jesús Arias de Velasco, 33005 Oviedo, Espana
e-mail : montoto@asturias.geol.uniovi.es

J.-L. Deltombe, A. Henriette, P. Cleaver; B. Legros
Advanced Logic Technology (ALT) sarl
Bât. A, Route de Niederpallen, L-8506 Redange-sur-Attert, Grand Duché du Luxembourg
e-mail : jean-luc.deltombe@alt.lu

J.-P. Sessarego, M. Francius, R. Guillermin
Laboratoire de Mécanique et d'Acoustique
31 Ch Joseph Aiguier, 13402 Marseille cedex 20, France
e-mail : sessarego@lma.cnrs-mrs.fr

P. Broun, J.-P. Martin, J.-M. Fedele, R. Dovis
GeoEnergy
19 Route de Paris, 27100 Le Vaudreuil, France
e-mail : philippe.broun@geoenergy.fr

Contents


a


b


c

To the right: Field set-up for hydrogeophysical testing constructed at CNRS and the University of Montpellier, in the framework of ALIANCE WP5. (a) Surface injection/pumping unit designed for push-pull hydrodynamic experiments with the CoFIS downhole tool, and equiped with several containers for tracer injection downhole, between packers, in a controled manner. (b) Modified logging vehicle for the safe assembly and downhole deployment of CoFIS. (c) Elements of CoFIS, the new downhole sonde for controled push-pull experiments in boreholes. Photos "a" & "b" shot at the Stang-Er-Brun site in Ploemeur (March 2005), and "c" in the Lavalette workshop (Montpellier), where CoFIS and the pumping unit were assembled and tested (December 2004).

1. PROJECT SUMMARY

Background

Over 50 % of the accessible water at or near the Earth surface is over-exploited due to human activities. Groundwater is particularly at risk in urban or semi-arid areas, with the maximum danger in coastal zones where more than 60% of the world population is concentrated. As the main source of drinking water, this strategic but vulnerable resource is of utmost importance.

The overall objective of this research is to improve groundwater sustainability and quality in coastal and semi-arid environments. For this, the aim of ALIANCE is to develop, integrate and assess a set of new geophysical tools, methods and scientific approaches to obtain an improved description of aquifer and fluid parameters in the subsurface. The cornerstone of ALIANCE is the setting-up of in-situ facilities for experimentation and long-term monitoring. The European community includes a large number of potentially exposed coastal aquifers due to over-exploiting and/or natural drought, especially in the Mediterranean region (SALTRANS project). The mitigation of seawater encroachment has thus become a key issue as, for example, the salinity of groundwater often exceeds drinking water standards, and eventually threatens long-term agricultural use. We propose here to study an intruding saline wedge from changes in space and time of pressure and electrical fields.

The slow renewal of groundwater, especially in semi-arid regions, enhances the need for long-term management tools. In order to mitigate the risks of long-lasting pollution or over-abstracting in such exposed aquifers, it is necessary to improve the exploration and monitoring methods to describe aquifer characteristics and fluid flow dynamics. Such improvements are also needed to develop, test and validate new theoretical and numerical models which are, in turn, necessary to assess aquifer vulnerability or groundwater sustainability and quality. The development of integrated approaches is requested to link exploration, monitoring, modelling and management facilities. In conjunction with the present effort realised to improve theoretical approaches and quantitative modelling, ALIANCE intends to focus on the improvement of aquifer characterisation and long-term monitoring.

In short, ALIANCE will develop and assess for end-users an integrated set of geophysical and hydrogeological tools and methods. Groundwater resources management and mitigation of long-lasting pollution risks, with a special attention to saltwater intrusion issues will be the main objectives of the research. For this, ALIANCE proposes to create in-situ experimental facilities, new downhole sensors yielding a far more precise in-situ fluid flow and transport description, and to test a new monitoring set-up. A cost-effective, rapidly deployed expert approach usable by industry or districts will be produced to merge multi-scale, multi-methods, and site-specific data into modelling procedures.

Problem to be solved
Salt intrusion in coastal aquifers, either from natural or anthropogenic source, is often related to over-drafting due to agricultural use, or a high density of population, or the effect of droughts in arid regions. While the physical processes associated with salt water intrusion are still being discussed, more field data are needed to assess the predictive models developed for long-term management and vulnerability assessment of groundwater resources in this context. This research focuses on the development of new geophysical logging, hydrological testing and long-term monitoring methods to describe and monitor saline intrusion processes.

Scientific objectives and approach
In order to mitigate the risks of saline water intrusion in coastal aquifers, an integrated, multi-scalar hydrogeological characterisation of subsurface structures and dynamics is required. The objective of ALIANCE is to develop a strategy for the quantitative description of fluid flow and storage in the shallow subsurface. A site-specific, detailed but cost-effective protocol will be implemented, leading to a site modeling capability associated with long-term monitoring from pressure and electrical fields. This includes state-of-the-art geological, geochemical, petrophysical, geophysical logging and hydrological methods, and the design of 5 new downhole sensors yielding new data for model validation. Two end-member sites in terms of hydrogeological behavior will be set up for long-term experimentation, the testing of the new tools, and the validation of site-specific experimental and modelling protocols from µm- to 100 m-scale. Active in-situ testing from short- and longer-term injections with variable salinity fluids will simulate over-drafting or saline water intrusion. In addition to pressure and fluid electrical conductivity, the electro-hydraulic coupling principle will be used to characterise and monitor water/brine hydrodynamics.

Expected impacts
ALIANCE aims to improve the long-term management of brine intrusion in coastal aquifers from detailed field description and hydro-electrical monitoring. The research will provide (1) a new geophysical and hydrological protocol to characterize shallow aquifers in an integrated manner, (2) new logging and testing sensors to investigate shallow aquifers, (3) geophysical and hydrological data at 2 end-member sites to validate existing numerical codes, (4) a test for new in-situ monitoring techniques of salt water intrusion in coastal aquifers.

Work plan structure
In order to achieve these goals, the work plan is built in ten, closely inter-related Work Packages (WP1-10). Several "End User – Water Authorities" are involved in both "advisory" and "client" capacities throughout all phases of the proposed research, particularly to assist with initial aspects of the studies (problem formulation), and with integrative (methodology development) phases of the proposed research.

2. OVERVIEW OF SCIENTIFIC PROGRESS

Work Package Number 1 :
Experimental Site (EXS) characterisation and drilling

Objectives and input to work package :

(a) EXPERIMENTAL SITE (EXS) identification, in a fresh granitic setting,
(b) Geological and geophysical site characterization
(c) Choice of the drilling/coring location for 2 to 4 holes, depending on pre-existing holes
(d) Site-dependent protocol for fluid sampling, geophysical logging, flow and tracing experiments, as well as traditional long-term monitoring.

Summary of work completed as part of Workpackage 1

The ALIANCE experimental Site (EXS) was chosen as part of the requested clustering effort with the SALTRANS project, also funded by the EC under the 5th framework program. The Ploemeur basement site (Southern Brittany, France; Figure 1) of SALTRANS was chosen as it was corresponding to the ALIANCE specifications for the Experimental Site (EXS).

Tasks 1.1, 1.2, 1.3 and 1.5 have been fully completed. Task 1.4 has been started, but will not be completed until Phase II of the fieldwork programme has been finished. Milestones M1.1, M1.2, M1.3 and M1.4 have been reached.

Deliverable D1.1 has been submitted, and includes the database on the boreholes and core, which was originally scheduled to be part of deliverable D1.2. This database is now included as part of the H+ database by "MEDIAS France" in Toulouse, a partner of CNRS. This database will be accessible to all scientists in Europe on year after the end of the project. The remainder of D1.2 cannot be delivered until monitoring is complete, which will not be until near the end of the project.

Overview

The EXS is located (Figure 1) in the city of Ploemeur (Morbihan), a few kilometers to the West of the major port town of Lorient (47°44′N 03°28′W, UTM (WGS84) 464410E 5287510N). The site lies 1.5 km from the coast and 2.0 km to the west of the city center (Figure 1). Groundwater abstraction is important for the local drinking water supply. The work undertaken is documented in details in the site geological report. The city of Ploemeur sits on granitic body bounded to the North by low angle normal fault (Touchard, 1998), with schist on the hanging wall. The "EXS" experimental site was located in the vicinity of an existing borehole (F22), and close to the granite-schist regional faulted boundary that might constitute part of the reservoir from which the city of Ploemeur is supplied with water.

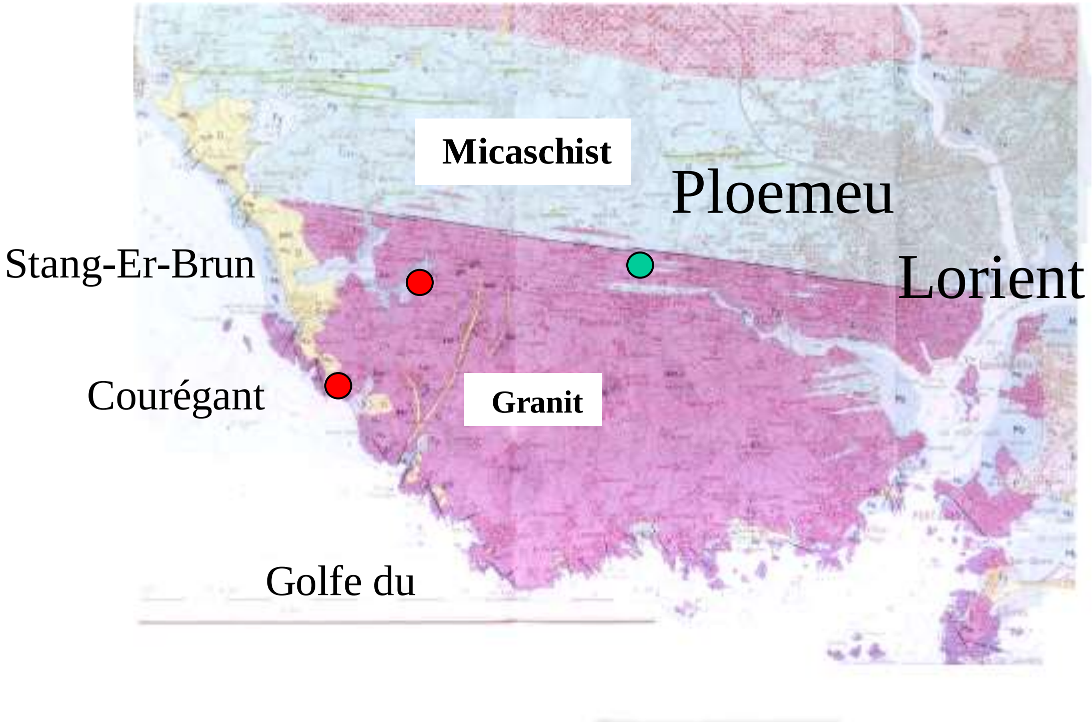

Figure 1. Location of Ploemeur, near Lorient, on the south coast of Brittany (France), with that of the Stang-er-Brune experimental site.

The Stang Er Brune drillsite covers an area of 10 by 40 metres in a stand of old deciduous wood and between open fields under pasture. Access is via an unpaved road between Kervinio and Lannénec. The nearest habitation is 500 metres away. There is no outcrop immediately at the site, but there is an existing borehole (F22) 35m away to the south (drilled by the commune in 1991) and a small abandoned quarry for granite building stone another 60m away, also to the south.

The experimental array comprises one wire-line cored 83.8 m borehole, two 100 m boreholes drilled using a down-the-hole hammer (diameter 105 mm), and three 10 m deep piezometers (Figure 5b). The shallow piezometers were cased with PVC tube (126/140 mm ID/OD) and cemented down to ~3 m through the soil and regolith zone, the deeper holes were cased and cemented to the base of the weathered zone (~23 m). A thin cover of soil (<0.5m) and regolith (<2m) covers mica schist overling the Ploemeur Granite at a depth of about 40 metres (Figure 2). There appears to be a contact between the two lithologies dipping at 41° in the direction of 001° calculated from borehole intersection elevations, including F22. The schist is well foliated dipping at 30°-50° in the direction 270-330° magnetic and contains minor folds. Foliation in the granite is difficult to see in the optical logs but core log data indicate dips ranging between 40-50°. The schist contains several narrow intrusions of pegmatite and more medium grained granitic material.

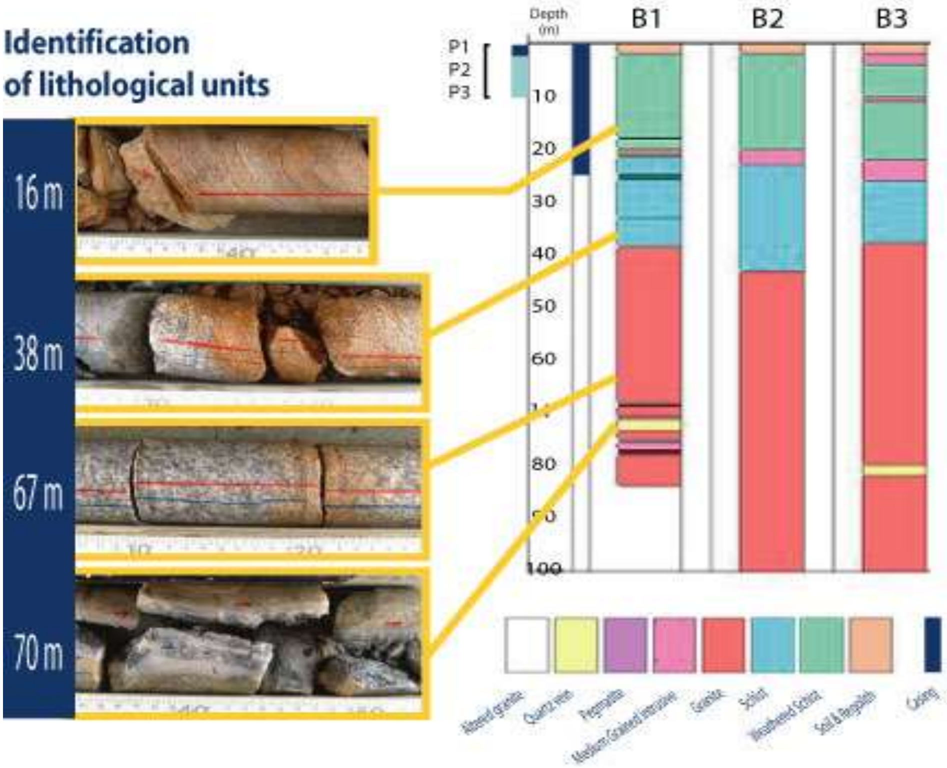

Figure 2. Geological log of B1 (left), B2 (middle) and B3 (right) holes deduced from core analyses (B1) and borehole wall geophysical images (B2, B3), after calibration in B1.

Filled and open fractures have been identified in the diamond drill core, with apertures generally on the sub-millimetre scale, but with the hydrothermal veins having apertures between 1 and 8 mm. Fracture fill includes iron oxide, clay, quartz and chlorite. The geophysical optical and acoustic logs indicates fairly well-defined fracture sets within the granite and schist and shows differences between two main dip directions, varying from 300° in the schist to 285° in the granite. In the granite there are at least two well-defined fracture sets, and a third set with a wider spread. In general the major fractures in the granite and unweathered schist have a frequency of 1-2 per metre with some increase at the granite-schist contact and adjacent to the hydrothermal veins.

During drilling operations, the handling and geological description of cores from B1 was undertaken by Partner 2 for B1 at the EXS and Partner 1 for D2 at the coast. Following coring operations, the core was taken to the repository of the University of Rennes, in charge of the Ploemeur site development as part of SALTRANS. Rock samples have been chosen for laboratory experiments as part of WP4 by partners 1, 2 and 4. No further development of the EXS was undertaken in 2004, waiting for the final experiments in 2005, as part of WP3 and WP5. As for all cores taken within ALIANCE, sections sampled for experiments have been split into :

- a working half, mostly for petrophysical experiments,
- a working quater mostly for petrological investigations such as thin sections,
- an archive quater to serve as geological reference and that should never be touched.

Work Package Number 2 :
SWS characterisation and drilling

Objectives and input to work package :

(a) SALINE WEDGE SITE (SWS) identification in a lithified and fractured sedimentary coastal aquifer, with a well documented history of brine intrusion,
(b) Geological and geophysical site characterization,
(c) Choice of the drilling/coring location for 5 to 8 holes, depending on lateral connectivity, core characterization strategy and pre-existing data,
(d) Site-dependent protocol for fluid sampling, borehole logging, flow and tracing experiments, and traditional site monitoring.

Summary of work completed as part of Workpackage 2 (WP2)

The ALIANCE SaltWater Site (SWS) was chosen as part of the requested clustering effort with the SALTRANS project, also funded by the EC under the 5th framework program. The Mallorca basement site of SALTRANS near Pollenca was chosen as it was corresponding to the ALIANCE specifications for the Salt Water Site (SWS).

Tasks 2.1, 2.2, 2.3 and 2.5 have been fully completed. Task 2.4 has been started, but will not be completed until Phase II of the fieldwork programme has been finished. Milestones M2.1, M2.2, M2.3 and M2.4 have been reached.

Deliverable D2.1 has been submitted, and includes the database on the boreholes and core, which was originally scheduled to be part of deliverable D2.2. This database is now included as part of the H+ database by "MEDIAS France" in Toulouse, a partner of CNRS. This database will be accessible to all scientists in Europe on year after the end of the project. The remainder of D2.2 cannot be delivered until monitoring is complete, which will not be until nearer the end of the project.

Overview

Saline water intrusions into fresh water layers are significant problems in densely populated coastal areas. To initiate appropriate mitigation measures, detailed knowledge of the hydrogeological settings is required. Of particular interest is the distribution of salt water, fresh water and preferential flow paths and the response of the hydrological system to artificial and/or natural disturbances.

These key issues are currently being addressed in the framework of this interdisciplinary European Commission project. Its main objective is to develop a strategy for the quantitative analysis and description of fluid flow and salt transport in coastal aquifers. For this purpose, a test site located in the southwestern part of Mallorca (the Campos Saline Water Site, or "SWS") has been selected and fully developed in 2003. The test site is located about 6 kilometers inland (Figure 3) and extends over an area of approximately 100 x 100 m^2. Based on information provided by several ~100 m deep boreholes, the main lithofacies units have been delineated. This typical reefal stratigraphy is exposed along kilometers of steep cliffs at

Cabo Blanco (Figure 4), 15 km to the west of the Ses Sitjoles site, with lagoonal structures on the top, core reef in the middle, and slope deposits at the base. The groundwater table lies at a depth of ~ 37 m, which corresponds to about 1 meter above sea level at the coast. Fresh water is found within the upper 20 m. Sandwiched between the fresh water and saltwater layers is a ~ 10 to ~15 m thick mixing zone.

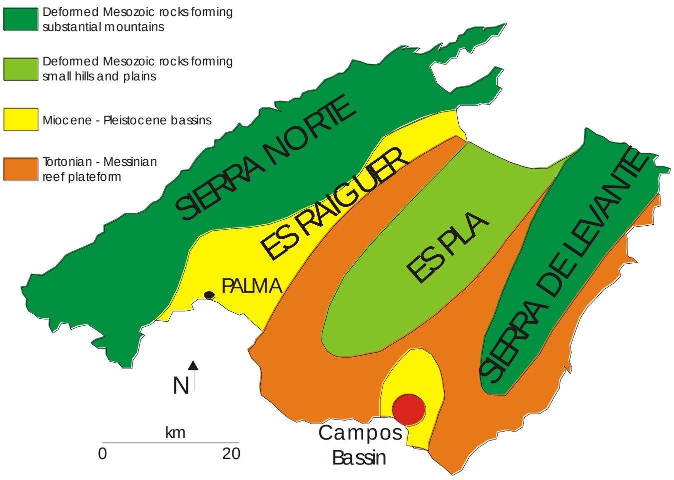

Figure 3. Approximative location of the Ses Sitjoles experimental site near Campos, within the Llucmajor Miocene reefal platform (Mallorca).

At the SWS and in summary, 5 boreholes MC1 to MC5 (Figure 5) have been fully cored, mostly with a core diameter of 84 mm and depths ranging between 100 and 102 m. Cored drillings at Ses Sitjoles yielded in general good core recovery for MC2-MC5 between 86 and 94% except for MC1 with only 33%. Core losses can be explained in most cases by karstic cavities or poorly cemented material, phenomenon which have been recorded in all boreholes. Poor core recovery in MC1 is due to inadequate drilling technology. Numerous surveys including downhole geophysical and hydrochemical logging, seismic cross-hole experiments and hydraulic monitoring have been carried out in 2003, and completed in 2004 as part of WP3 and WP9.

Figure 4. Cliff at Cabo Blanco (Mallorca), where an entire sequence such as that drilled near Campos by ALIANCE is exposed with: lagoonal structures at the top, the reef core in the middle (orange in colour), and slope deposits (white in colour) at the base.

For geological interpretation, upconing experiments, as well as cross-hole hydrogeophysical experiments as part of WP3 and WP5, a set of 4 additional boreholes was drilled in a destructive manner. In all, the spacing between individual boreholes ranges from 5 to 90 m. The boreholes were found unstable to variable degrees in the upper 50 to 60 meters. Those dedicated to upconing experiment had to be over-drilled with a larger diameter in order to install a PVC casing in the upper borehole section. This casing was full PVC in the unsaturated zone, and slotted below. Three holes (MC2, MC8 and MC9), stable since drilling and with 5 m spacing between them, were left open for crosshole hydrogeophysical experiments.

From top to bottom, the main lithofacies types, are the lagoonal sequences, the reef core, then the proximal and distal slope, all encountered at Ses Sitjoles in the first one hundred meters. They have been recognized in all cored boreholes, however, their thickness and depth varies considerably. During drilling operations, the handling and geological description of cores from MC1 to MC5 was undertaken by Partner 3 for all holes from the Campos SWS. Following coring operations, the core was stored for the duration of the project in a government workshop in Sa Pobla (in the northern part of Mallorca), where the cores were sampled for experiments in the different laboratories.

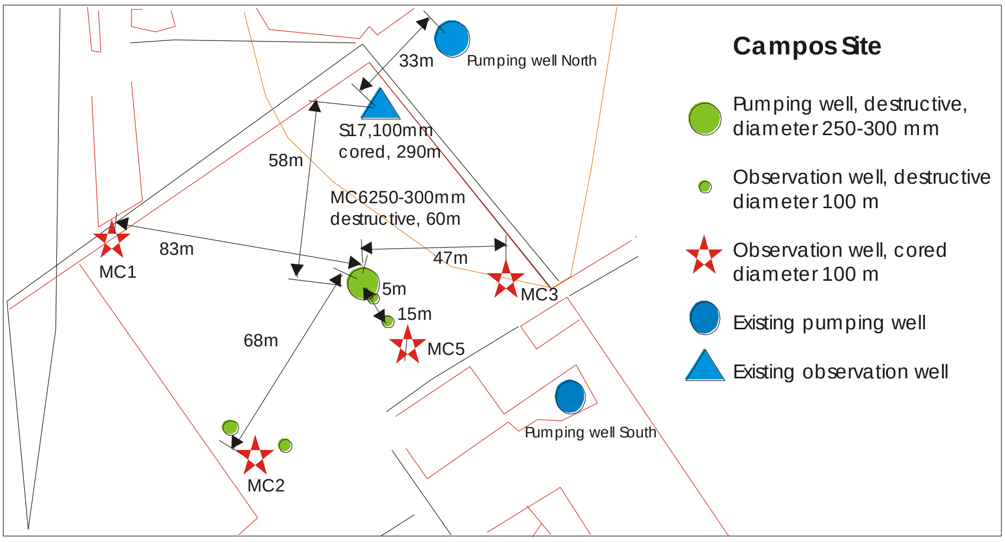

Figure 5. Map of the SWS experimental site at Ses Sitjoles near Campos (Mallorca). In all, a total of 9 holes has been drilled, five of them fully cored.

With MC1, MC2, MC3, MC4 and MC5 fully cored, it was decided to concentrate most core experiements as part of WP4 on one of the holes. MC2 was chosen due to the stability of the section and the completeness of downhole experiments obtained in this hole. As for all cores taken within ALIANCE, sections sampled for experiments have been split into:

- a working half, mostly for petrophysical experiments,
- a working quater, mostly for petrological investigations such as thin sections,
- an archive quater, that should not be touched in order to serve as geological reference for future studies.

Rock samples have subsequently been chosen for experiments as part of WP4 by partners 1, 2 and 4. Cores from MC3 and MC5 were tranfered in 2004 and are now stored by partner 3. Cores from MC2 and MC4 will be transfered to Montpellier for permanent storing in 2005. Additional work on core from MC3 and MC5 has been conducted by partner 3 in Zurich.

Partners 1 (ISTEEM – Montpellier - France)

In order to investigate the evolution of the carbonate reef since emplacement in terms of past flooding conditions, the core from MC2 was used to identify and analyze mineralized horizons. In relation to CNRS at the University of Aix-Marseille (France), Sr isotopes ages were measured from a few samples taken along the Cabo Blanco cliff, and along MC2. While the reef and lagoon at Cabo Blanco were found to be, as expected, of Messinian age (Pomar, 1993; Pomar et al., 1995), only the upper part of the MC2 sequence was found to be contemporaneous to that sampled at the cliff. Below 35 m depth, ages in excess of 17 Ma were measured. This corresponds to Seravallian Miocene ages which is known to be, as for the Messinian, a period of hot climate and high sea level. This result considerably changes the geological history of the island of Mallorca, as well as that of reefal platform development in the Mediterranean. While the lateral extension of the Seravallian platform is presently unknown, this result could have a significant influence on the processes of deep salt water intrusion into the island.

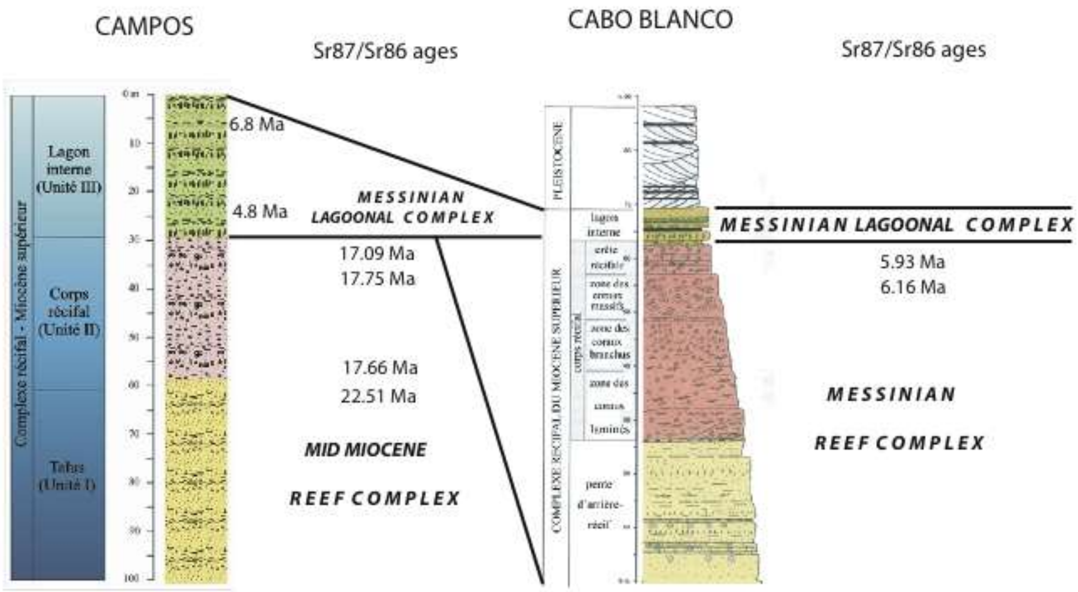

Figure 6. Stratigraphic and diachronic relationships between sequences exposed at Capo Blanco and drilled by ALIANCE near Campos (Mallorca).

Partners 3 (ETH – Zurich - Switzerland)

Geophysical investivation at a 100 m-scale

Main objectives of geophysical testing included detailed characterization of the lithological parameters that are relevant for saltwater intrusions in freshwater aquifers. These parameters can be determined with a combined application of seismic and electrical methods. For that purpose, a variety of seismic and electrical experiments were performed in 2003 at the Campos (Ses Sitjoles) test site. Seismic tomography was applied between boreholes MC1 and MC2, and MC5 and MC2, and geoelectrical data were collected in MC1, MC2, MC3, MC4 and MC5 (Figure 1). Initial processing revealed that both seismic and geoelectrical data provide useful subsurface information. In particular, small-scale variations of the lithology and variations of the salinity could be determined. It was therefore decided to complement this data sets with additional seismic and geoelectrical cross-hole experiments in 2004.

The experiments were performed in April 2004. Seismic cross-hole data were recorded with borehole pairs MC5-MC4, MC4-MC7, MC5-MC7, MC3-MC5, MC3-MC4 and MC3-MC7 (Figure 7). Geoelectrical cross-hole data were acquired with borehole pairs MC5-MC4, MC5-MC3 and MC3-MC4. Tomographic inversions of the traveltimes were performed using a non-linear algorithm that employed a finite-difference eikonal equation solver and an efficient sparse matrix inversion algorithm (LSQR). Both damping and smoothing constraints were applied to account for the underdetermined component of the inverse problem. The results are displayed in Figure 8. Background velocities are of the order of 2500 m/s. Between 10 and 25 m bsl, a band of high velocities is observed, with values varying between 3000 and more than 4000 m/s. The internal structure of the high-velocity zone is quite variable, particularly in the tomographic plane MC5-MC4-MC7, where pronounced lateral changes are evident. It is likely that such strong heterogeneities are the results of 3D effects; the waves may have traveled slightly outside of the tomographic planes.

Processing of the geoelectrical cross-hole data is still in progress, but in the mean-time a more detailed analysis of the single-hole data collected in 2003 was performed. Using a single-hole tomography technique, electrical resistivities were determined as a function of depth and borehole distance. The resulting tomograms, depicted in Figure 9, indicate the transition from fresh- to salt water between 20 and 30 m depth b.s.l.. Moreover, significant variations in the freshwater domain can be recognized.

To check the reliability of the single-hole tomograms, the results were compared with EM induction logging data, with an example provided here for MC5 (Figure 10). There is a remarkable match between the two.Resistivity-depth functions were extracted from the tomograms at a distance of 0.64 m from the boreholes. This corresponds roughly to the average penetration depth of the induction resistivity tool. Combined interpretation of electrical conductivities obtained from geoelectrical experiments and results from the fluid resisitivity logs, allows porosity values of the formation to be estimated. Again, borehole MC5 is used to illustrate the procedure. The resistivity-depth function (Figure 10b), the fluid log (Figure 10c), and Archie’s law were combined to derive a porosity-depth function (Figure 10d). The methodology was also applied to the entire tomogram, which resulted in the porosity tomogram in Figure 10e. It indicates, as to whether high-porosity zones are confined to the vicinity of the borehole, or if they extend over larger distances.

Conclusions and outlook

Preliminary analysis of seismic and geolectrical borehole measurements has yielded critical information for appropriate characterization of a coastal acquifer. Future work will focus on joint quantitative analyses of crosshole seismic and crosshole geoelectric data to obtain 2D distributions of porosity and permeability, with which meaningful hydraulic flow models can be established. For that purpose the geoelectrical cross-hole tomograms, which will be finalized soon, may contribute valuable information.

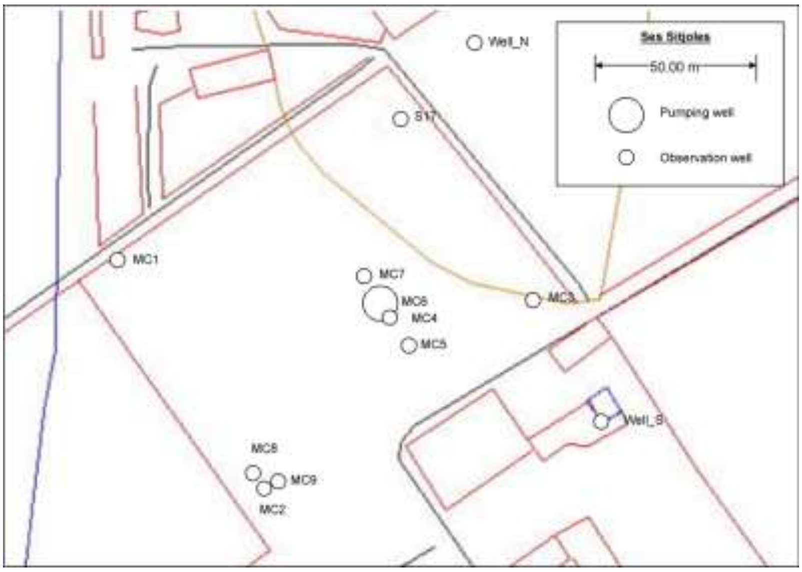

Figure 7. Borehole distribution at the Campos (Ses Sitjoles) test site.

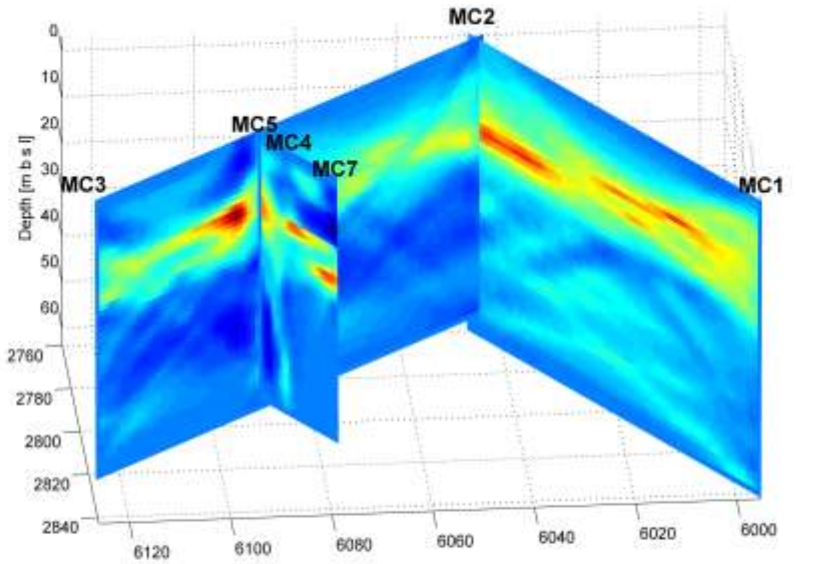

a

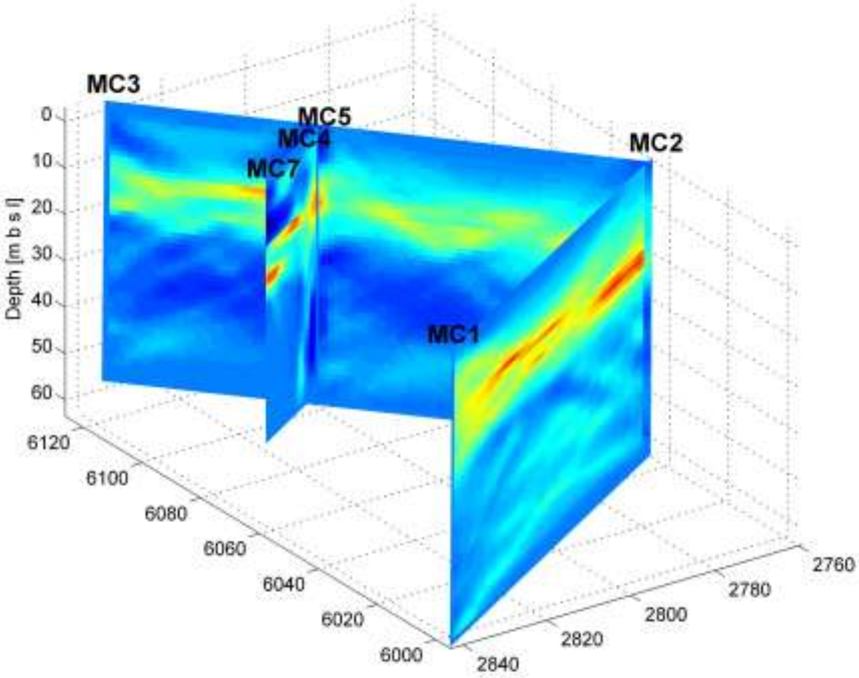

b

Figure 8. Tomographic images obtained from seismic travel time data. The diagrams show the same data from two different view angles.

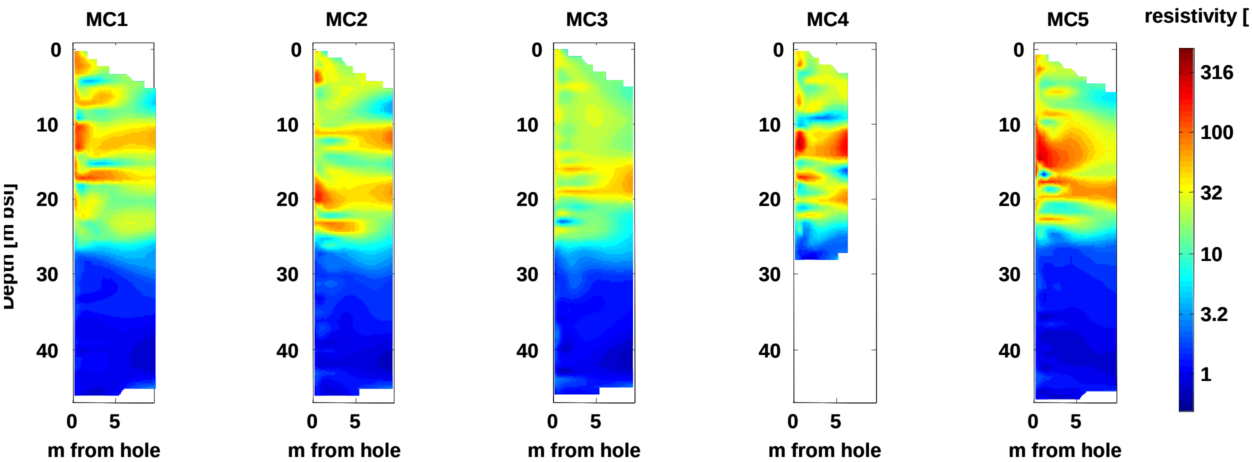

Figure 9. Electrical single-hole tomograms in the five core holes from Ses Sitjoles.

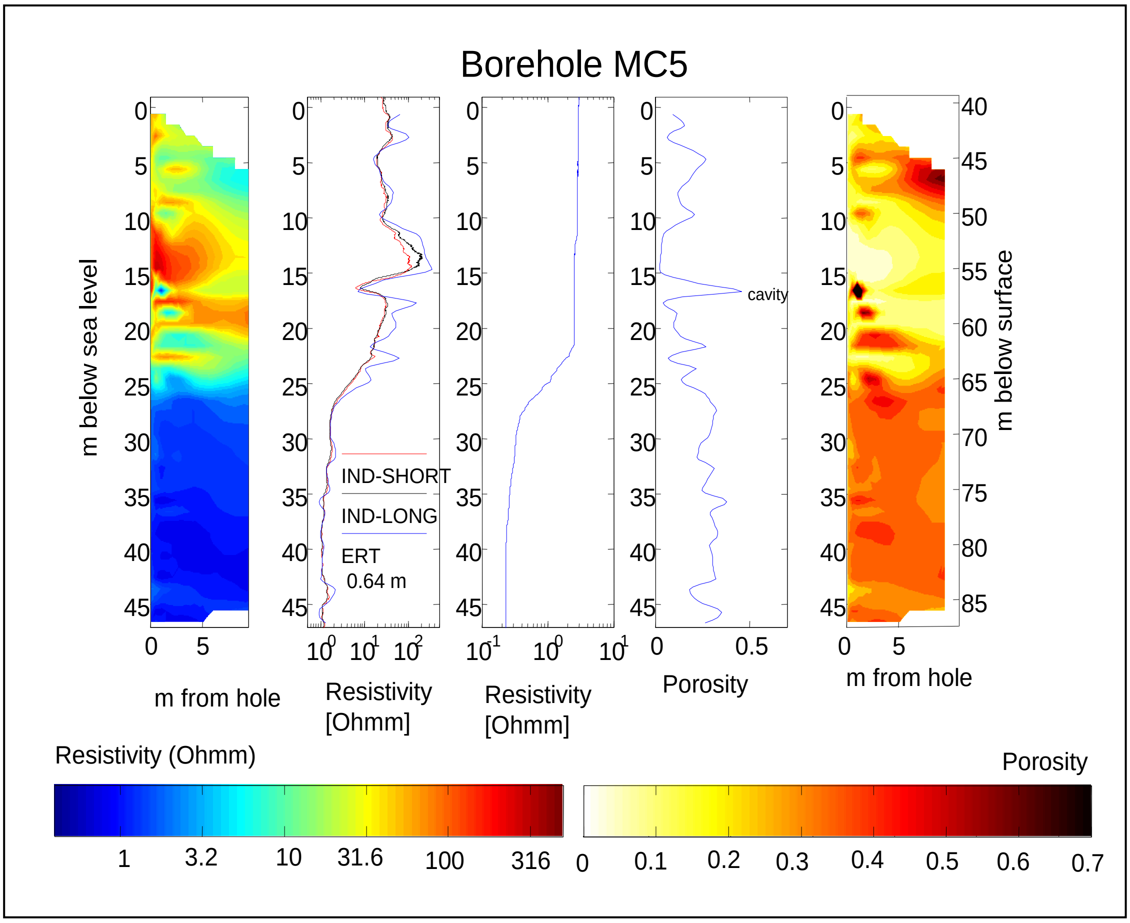

Figure 10. Determination of porosity from single-hole tomograms. a) Original tomogram. b) Comparison of tomogram values with results from induction logging. c) Fluid resistivity log. d) Porosity-depth function determined with b), c) and Archie's law. e) Porosity tomogram obtained with a) and c).

Work Package Number: 3
Logging and testing (both sites)

Objectives and input to work package :

(a) Detailed description of the structure, geometry and petrophysical characteristics in each of the boreholes at the EXS and SWS,

(b) Hydrodynamic and hydrodispersive properties (from cm- to 100 m-scale),

(c) Validation of the new geophysical logging/hydrodynamic testing tools,

(d) Setting up of a comprehensive but cost-effective protocol for the investigation, from borehole logging and testing, of brine polluted aquifers.

Summary of work completed for Workpackage 3 (WP3)

The fieldwork for Tasks 3.1 and 3.2 as defined in the DoW of ALIANCE has been completed. For both sites, analysis of the results was a current activity throughout 2004. Also, additional data were recorded at the SWS in Campos (Mallorca) in order to improve the quality and completenes of the dataset. This field campaign was dictated by the necessity to record a full set of data in the two new holes (MC8 and MC9) drilled for crosshole experiments. In addition, induction electrical resistivity, neutron porosity and spectral gamma data were recorded in all the holes from the Cqmpos site. Borehole fluid geochemical recordings were also obtained, as part of a routine and repetitive data collection, in all open holes from the site.

<u>Partners 1 (ISTEEM – Montpellier - France)</u>

In order to provide platforms for the development of new downhole geophysical and hydrodynamic sensors to improve the investigation, characterisation and monitoring of coastal aquifers for vulnerability assessment, new experimental sites were developped in the context of ALIANCE. For this, a set of nearby 100 m deep boreholes have been drilled at two opposite, hence complementary sites in terms of hydrogeological properties an behaviour. The objective is to set-up a cluster of extremely well characterized in-situ laboratories at scales where experiments cannot be conducted in traditionnal laboratories. At least one borehole is continuously cored at each site, and the core is fully characterized in petrological, petrophysical, hydrological and geochemical terms prior to new experiments.

Borehole geophysics at Ploemeur (EXS)

The Ploemeur cristalline reservoir in Brittany (France) constitutes the low permeability end member of this set-up, with a fractured aquifer expoited to supply a city of 20,000. Potential threats for this aquifer come from agricultural run-offs and seawater intrusion along the nearby Atlantic coast. In the long run, the impact of global climate change on the ressource is to be evaluated from in-situ monitoring. For this, a detailed characterization of heterogeneities has been undertaken with the drilling of 40 to 100 m deep and nearby holes at two sites located respectively along the coast and a few km inland, both away from the main pumping zone at Kermadoye. One hole has been cored at each site for geological and petrophysical reference. While the inland site straddles the main regional geological boundary with a low angle normal fault separating schists above and granite below, the coastal site penetrates granite with no sign of seawater intrusion as close as a few meters only from the shore.

At each site, the structure and transmissivity of the basement has been studied at mm- to 100 m-scale from borehole geophysical measurements and images, hydrological experiments and core analyses. For this, one of the holes is being studied as site geological reference and more than 60 samples have been taken along a 80 m-deep section (inland) and 40 m-deep hole (on the shore). While the storativity of the basement aquifer appears to be located within the fault zone, most of the transmissivity is provided by fractures. In the shorter term, this site will be used to test the new tools designed in the context of ALIANCE.

Montpellier University (ISTEEM) undertook the geophysical logging of the deeper boreholes in July and October of 2003. The logs that were run included optical, acoustic, gamma ray, spectral gamma ray, electrical resistivity, pH, temperature, fluid conductivity, tilt and azimuth. The 3 main holes at Stang Er Brune cut all an E-W trending low angle normal fault identified by Touchard (1999) between schist (above) and granite (below) near 40 m. The main fractures identified from the borehole wall geophysical images trend on average NE-SW in the schist, and N-S in the granite. This is favorable for a good connectivity between holes the three holes (B1, B2 and B3). In the following, B1 is taken as reference to illustrate the geophysical structure of the site as viewed from borehole geophysical experiments.

Borehole geophysical data and image analysis

In the course of 2004, the activity at Montpellier concerning WP3 focussed on data and image analysis. Concerning downhole measurements, a priority was given to the analysis of the matrix chemical characteristics with the spectral gamma sensor (Figure 11).

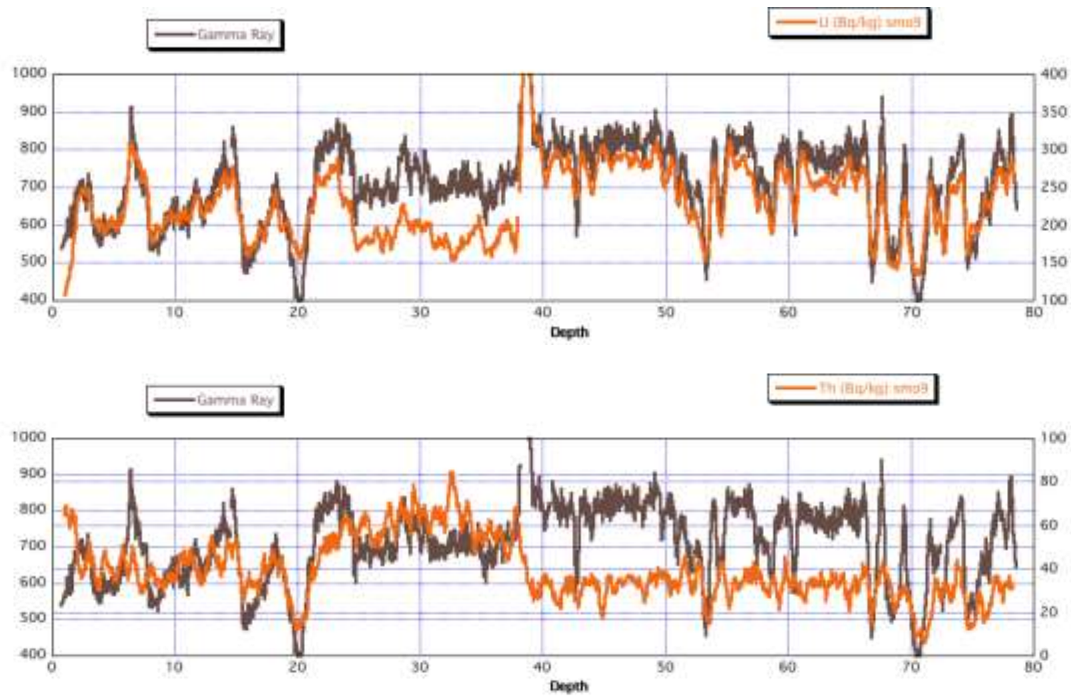

Figure 11. Downhole spectral gamma records from hole B1 at Stang-Er-Brune.

While the total gamma signal is dominated by uranium in altered schists and soils from the upper part of the hole (1-22 m), a significant change in uranium and thorium is obtained to differentiate fresh schist (22-38 m) and fresh granite (40-65 m). Significant uranium loss is recorded in all fracture zones in the granite, while thorium appears to be less reactive to fracturing in granite, except in quartz-rich zones at the base of the hole (68-78 m). The fault zone at 38 m appears to be enriched in uranium, but not in thorium. In all, granite, schist and their respective alteration phases can be identified solely on the basis of these four spectral gamma records (GR, U, Th, K). This result is to be calibrated with and compared in 2005 to geochemical measurements made on a series of core from B1 at the University of Rennes.

In addition, particular efforts were made to the study of fracturing in basement. For this, a composite image of basement structures including borehole wall images and downhole geophysical measurements was assembled (Figure 12). This composite log will, in particular, help to identify potentially open fractures, hence serve as a base for hydrogeophysical experiments to be conducted in 2005.

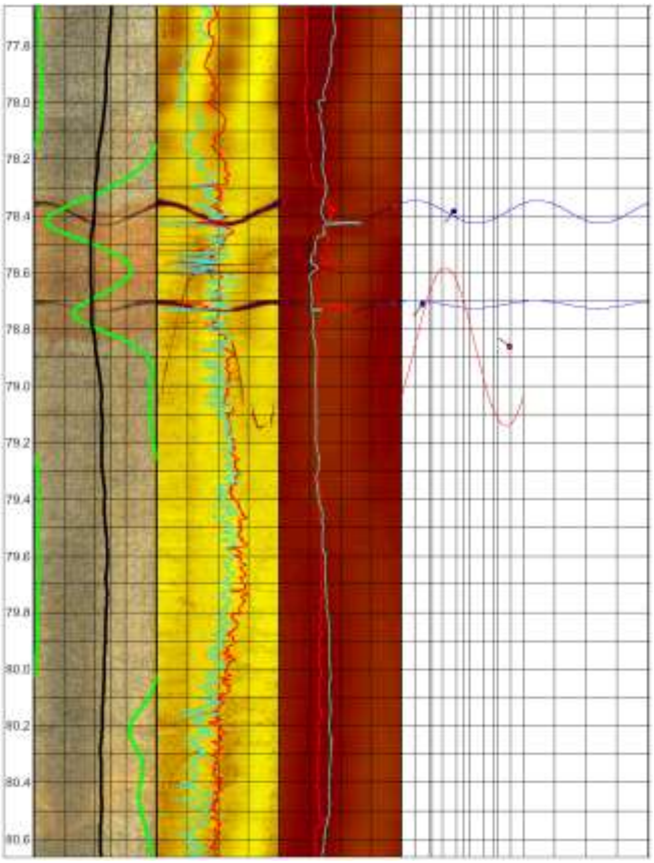

Figure 12. Composite log of optical (left), acoustic amplitude (middle), and acoustic transit time (right) unwrapped image of the borehole surface with reference to North to the left side of each image, with electrical resistivity (green curve), and interpretated fractures (to the far right) from 77.7 to 80.6 m in B1. A pair of open fractures with alteration stain is identified at 78.4 and 78.7 m within an otherwise fresh granite interval.

Fracture density downhole has naturally been derived from this analysis (Figure 13) in each of the basement holes. The study of this composite log has also served as a base to calibrate a new image analysis software program to identify fractures (Figure 14) and lithology (Figures 15 and 16) automatically from borehole wall images.

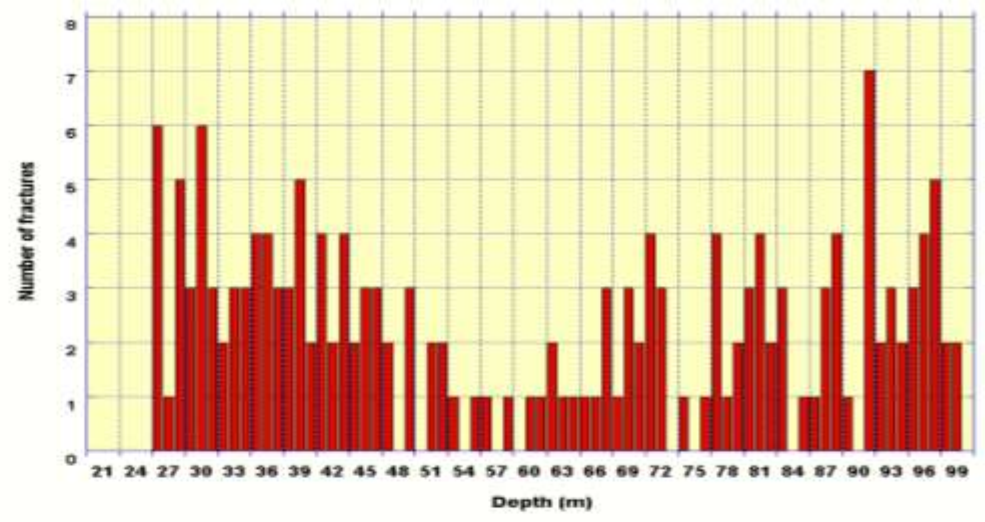

Figure 13. Downhole fracture density in B1, mostly from image analysis (see Figure 12).

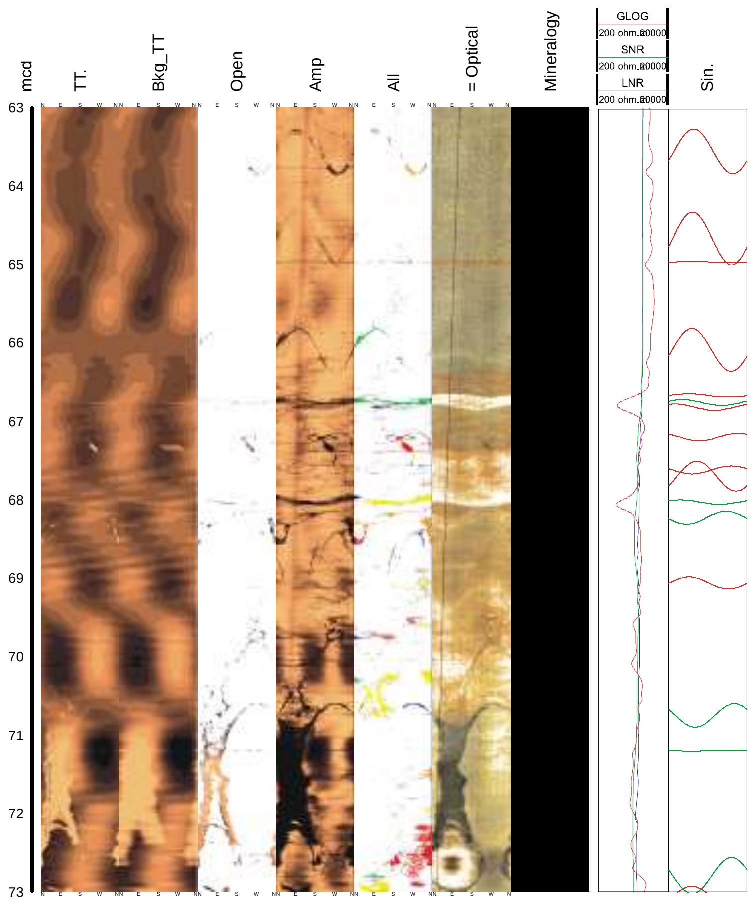

Figure 14. Composite image including, for a 10 m interval (63 to 73 m) in B1, from left to right: transit time acoustic image with background and (to the right) result from the substraction of the two showing open fractures; amplitude acoustic image interpreted (also to

the right) in terms of total fracturing; optical image interpreted (again to the right) in terms of lithology; electrical resistivity profiles; fractures and lithological boundaries from individual mapping. Potentially open fractures are indicated in red.

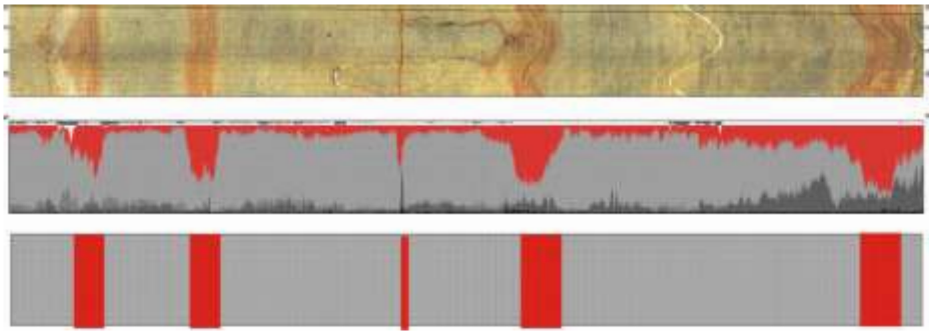

Figure 15. Optical image (top) from a 5 m long interval in B1 (38 to 43 m) analyzed in terms of lithology (middle) and simplified stratigraphy (bottom) for rubified intervals (red) and fresh granite (grey).

While horizons rich in iron oxides are easily detected, the quality of the image does not appear to be sufficient to get rid of the aleration index (red) in the absence of rubifaction. This method consequently needs a calibration and further developments. In 2005, this work will continue in the framework of thesis, and with emphasis on acoustic and electrical properties of the basement, as well as hydroelectrical processes. In particular, individual fractures from B1 will be analyzed in terms of structure from borehole wall images, acoustic response (mostly to surface waves), electrical response (from numeraical modeling), and hydrodynamically from a detailed flowmeter survey and spontaneous potential.

<u>Partner 2 (University of Birmingham - UK)</u>

Analysis of hydodynamic testing results at Ploemeur

A programme of hydraulic and tracer testing at Ploemeur was conducted in November 2003. The results of these tests have undergone preliminary analysis and a report on the hydrogeology of the site has been prepared in draft. The report will be finalised when the results of the tests to be carried out in 2005 have been analysed.

<u>Model of tidal variation</u>

During the testing in 2003, a substantial diurnal variation in water levels coincident with tidal gravity variations was observed and the complete analysis of the tests requires the data to be corrected for this variation. Because the site is small, it is not possible to test it and monitor undisturbed tidal fluctuations simultaneously. Hence a mathematical model has been developed to reproduce the tidal variations. The groundwater system is conceptualised as a slightly leaky confined system overlain by an unconfined aquifer. This is in good agreement with the observed geology, which shows fractured granite partially confined by schist. The model predicts water level changes in both aquifers. Long-term monitoring at 5 and 10 minutes intervals in the granite and the shallow piezometers respectively is underway to provide data to validate the model.

The main aquifer

The total vertical stress on the aquifer is balanced by the effective stress and the fluid pressure:

$$\sigma_T = \sigma_e + P \tag{1}$$

Small changes in the total stress give rise to changes in effective stress and fluid pressure:

$$\Delta\sigma_T = \Delta\sigma_e + \Delta P \tag{2}$$

Changes in the aquifer volume are related to the effective stress by:

$$\frac{\Delta V_T}{V_T} = -\alpha\Delta\sigma_e \tag{3}$$

where V_T is the total volume of aquifer and α is the compressibility of the rock.

Assuming that compaction and expansion of the aquifer occurs only through porosity changes, the increase in the volume of water stored in the aquifer per unit volume of aquifer, is given by:

$$\frac{\Delta V_W}{V_T} = -\alpha\Delta\sigma_e \tag{4}$$

Hence, the increase in the volume of water stored in the aquifer per unit area is given by:

$$\Delta V = \frac{\Delta V_W}{V_T} b = -\alpha b\Delta\sigma_e \tag{5}$$

where b is the aquifer thickness.

Substituting for the change in effective stress from equation (2), and noting that the change in total stress is proportional to the change in gravity gives:

$$\begin{aligned}\Delta V &= -\alpha b[\Delta\sigma_T - \Delta P] \\ &= -\alpha b[\gamma\Delta g - \Delta(\rho g h_A)] \\ &= -\alpha b[\gamma\Delta g - \rho g\Delta h_A - \rho h_A \Delta g]\end{aligned} \tag{6}$$

where h_A is the head in the aquifer and γ is the constant of proportionality. Hence:

$$\frac{dV}{dt} = -\alpha b\left[\gamma\frac{dg}{dt} - \rho g\frac{dh_A}{dt} - \rho h_A\frac{dg}{dt}\right] \tag{7}$$

The vertical water flux from the main to the upper aquifer is just $-\frac{dV}{dt}$. Assuming that the vertical flux is proportional to the head difference between the two aquifers gives:

$$-\frac{dV}{dt} = C(h_A - h) \tag{8}$$

where h is the head in the upper aquifer and C is the vertical conductance.

The upper aquifer

The vertical flux of water into the upper aquifer causes an increase in water level characterised by the equation:

$$S_Y \frac{dh}{dt} = -\frac{dV}{dt} \tag{9}$$

where S_Y is the specific yield of the upper (unconfined) aquifer.

Overall mass balance

Thus, from equation (8) and equation (9):

$$h_A = h + \frac{S_Y}{C}\frac{dh}{dt} \tag{10}$$

and from equation (7) and equation (9):

$$S_Y \frac{dh}{dt} = \alpha b\left[\gamma \frac{dg}{dt} - \rho g \frac{dh_A}{dt} - \rho h_A \frac{dg}{dt}\right] \tag{11}$$

Substituting h_A from equation (10) into equation (11) gives:

$$\frac{S_Y}{C} g \frac{d^2h}{dt^2} + \left(g + \frac{S_Y}{C}\frac{dg}{dt} + \frac{S_Y}{\rho\alpha b}\right)\frac{dh}{dt} + \frac{dg}{dt}h - \frac{\gamma}{\rho}\frac{dg}{dt} = 0 \tag{12}$$

Gravity changes

Temporal changes in gravity are represented by the sum of n sinusoids. Thus:

$$g(t) = \bar{g} + \sum_{j=1}^{n} a_j \sin[2\pi(\omega_j t + \varepsilon_j)] \tag{13}$$

where $\bar{g}$ is the mean gravitational acceleration.

Solution procedure

The expression for $g(t)$ from equation (13) is substituted into equation (12), which is then solved numerically to give $h(t)$. Equation (10) is then used to calculate h_A from $h(t)$. A simple, explicit, central finite difference scheme has been used.

Figure 16 shows a comparison between modelled and observed heads in the granite. The field data have been detrended to remove longer-term variations in water level. The general agreement is good. The modeled response shows a 10-20 minute forward phase shift, which is now being investigated further.

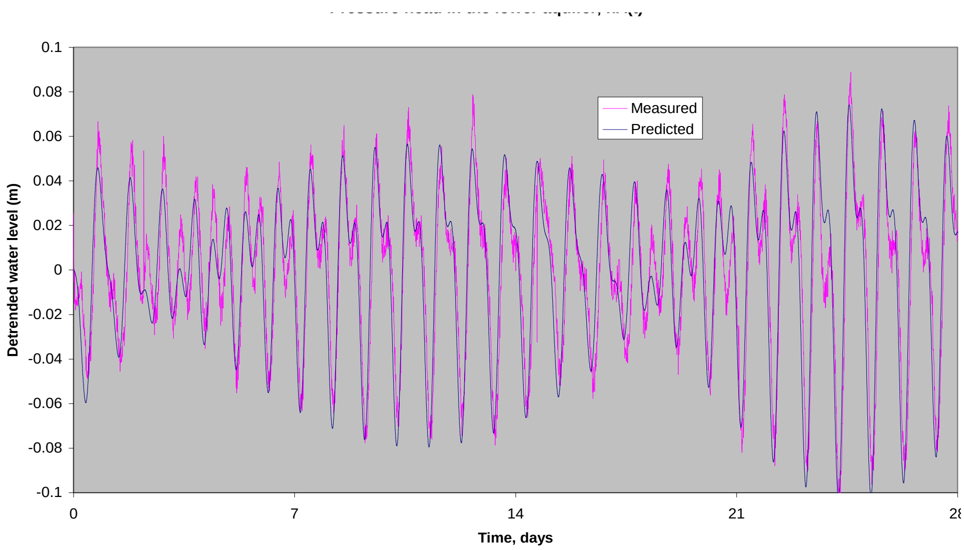

Figure 16. Pressure head measured in the lower aquifer of B1 over a one month period, with prediction from earth and ocean tides.

Hydraulic testing

Analysis of step drawdown tests in the site boreholes shows the existence of significant non-linear losses. In particular, the results for Borehole 1 show drawdown of up to 18 m in the abstraction borehole (Figure 17) with a maximum drawdown of approximately 27 cm in the nearest hole, just 6 m away (Figure 18). In addition, transmissivity estimates based upon pumping from Borehole 1 are significantly lower than derived from all other boreholes. It is suspected that these effects result from the construction of the borehole by diamond coring. This was a very slow process requiring the replacement of the drill bit three times. It is believed that the slow grinding of the rock produced large quantities of rock flour that have affected the transmissivity of fractures close to the borehole. The remaining boreholes, which show less significant non-linear losses, were drilled rapidly using down-the-hole hammer.

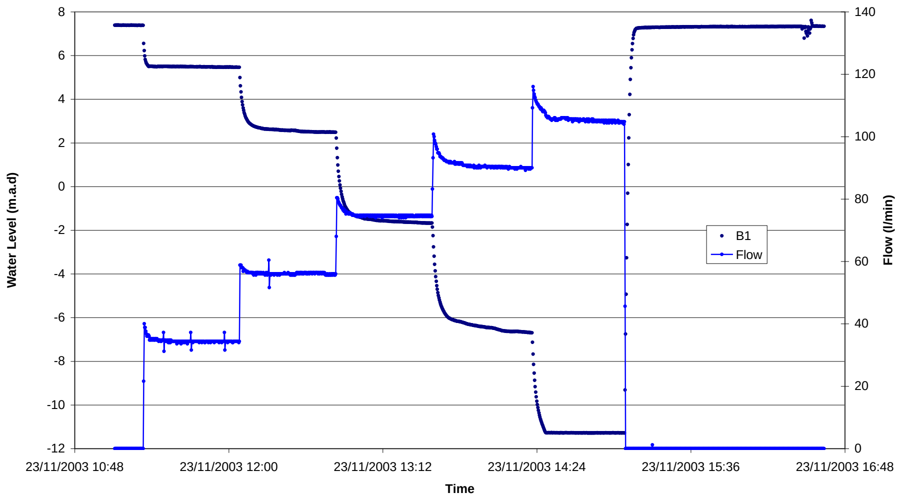

Figure 17. Simultaneous plot of fluid flow (in l/mn) and water level in the hole (in m) during a 6 hours long testing period in B1.

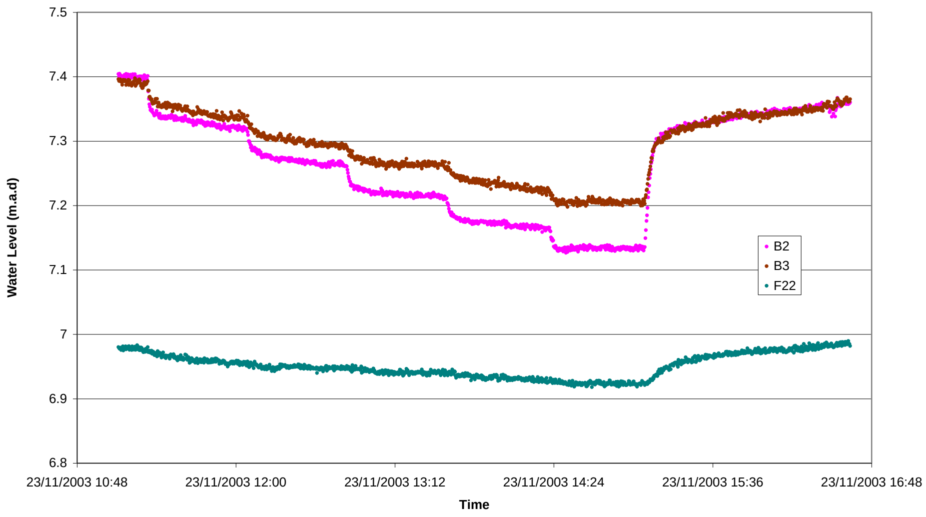

Figure 18. Water level response in B2 (pink), B3 (brown) and F22 (blue) to testing in B1.

Tracer testing

Tracer tests were carried out with Fluorescein and Amino-G Acid between boreholes B3 and B1, and B2 and B1 respectively (Figure 19).

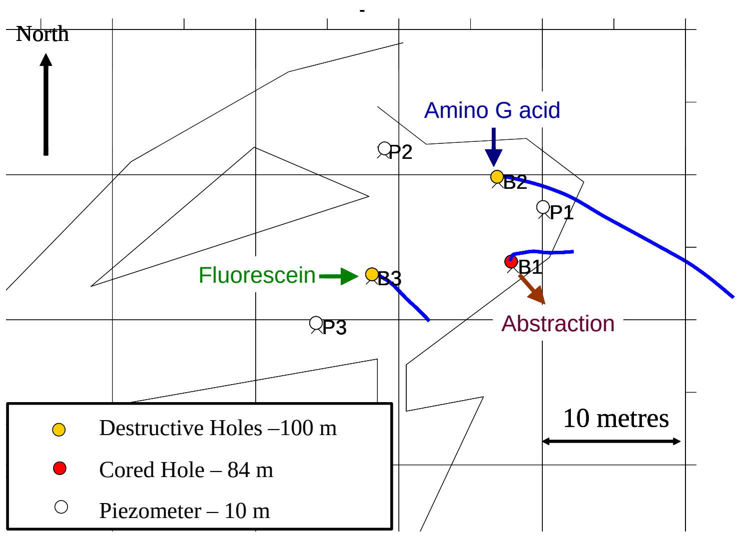

Figure 19. Relative location of boreholes at Stang-Er-Brune, with downhole trajectories, tracers injection holes, and abstration hole (B1).

The fluorescein and amino-G acid breakthrough curves exhibit typical features, but the complexity of the flow system is exemplified by tracer concentration profiles recorded on the 27th and 28th of the month in B2 following amino-G acid injection in that hole on the 25th and fluorescein injection in B3 on the 26th (Figure 20). amino-G acid concentrations are depleted except in the cased section of the injection well as expected. However, fluorescein is seen to be present in the lower sections of B2 even though the base of the hole is on the opposite side of the abstraction hole from the fluorescein injection borehole.

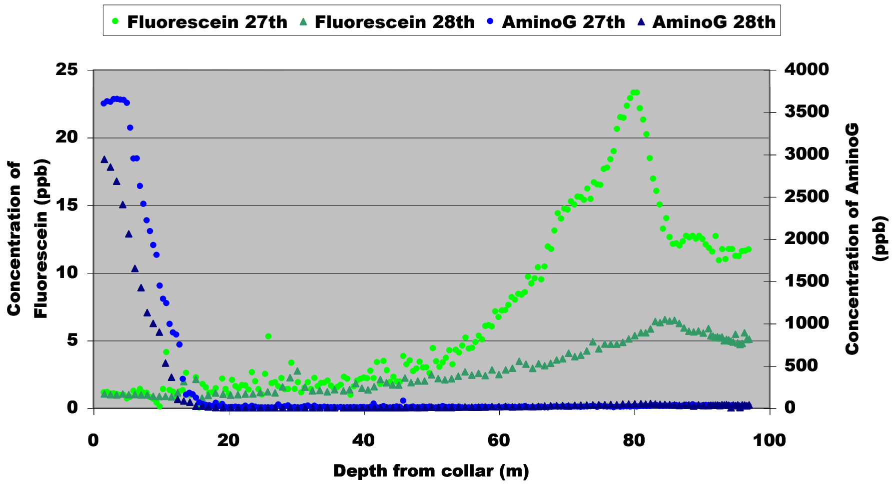

Figure 20. Tracer concentration with depth in B2.

It is clear that no simple model of tracer transport based upon uniform property distributions will reproduce this behaviour. Full analysis of these tests will be conducted with the discrete fracture network modelling software, VodoLei, developed as part of WP7, following full analysis of the additional hydraulic testing to be conducted in 2005 to identify the principal transmissive features in each borehole.

Borehole geophysics at Campos (SWS)

A series of 100 m deep boreholes located a few to 100 metres away from each other have been drilled. The objective is to set up an extremely well characterised in-situ laboratory at scales where experiments cannot be conducted in traditional laboratories. Five boreholes have been continuously cored, and the core is fully characterised in petrological, petrophysical, hydrological and geochemical terms. One of the borehole (MC2) is being studied as site geological reference and more than 100 samples have been taken as part of WP4 activites.

A field campaign was organized in 2004 in order to improve the existing dataset and record measurements in the two holes drilled in perpendicular directions 5 m away each from MC2, in view of crosshole experiments in 2005. In addition, the activity at Montpellier concerning WP3 focussed in 2004 on data and image analysis. Concerning downhole measurements, a priority was given to the analysis of lithology with the spectral gamma sensor (Figure 21).

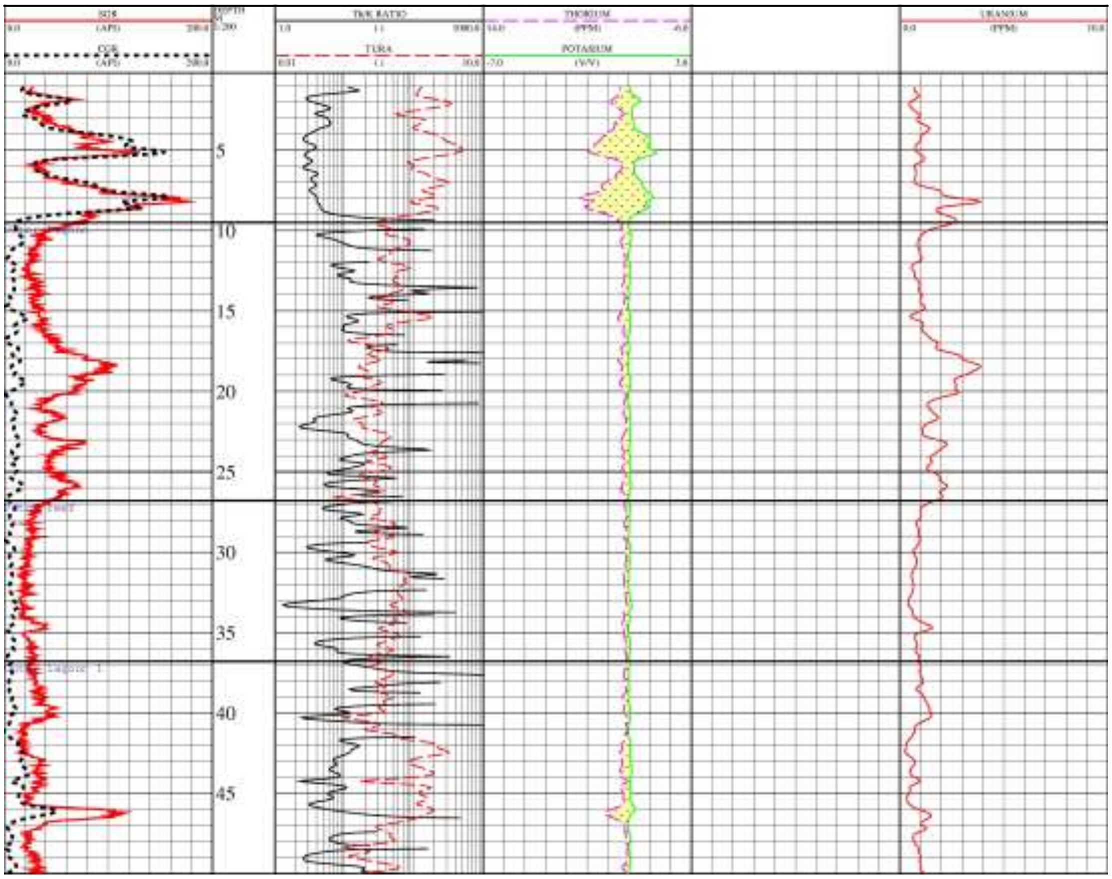

Figure 21. Downhole spectral gamma records from hole MC2 in Campos with, from left to right, total gamma, Th/K and Th/U ratios, Th and K, and U (alone) indicating red algae.

While the total gamma signal remains low throughout the sequence, the signal at the top of the hole and 47 m is explained by the presence of clay, possibly montmorillonite and mixed-layer clays, from the thorium-potassium ratio (Figure 22). Below 10 m, most gamma peaks are explained by an increase in uranium due to the presence of red algaes in the column due to past low sealevel stands. From coastal to shallow and deeper marine settings, the paleo-environments of deposition and diagenesis will be derived from this dataset in 2005.

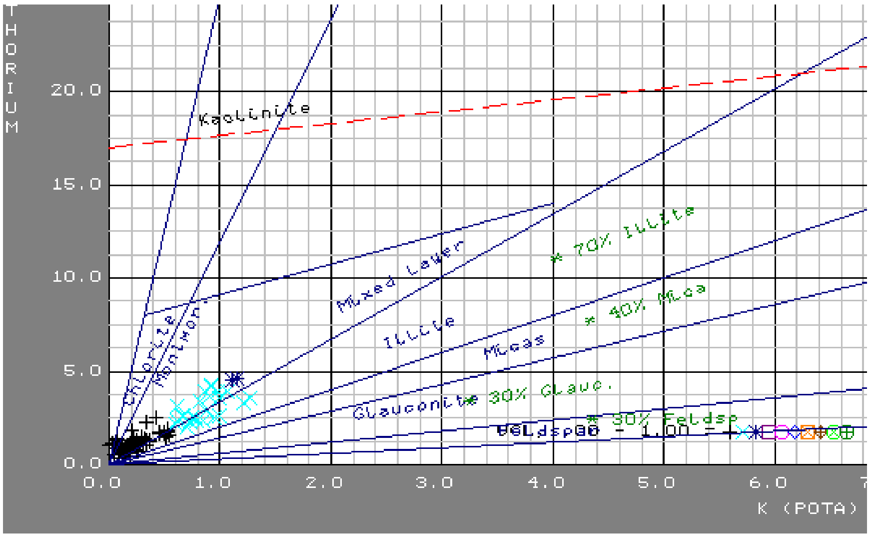

Figure 22. Thorium potassium crossplot for spectral gamma data in MC2.

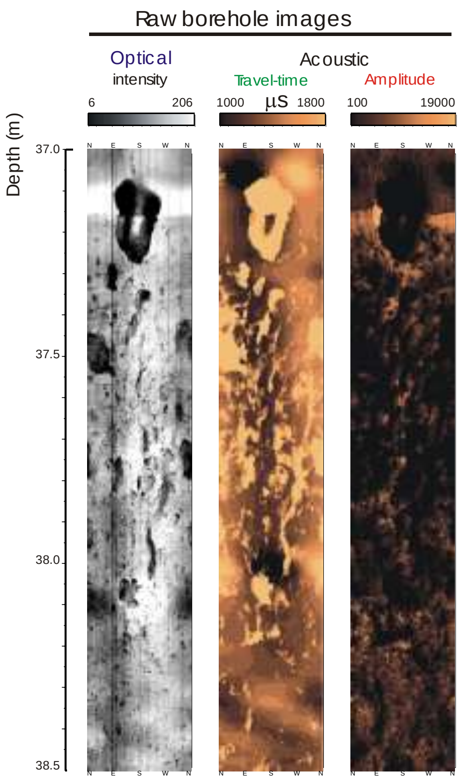

Figure 23. Composite presentation of mm-scale borehole wall images over 1.5 m in the MC2 hole, near the top of the water table. Optical (left), acoustic amplitude (middle), and acoustic transit time (right), images show mesoscale, vuggy porosity structures below a completely recrystallized interval at 37.0 m.

Mesoscale porosity downhole (here vugs and mini karsts) has been derived from an image analysis similar to that developped for fracture detection in granite (see above). From original images (Figure 23), a background is substracted to improve signal quality (Figure 24), and vugs can be isolated and counted per unit length of the image (Figure 25). A continuous curve versus depth is consequently obtained for each of the three images.

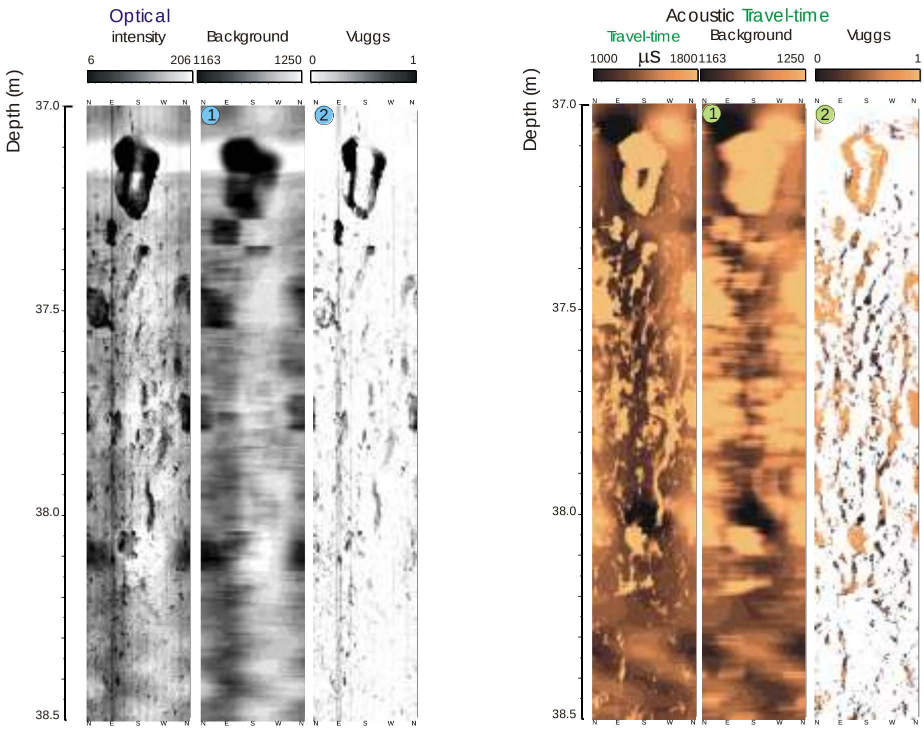

Figure 24. Vugs extracted (right) from two types of images (left), after substraction of the background (middle) in each case, over a 1.5 m long interval in MC2.

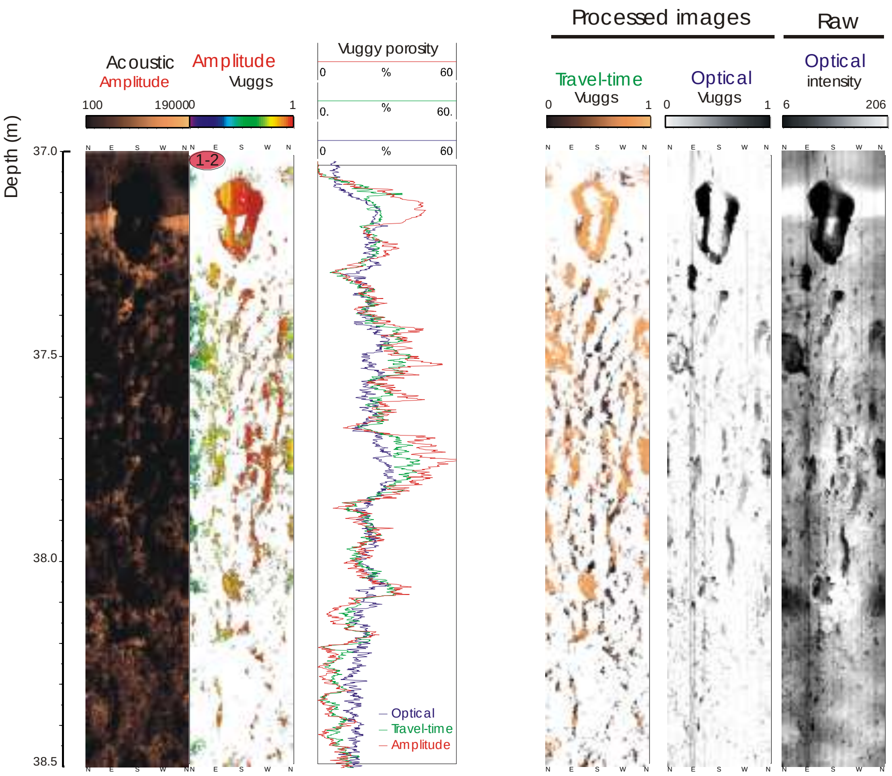

Figure 25. Composite image including, for a 1.5 m interval (37.0 to 38.5 m) in MC2 (from left to right): amplitude acoustic image with derived mesoscale porosity, mesoscale porosity profiles derived from the 3 images (middle), and the associated vugs distribution images obtained in each of the 3 cases (to the right).

In 2005, this work will continue in the framework of a thesis, and with an emphasis on describing heterogeneities, on improving the dataset at the opportunity of the final phase of field experiments, during the testing of new tools. In addition, the detection of mesoscale porosity (vugs and mini karsts) will be calibrated directly from core analyses.

Partners 3 (ETH-Zurich – Switzerland)

Mesoscale pore structure in limestones

The sampling intervals of downhole logs are far smaller than their resolution. Each log has its inherent scale of investigation and may not be appropriate for all lithofacies types, because also a lithofacies type has a dominant inherent scale of heterogeneity. Within carbonate reservoirs sampling plugs at a constant rate introduces large bias (Corbett et al. 1998). Furthermore the signals from logging tools such like resistivity tools, investigating volumes, which are several orders of magnitude larger than the volumes comprised by standard 1 inch plugs are not just simple averages of the plug values. Sampling has to be performed for each lithofacies type separately and targeted on representative elements. Such representative elements can then later on be modeled with geo-modeling software like GOCAD. Visualizing the scales of heterogeneity is important for checking the match or mismatch between core and log data. The log is a series of anomalies which can be described in terms of spatial frequencies using the Fourier technique; the inverse of the wavelength being its spatial frequency (Jackson et al. 1998). With this method for each tool the investigated scale of heterogeneity can be calculated. Another method allows for varying the scale of investigation is the scan of acoustic travel time. This is a new high-resolution method, which will be introduced and used here for the first time for evaluating the heterogeneity distribution within the formation and the inherent scales of heterogeneity for each lithofacies type. By varying the resolution or investigation area of the tool, REV's can be assessed by statistically analyzing the dataset. In addition with this tool the fine scale sedimentary structures, which are known to be important controls of reservoir behavior, can be adequately characterized (Jackson et al. 1998). Small-scale heterogeneities have also been considered by using FMI and FMS (Russell et al. 2002). Other authors use combinations of standard logging tools in order to assess the pore structure. Anselmetti and Eberli (1999) calculated velocity deviation logs from neutron and sonic logs. With this method they got downhole information about the predominant pore type.

Results from Ses Sitjoles test site

For larger scales (cm to m) numerous borehole logs provided insight into the variation of petrophysical parameters along the vertical borehole axis. The logs had to be calibrated very carefully with lab data in order to produce meaningful results. The outer lagoon sediments are in general less porous than the talus sediments. In average values between 15 and 20% have been found which also seems to be a valid range for rudstones within this zone. This is a remarkable difference compared to talus sediments with 30 to 35% porosity. A clear distinction can be made between proximal and distal talus. The border is built by a prominent rudstone above which in most boreholes porosity increases in average about 5%. The rudstone exhibits a lower porosity than the surrounding sediments. In addition the sonic velocity is decreased there, which is somehow contradictory. The reason for this phenomenon is subject of the ongoing work. At borehole scale porosity variations are highest within reef core. This result has been proved by all logging techniques. At borehole scale measured porosity is strongly affected by large dissolution cavities and karstic channels. Therefore within the karstified reef core at this scale high porosity contrasts are present. Whereas the induction technique yields for proximal and distal talus more or less similar values, sonic porosity as well as TOP from the acoustic televiewer scan (ATS) is clearly lower within distal talus. This is mainly due to the different scales of investigation and therefore a change of the porosity type. The signal from the sonic tool is known to be affected by the pore type. Framework-like porosities tend to yield too low sonic porosities (Anselmetti et al., 1999). These pores are not connected and the matrix is dense, cemented and has undergone an intense diagenesis. The distal talus is therefore less permeable than the proximal talus, although total porosity is comparable. The ATS resolves porosity down to a size of a few mm. Therefore if small scale intergrain porosity or a large amount of microporosity is present, TOP will be much lower than real total porosity. The ATS only records the visible heterogeneities or the macroporosity. But these visible heterogeneities are controlled by the fine scale sedimentary structure which itself is controlling the reservoir behaviour. The curves of heterogeneity distribution from ATS measurements also provide insight into the lateral heterogeneity distribution within individual lithofacies types. Distal talus exhibits a very homogeneous distribution of macroporosity whereas macroporosity in outer lagoon and proximal talus is lognormal distributed. No statistical distribution can be observed for the karstified reef core. At present a geostatistical analysis is being performed on the ATS data in order to extract REV’s and to test the variability of heterogeneity distribution.

Results from induction logs

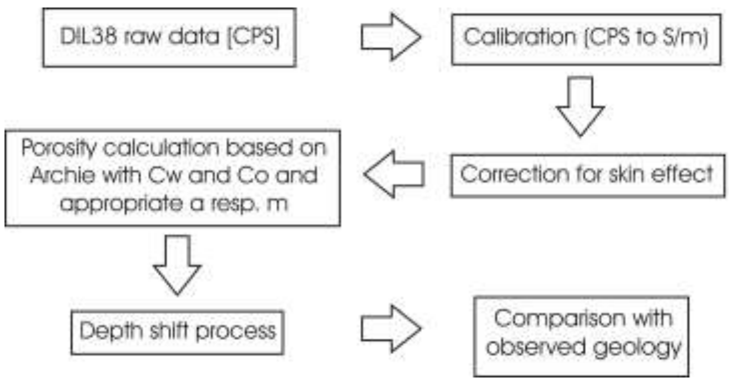

Figure 26. Schematic flow diagram for induction resistivity analysis.

Data from the DIL38 have been processed according to the flow chart above. The dataset has been compared to the geology observed on core material. As seen from all porosity logs despite the fact that different values for parameters a resp. m yield different porosities, the relative porosity changes remain the same. On these porosity changes we want to concentrate first and in a later phase try to calibrate the logs on lab porosity measurements. The values mentioned in the following discussion are based on the Archie equation without clay correction and parameters derived by Bussian equation are a=1 and m=1.3.

Boreholes MC4, MC5 and MC7

MC4, MC5 and MC7 show comparable log characteristics. Values in the distal talus are quite uniform and lie at 30%. The boarder between distal and proximal talus is clearly identifiable on these logs and well corresponds to the depth observed on core material. At the transition in all 3 boreholes a rudstone could be identified, which exhibits lower porosities of about 25% (blue zone in Figure below).

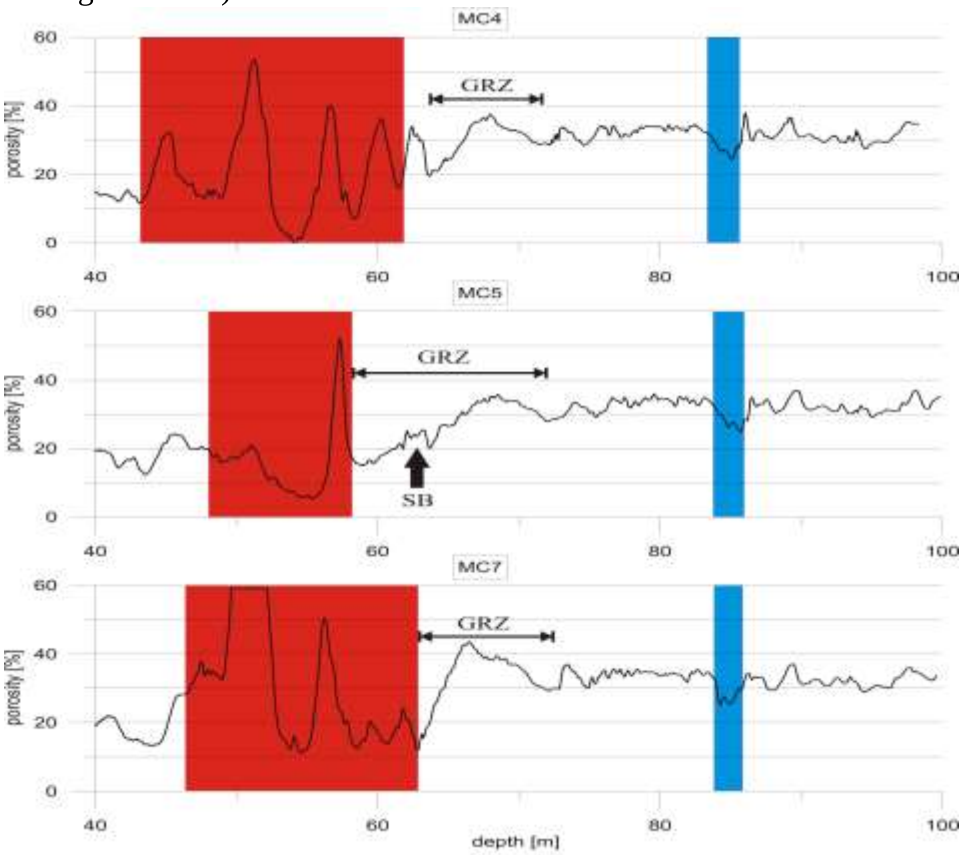

Figure 27. Comparison of porosity profiles derived from resistivity for MC4, MC5, MC7.

The boarder to distal talus is set at the bottom of this remarkable rudstone. Interestingly smaller rudstones with thickness<0.5 m are not recognized any more in the porosity log. This could be due to their lenticular form or more probable due to the resolution of the induction tool (see section 5). Locally enhanced porosities (up to 40%) are due to small fossil accumulations, with larger coral fragments or rhodolithic floatstones, the latter can be observed in these boreholes around 73 m. Above the boarder distal/proximal talus porosities are a bit enhanced and lie around 35%. At MC4 porosity increases from 72 m to 68 m continuously by 10% to almost 40% and decreases again towards 63.5 m to 20%. This characteristic zone could be observed in all boreholes and will be designated here as the gradient zone (GRZ). Above this zone a high variability starts, which characterizes the reef core (red zone in Figure 27). At MC5 the gradient zone can also be observed, with a decrease in porosity towards 58.5 m down to 15%. The sequence boundary at 63 m shows slightly enhanced porosity, which is due to the clay effect (see section 8). The base of the reef is again marked by a strong porosity peak. MC7, which has been drilled destructively, shows similar trends however intensified. Within the gradient zone from 72.5 m to 66 m porosity increases till 45% and then falls towards 63 m to a value of 10%. Above the gradient zone presumably the reef core starts though the high variability, which is typical for reef core only begins at 58 m. Within the reef core high variability in porosity with abnormal values up to 100% is typical. But we have to keep in mind, that within karstic zones clay values are significantly enhanced and therefore porosities derived from formation resistivity are biased. However the high porosities yield in general a good approximation, because such zones contain high transmissive karstic channels. Low porosity zones within the reef seem to correlate with dense, recrystallized rock. Porosity of the external lagoon is with 15-20% in average remarkably lower than in the talus.

Borehole MC1

At first glance this log shows no similarity to the others. At MC1 from bottom to 67 m porosity is quite uniform with an average value of 30% and no real difference between distal and proximal talus can be observed. The rudstone at 80 m shows like in MC3 at 86 m a reduced porosity (blue zone in Figure 28 below). Local increases are due to macrofossils, like large bivalves and coral fragments. From 67 to 60 m again the gradient zone occurs. Porosity increases till 65 m to 45% and decreases then till 60 m down to 20%. From 60 to 55 m follows a low porosity zone with values between 20 and 25%, whereas values are disturbed by two lost drill bits located at 59 and 56 m. Possibly within this borehole the gradient zone (GRZ) is not directly followed by the reef core (red zone).

But it has to be mentionned, that due to the stuck drill bits and the inaccurate depth control in MC1 no clear proof can be provided. Within the reef core another stuck drill bit at 48 m produces a biased signal. In general low porosities with a high variability dominate. Karstified zones are nicely displayed by high porosities.

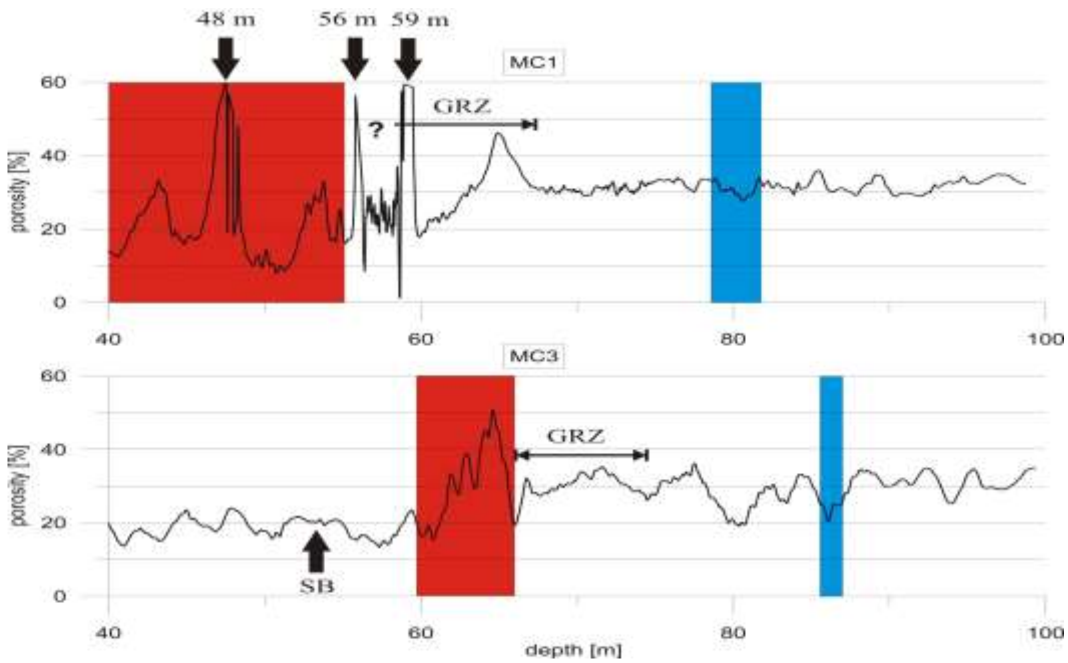

Figure 28. Comparison of porosity profiles derived from resistivity for MC1 and MC3.

Borehole MC3

This borehole seems somehow to play a special role compared to the others. It also exhibits a rudstone at 86 m but more low porosity zones (5-10% less) occur at 80 and 94 m without any observed rudstone layer. These zones could be affected by dense fracture sets, which have been observed at those depths in MC3. A closer comparison to fractures analyzed on the boreholes still has to be performed. Average porosity within talus is on the order of about 30%. No distinction between proximal and distal talus is possible, which could be due to an overlaying signal from intense fracturing. The gradient zone occurs from 74 to 67 m with a maximum at 71 m but is not as pronounced as in the other boreholes. The gradient zone lies clearly deeper than in the other boreholes. In MC3 also the reef is located deeper, which gives raise to the assumption of a genetic origin (in context with reef genesis) of the gradient zone. Within the reef core again strong variations with high amplitudes occur, whereas amplitude is highest at the bottom of the reef, like observed at MC5 too. Porosity is 50% at the bottom and decreases in an oscillating manner down to 20%. The outer lagoon is characterized by porosities of 15-20% at low variations. The thick rudstones at 41 and 46 m cannot be easily detected from the porosity profile. There is no clear difference to the grainstones in the background, which is much less porous, than sediments in the talus. Like in the other boreholes, the sequence boundary between 52 and 54.5 m with increased clay values shows abnormal high porosities.

The porosity gradient zone first found by seismic tomography and confirmed by sonic logs has again been clearly identified in all boreholes with the induction tool. The zone starts in general right at the reef bottom and extends to about 8-13 m below. Uncalibrated porosity changes range from 10-45%. A comparison to thin sections is required also for checking the reason of the deviation between sonicΦ and RΦ within this zone. We suppose a process, which is strongly related to reef evolution, because depth of the gradient zone seems to be correlated to reef depth. Sequence boundaries show no or even positive signals due to higher clay content. A clay correction would be necessary in this case. In general sequence boundaries with high gamma readings lead to biased readings of the induction tool. However for maybe 95% of the area investigated by induction logging, the assumption that no clay minerals disturb the measurements remains valid. The locations where clay occurs are clearly identifiable by the gamma tool and are restricted to sequence boundaries and karstic cavities within the reef core. Clear signals have been found at the transition from distal talus to proximal talus. The top of distal talus has been set to a rudstone, which occurs in all boreholes. The part on top of the rudstone, in most boreholes exhibits in average a porosity, which is about 5% higher than below it. The signal of this prominent rudstone is negative in all boreholes, although its thickness varies considerably between 1 m in MC5 and 3 m in MC1. The outer lagoon sediments are in general less porous than the talus sediments. In average values between 15 and 20% have been found which also seems to be a valid range for rudstones within this zone. This is a remarkable difference compared to talus sediments with 30 to 35%.

Results from sonic logs

Porosity calculated from sonic logs is not necessarily a total porosity, because it appears to be affected by pore shape, geometry and therefore controlled by the pore type (Brie et al., 1985; Anselmetti and Eberli, 1993; Kenter and Ivanov, 1995). Five main pore types are distinguished, namely moldic, intrafossil, interparticle, microporosity and low porosity carbonates (<10%). If we calculate synthetic velocities using measured porosities on plugs and compare them to porosities derived from sonic logs, largest deviations are observed in samples in which intrafossil porosity dominates (Anselmetti and Eberli, 1999). Similar observations have been made for moldic porosity. Therefore large positive deviations are typical for porosity types, which build a framelike fabric which means that within these zones measured sonic velocity is relatively high and also porosity is high. In other words, sonic log tend to overlook porosities with a framelike fabric (Anselmetti and Eberli, 1999) or large vugs (Lucia, 1999) and measured velocities in such zones are therefore too high.

In a highly porous carbonate setting, like the Miocene reef platform of Llucmajor, velocities lie in the range of 1500 m/s for the fluid, which is water in this case and 7000 m/s for dolomite, which exhibits slightly higher velocities than calcite. On our test site at Ses Sitjoles boreholes lie predominantly in calcitic carbonates and an upper threshold of 6500 m/s can therefore be assumed. In the vadose zone clays and marls of inner lagoon are abundant, but the dry part cannot be logged by the sonic tool.

Porosity values can be calculated using the time average equation of Wyllie (Wyllie et al., 1956). This empirical relationship is only valid for low differential pressures, which means no overburden and low fluid pressure, which is accomplished on our site. At high differential pressures better results may be achieved by the more complicated empirical equations of Gassmann or Pickett. If we derive porosity Ø from the time average equation, it arises that three special cases can occur:

a. Vsonic > Vsolid → Φ = negative!
b. Vsonic = Vfluid → Φ = 100%
c. Vsonic < Vfluid → Φ > 100%

If we use Vsolid = 6500 m/s and Vfluid = 1500 m/s, measured Vsonic has to be smaller or equal to 6500 and larger or equal to 1500. Therefore two filters have been applied on the measured Vsonic, namely a low cut (Vp < 1500 m/s) and a high cut (Vp > 6500 m/s) filter. This enables the conversion from Vp to porosity to yield reasonable values. Unrealistic values of Vsonic originate from first arrival picking within WellCAD, which revealed to be a difficult task. Especially within the reef core, full waves of the upper receiver often didn't show clear wave forms and were contaminated with a high noise in amplitudes.

Curves from automatic picking and those picked manually do not differ significantly. The confidence for large peaks is not as high as in zones with moderate values. Manual picking in such zones is complicated by diffuse first arrivals and a high noise level. The velocity profile from borehole MC5 is only available in two parts and depth control proved to be a difficult task. There the calibration of data is based on several assumptions. MC4 data is therefore believed to be more consistent and reliable than MC5 data.

Borehole MC4

Three domains of different characteristics in Vp-signals can be delineated. In general one observes high amplitudes and large variability of Vp (1000-6250 m/s) in the upper section till 67 m and lower amplitudes and small variability (2000-3000 m/s) in the lower section till the end of the log at 96 m. A further velocity boarder lies within the lower section which divides it into part 67-86.1 m with variability of 2000-2500 m/s and part 86.1-96 m with slightly higher variability of 2500-3000 m/s. The upper part is characterized by zones of low velocities at 44.1-46.0, 49.6-52.3, 56-57.2, 58.7-61.2 and 62.1-63.3 m. These zones correlate well with observed karstic cavities on core material. Most of these cavities can be clearly seen on the gamma log, which is significantly increased there and explained by karstic clay fillings. In between and associated with karst lie high velocity zones at 49.0, 54.6, 58.5 and 61.6 m which are interpreted as dense, recrystallized rock with low porosity. Interestingly the transition of high variability to low variability does not coincide exactly with the end of the reef core, observed on core material at 62 m. Partly recrystallized zones below the reef core, which are probably part of a gradual diagenetic transition to talus sediments could be the reason for this phenomenon. This observation is in good agreement with data from seismic tomography (Maurer and Friedel, 2004). From 67-86.1 m sonic velocities of 2000-2500 m/s occur. This low variability at a low mean value implies a homogeneous rock (m-scale) with high intergrain and moldic porosity (around 50%) and no karstification respectively recrystallization. Porosity derived from Vp is presumably too high due to the high amount of molds observed on core material. Rudstones are in general indicated by slightly lower velocities, which could be due to higher porosity. The boarder at 86.1 m at which velocities slightly rise to 2500-3000 m/s very well corresponds to the boarder proximal/distal talus observed on cores. The lower part is more finegrained and rudstones are less common.

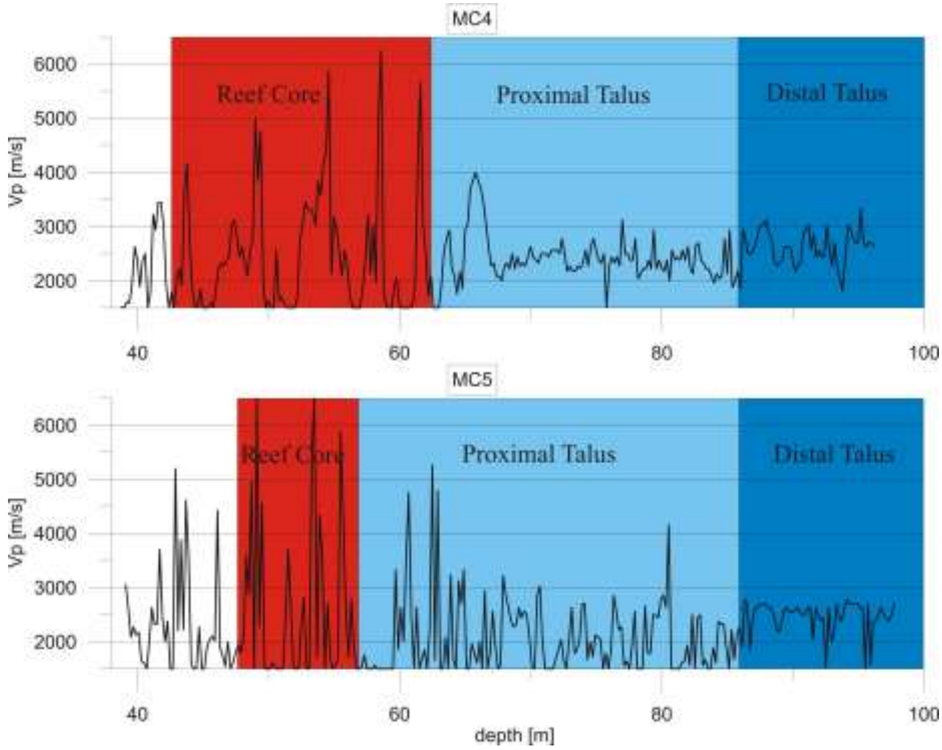

Figure 29. Comparison of P-wave velocity profile in MC4 and MC5.

<u>Borehole MC5</u>

Four domains of different characteristics in Vp-signals can be delineated. One observes a high variability of Vp (1000-5000 m/s) in the upper section till 48 m. Then a domain in which variabilities are highest follows (1000-6500 m/s) till 63 m. In a next section 63-86 m lower amplitudes, but still with a high variability of 1000-3000 m/s are present. Finally at 86 m again like in MC4 a uniform zone with velocities of 2500-3000m/s follows. The upper part till 48 m lies within grainstones-rudstones of the outer lagoon, which is here sandwiched between a patch reef on top and the main reef core at the bottom. This zone exhibits a high porosity, which mainly originates from fossil molds. Recrystallized corals or coral fragments cause a high reading on the sonic log, which can be observed at 43 and 46 m. From 48-63 m large differences in velocity are present. Zones with extremely low sonic velocity are detected at 49.7-53.1, 54.3-55.3 and 56.5-59.5 m. Except for the reef core there is a poor correlation to karst observed on core material. There is also no correlation of karst with the gamma signal in this borehole. Obviously no thick clay fillings are present within cavities. Recrystallized zones with high sonic readings have been detected at 42.9, 48.9, 53.4, 55.5 and 62.5 m. Most of them lie within the reef core, which extends from 47.5-57 m. Again the coral framework, especially when karstified is strongly recrystallized. Similar to MC4 the bottom of the reef core does not coincide with the disappearance of the high variability zone. At 63 m, a sequence boundary with fine grain, partly recrystallized wackestones is present. This boundary generates a high gamma signal and is clearly marked in the sonic log by two sharp peaks. From 63-86 m maximum amplitudes are about half but variability still persists. Core material revealed coarse grain grainstones with thin rudstones in between. Porosity calculated from sonic log is relatively high, but framework porosity like fossil molds is common and therefore care has to be taken with absolute porosity values. At 86 m the boarder of proximal/distal slope again appears very clear on the sonic readings. Variability of Vp with 2500-3000 m/s is less and implies a homogeneous and less porous rock at this depth. From porosity analysis on thin sections it is known, that the main pore type at that depth is intergrain porosity. Therefore total porosity does not necessarily have to be lower than in the proximal slope, but main pore types are surely different.

A zone of highly variable V_p, which is typical for reef core and the adjacent transition zone to talus sediments could be detected. Proximal talus exhibits low Vp at quite a high variability whereas distal talus shows a higher mean Vp and the signal remains more uniform. As seen on the logs, a rough estimation of porosity can be given and the velocity profiles well describe large scale features like heterogeneity, lithofacies boarders and mean sonic porosity. For a reliable quantification of porosity the data has to be compared to porosity measured on core material such as mini cores or thin sections. In combination with a neutron-porosity or density log velocity deviations could provide us with interesting information about pore types or even permeability trends within the borehole, as described in Anselmetti and Eberli (1999). Velocities do not change abruptly at the transition from reef core to proximal talus, which as well has been observed with other investigation methods.

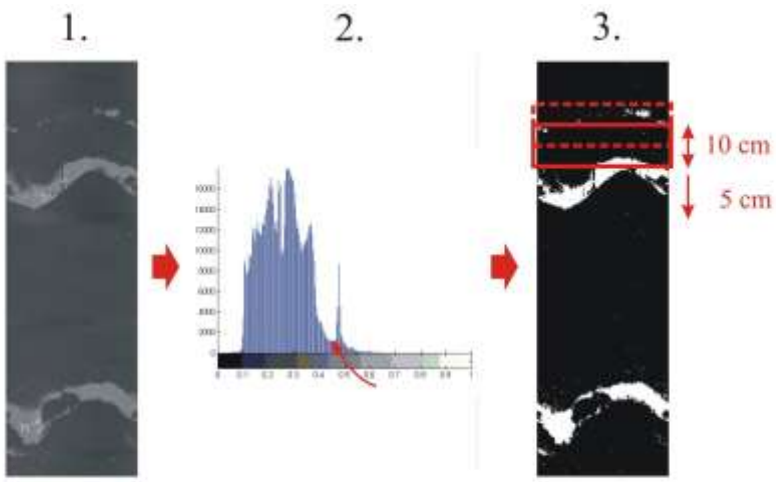

Figure 30. Results from acoustic travel time scan (ATS).

Data from acoustic logs have been used in order to determine the downhole heterogeneity distribution or distribution of macroporosity (pores larger than 1 cm). The acoustic log images the borehole wall and the travel times yield an image comparable to the optical televiewer. The main advantage of the acoustic log compared to the optical televiewer is the independence of illumination (opaque borehole fluid) and borehole wall color. A disadvantage is its sensitivity to decentralization of the tool. The image of the acoustic travel time is converted to a gray level image (1). A moving average scans the whole log with a predefined scanning window and a preset scanning increment on total optical porosity (3). This is done by thresholding the gray level image at an appropriate value, which is determined through comparison with the corresponding optical televiewer image (2). The resolution of the technique had been chosen at 1 cm in order to avoid artifacts from decentralization, artificial borehole roughness, scratches and outwashings. The obtained dataset therefore is quite accurate for characterizing the heterogeneity distribution on the mesoscale, such as moldic pores, vugs, fractures and karstic and non karstic cavities.

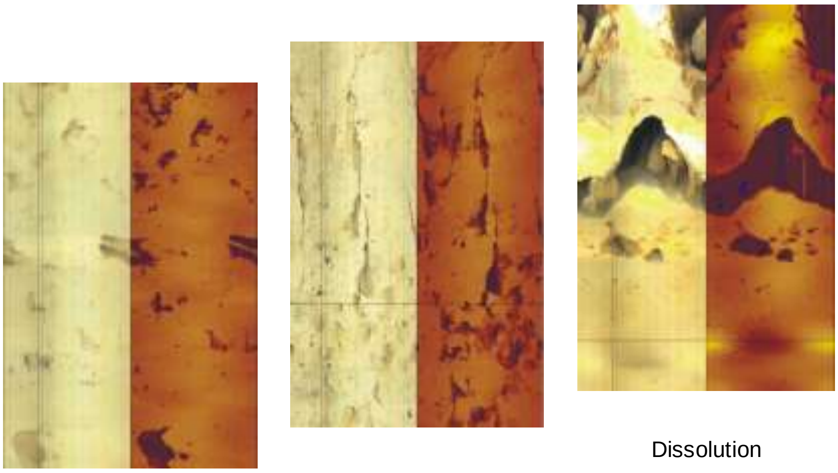

Figure 31. Illustration of geological and hydrological features from optical images.

For displaying the heterogeneity distribution along the borehole a moving window of 10 cm length, which is shifted by 5 cm steps has proven to be appropriate. The figure below displays the macroporosity (>1 cm) heterogeneity distribution along boreholes MC2, MC3 and MC5 in comparison with the observed geology or lithofacies-distribution. In general the heterogeneity distribution seems to fit quite well the geology observed on core material. Outer lagoon exhibits larger zones, which are relatively homogeneous but variations still can be quite pronounced if outer lagoon in MC2 and MC3 are compared to each other. In MC5 the outer lagoon is more heterogeneous and TOP lies at a remarkably higher level. This is due to its sandwiched position between the patch reef above and the reef core below. Like expected the variability within reef core is very high and on the chosen cm-m scale the TOP seems here to be highest! Proximal talus is clearly less homogeneous than outer lagoon and certain trends in increasing and decreasing heterogeneity seem to be present. These trends seem to express the sedimentary environment and especially the genetic stage of the reef complex. A comparison to the sequence stratigraphical model is supposed to yield quite good coincidence with the heterogeneity trends within proximal talus. Distal talus is very homogeneous on this scale and the transition from proximal to distal talus is quite pronounced in all 3 boreholes.

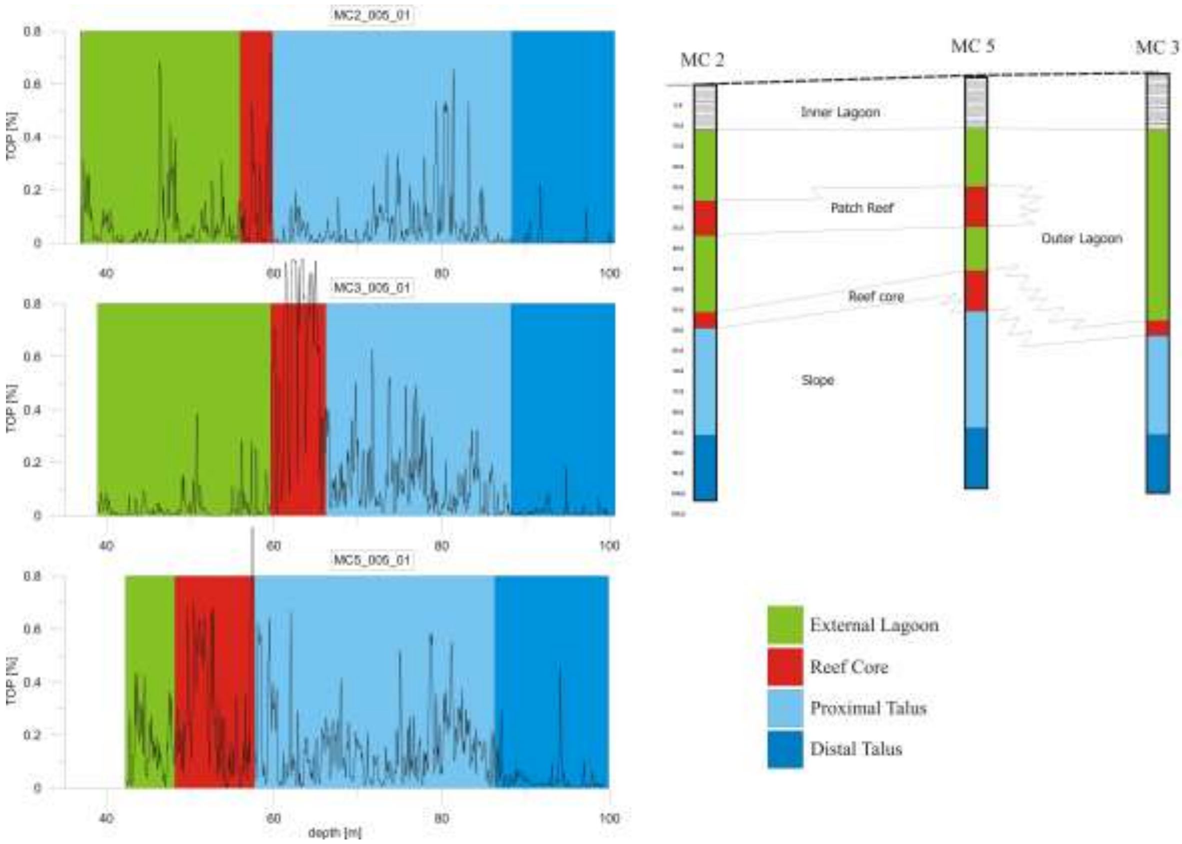

Figure 32. Lithological comparison between MC2, MC5 and MC3.

If the distribution of the recorded TOP is plotted for each borehole and lithofacies type separately, we get an idea of the lateral heterogeneity distribution for each lithofacies type. The comparison in the figure below yields the evidence, that within individual lithofacies types lateral heterogeneity distribution seems to be uniform.

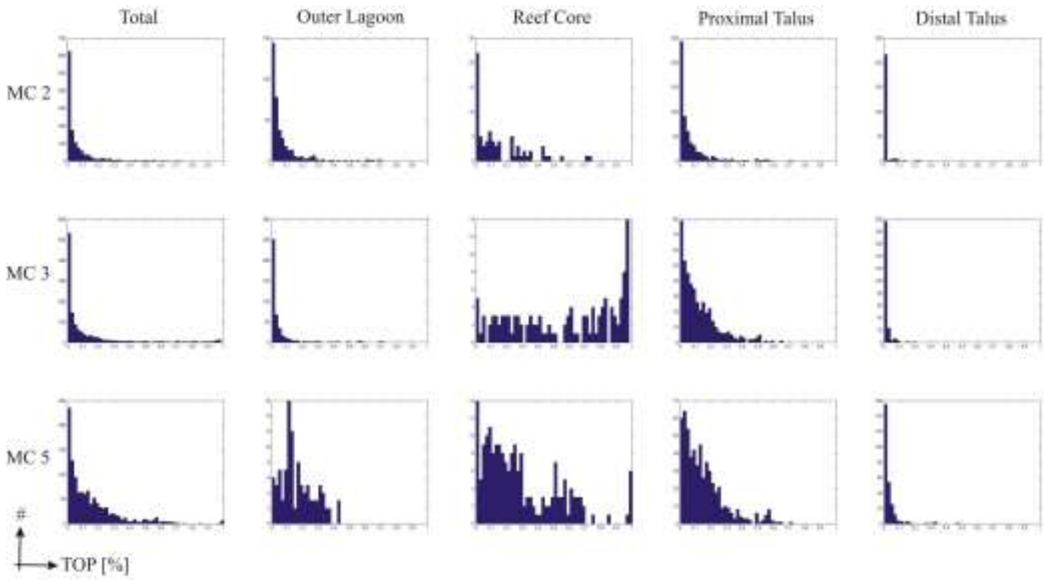

Figure 33. Comparison of distribution of reefal facies in MC2, MC3 and MC5.

Quite homogeneous distributions are observed in outer lagoon and distal talus. Due to the small pore sizes in distal talus the resulting distribution is nearly a single spike. The distributions of outer lagoon and proximal talus follow the typical lognormal distribution. The reef core is the most heterogeneous lithofacies type, which is due to the large range of pore sizes occurring at cm-m scale. From these diagrams only lithofaciestypes could be determined already quite easily. These trends hence seem to be typical characteristics for the individual lithofaciestypes and their lateral variability seems to be moderate (with exceptions).

Work Package Number: 4
Core and fluid analyses (both sites)

Objectives and input to work package :

(a) Detailed microstructural description of the core and fluid samples at both sites,
(b) Petrophysical characterization with transport properties from µm- to dm-scale,
(c) Solid phase and fluid geochemical composition, with relation to fluid-rock interactions and spontaneous potential processes.

Tasks 4.1, 4.2 and 4.3 were initiated in 2003 following the coring of the EXS and SWS field sites. Task 4.4 continues from year 1. D4.1 through D4.3 have progressed during 2004, with the assembly by partners 1, 3 and 4 of a database going far beyond initial expectations. This development is justified by the importance of understanding and differentiating in the laboratory the processes by which the rock has evolved in the past, and those by which it might be influenced now by saltwater intrusion.

Partner 4 (University of Oviedo - Spain)

During 2004, the efforts in Oviedo have been focussed on the following tasks :

1. to complete and to finish the petrophysical studies with the Mallorca cores,
2. to begin the petrophysical characterization of the Ploemeur cores,
3. to design and to implement a multimedia database for loading the petrophysical results obtained in the WP4 of the ALIANCE project.

Mallorca cores

During the first months of the 2004, until the first arrival to Oviedo of the Ploemeur rock cores, the main task has consisted on completing the petrophysical characterization of the Majorca rock cores. Therefore, the analysis of the pore space structure and the hydraulic properties of the selected rock cores were finished. The final results have been presented in the Paris ALIANCE meeting (2004); in the Oviedo meeting (2005) all the results obtained in Montpellier and in Oviedo were jointly analyzed.

Ploemeur cores

In the petrophysical characterization of the Ploemeur rock cores, the following studies were performed: Preparation of specimens with different sizes and shapes; specific methods of preparation (impregnation with fluoresceine, cutting with low deformation sawing machines, etc.) were used. Those tasks implied laborious cutting manipulations and continuous subdivision of fragments. A ***documentation strategy*** of all the implied stages and specimens, as well as data obtained from each specimen has been established an added to the database.

Prior to any other study, the ***anisotropies and heterogeneities*** of the Ploemeur rock cores were evaluated using non destructive tests, direct transmission method of P-waves; the procedure was described in the 2002 Technical Report. Profiles of “times of flight” and “residual times” along the Plomeur cores have been obtained.

The ***void space structure*** of the rock matrix, at the μm- to cm-scale, has been characterised in terms of the following parameters: total porosity, open and closed porosity, effective and non-effective porosity, specific surface of fissures, fissure aperture, tortuosity, etc. The data so obtained, allows a more solid interpretation of: a) the ability of water for flowing through this igneous and metamorphic rock matrix and b) the character of its main water pathways. Different microscopical and instrumental techniques have been used for that characterisation. ***Hg-porosimetry*** has been used for evaluating the trapped, or non-effective, porosity as well as the overall hydraulic function of the effective porosity.

The evaluation of the ***hydraulic properties*** according to standardised tests implies a repetitive and tedious manipulation of a large number of specimens; those manipulations can very often introduce errors and they imply high costs in terms of technician's time. Therefore, non-standardized computerized instrumental equipments have been used. These equipments have already been thoroughly described in the scientific reports of 2002 and 2003. The results obtained using these non-standardised tests are comparable to those obtained using standardised tests.

As a guarantee for not introducing errors during the manual evaluation of the ***hydraulic properties*** according to standardized tests, which implies a repetitive and tedious manipulation of a large number of specimens, non-standardized computerized instrumental equipments have been used. These equipments have already been thoroughly described in the scientific reports of 2002 and 2003. The results obtained using these non-standardised tests are comparable to those obtained using standardised tests. The results up to now obtained in the Ploemeur rock cores are summarized:

- in the rock cores the Vp values oscillate among 4000-5300 m/s; those results are mainly lithology dependent: in schists 4000-4700 m/s and in granites 3400-5500 m/s. In both cases the altered rock cores obviously shows a clear decrease in Vp,
- the open porosity ranges from 0.8 to 2.6 %. In a general, it can be stated that the porosity of the schists is higher than the porosity in the granites, although, some altered granites present porosities similar or bigger than those for the schists,
- the hydraulic properties in schists and granites show a similar behaviour than that just described for porosity. The values of free water absorption and water saturation (by vacuum) are always very low, rarely overcoming respectively 1 % and 1,5 %. The most altered cores show the highest values. In the rock cores up to now studied, the free water absorption values are, in general, a 75% of the corresponding water saturation values.

Multimedia database for the petrophysical results obtained in WP4

A multimedia database for loading the large amount of petrophysical data obtained of WP4 has been designed and implemented; it is supported in Flash MX 2004 (Macromedia). All the numerical data, tables, charts, graphics, galleries of pictures, profiles, etc. have been integrated in this multimedia support. Links among the different fields of information have been established. Two main types of fields have been considered in the structure:

- **informative fields**, mainly focussed towards the general objectives of ALIANCE and those more specific of WP4. The petrophysical methodology, the used standards, sample preparation and documentation, description of properties.
- **data fields**, with all petrophysical data ordered in thematic sub-fields.

One of the main activities of partner 4 during the 2005 extension period will be the loading in this multimedia database of all the obtained data. The preliminary results have been presented in the Paris ALIANCE meeting (2004). A meeting to be held in Oviedo in February 2005 is planned to crosscorelated and discuss the results from the different groups. An updated copy of the results has been transferred to the ALIANCE coordinator.

<u>Partner 1 (ISTEE Montpellier - France)</u>

Petrophysical characterisation of basement rocks at the EXS

A set of representative samples of fresh schists and granite from the B1 and D2 cored intervals in Ploemeur has been assembled in order to provide the necessary basis for field test experiments. In 2004, the petrophysical investigation of this set of minicores has continued from that accomplished in 2003. This included the making of thin sections, the deployment of a more precise measurement of wet samples with a technique designed for very low porosity rocks (Melnyk and Skeet, 1986), the achievement of electrical measurements with the determination of formation factor (FF), surface conductivity (C_s) and cementation factor (m), as well as the measurement of V_p and V_s in dry and saturated conditions at 500 kHz.

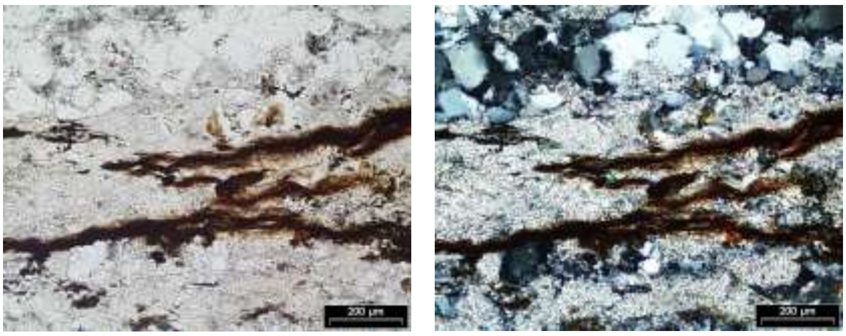

Figure 34. Iron oxide staining of a fracture in fresh schist matrix from B1 (21.9 m) under non polarized (left) and polarized light (right).

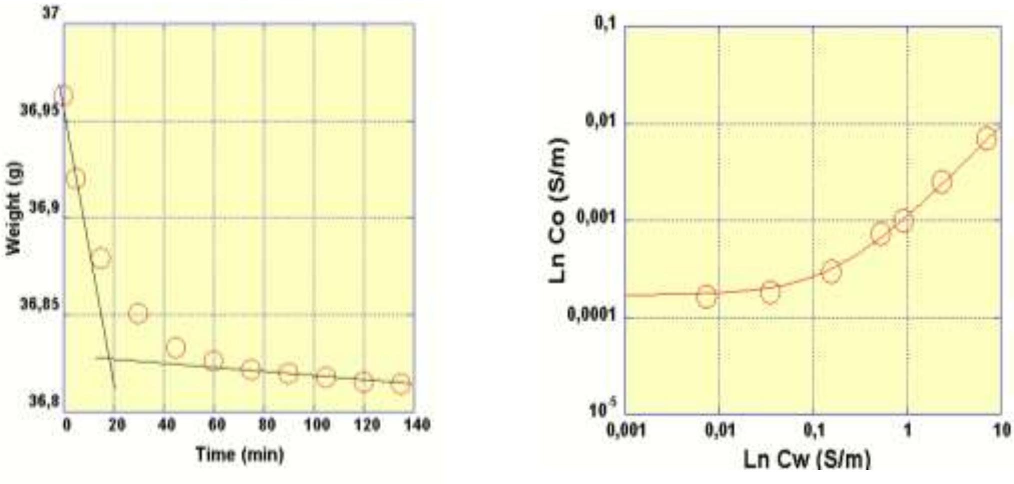

Figure 35. Wet weight measurement at 65.7 m in B1 after Melnyk and Skeet (1986; left), and electrical diagram at 55.2 m in B1 to derive FF = 1079 and Cs = 169 µS/m (right).

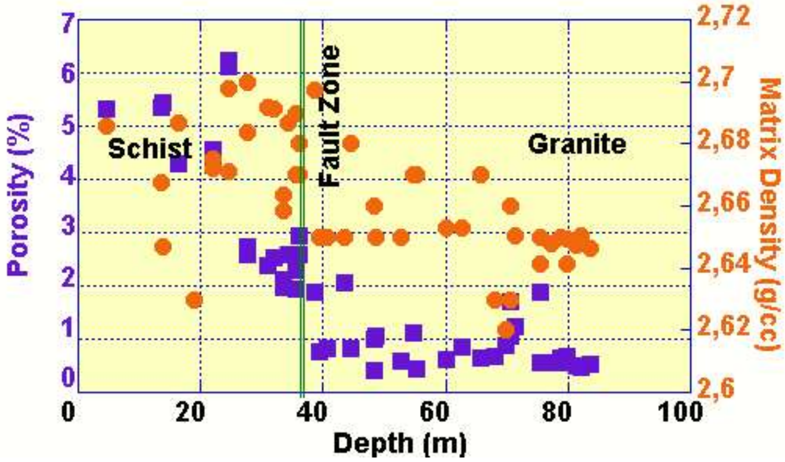

Figure 36. Newly derived porosities (with lower values) and grain densities for B1 cores.

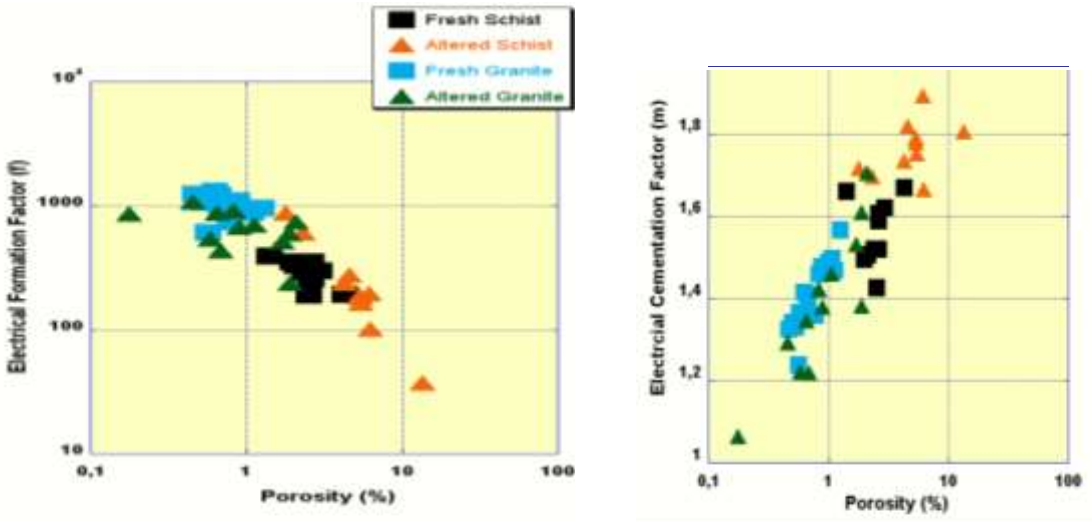

Figure 37. Formation factor (left) and cementation index (right) as a function of porosity in B1, showing linear relationships, hence small scale alteration processes.

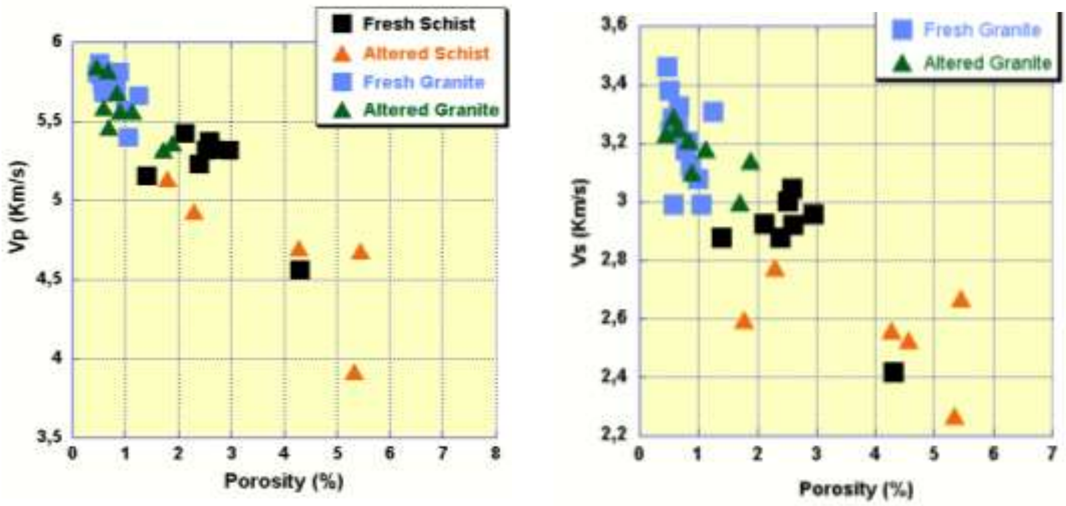

Figure 38: V_p and V_s measured satured at 500 kHz and room conditions for B1 samples.

Petrophysical characterisation of reefal limestones at the SWS

The structure and transmissivity of the reef has been studied at mm to 100 m scale from the systematic recording of borehole geophysical measurements and images in each of the new holes, in-situ hydrological reference in MC2 and MC5. A set of representative 59 samples of reefal carbonates from the chosen reference hole (MC2) has been assembled in order to provide the necessary basis for field test experiments. In 2004, the petrophysical investigation of this set of minicores has continued from that accomplished in 2003. This included pore throat measurements from Hg injection for 14 samples, 50 permeability measurements, and 3à measurements of coupling coefficient between electrical and hydraulic processes.

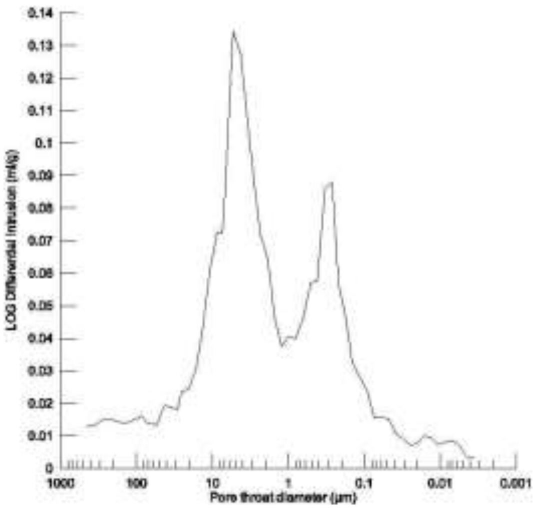

Figure 39. Bimodal pore throat distribution in a 35.0 % porosity and 2.83 g/cc density sample from 60.6 m in MC2, suspecting the presence of some dolomite in the section.

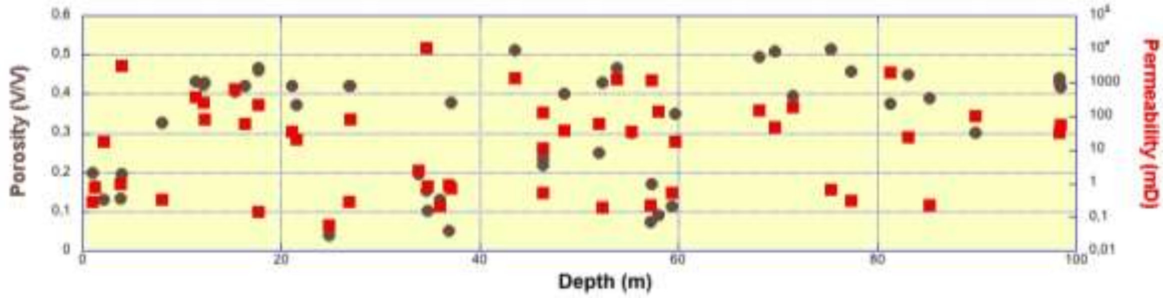

Figure 40. Porosity (brown) and permeability (red) measured on cm-scale plugs from MC2 and presented as a function of depth in the hole.

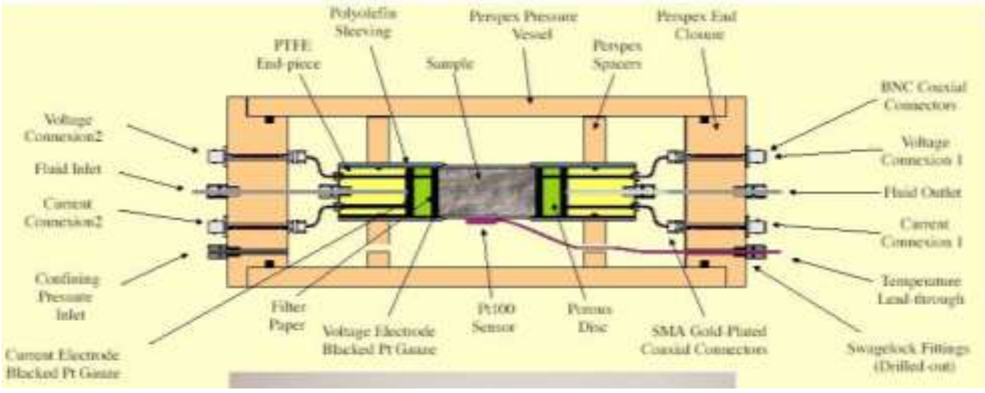

Figure 41. Cell contructed during "year 1" (2002) of ALIANCE to measure the coupling coefficient between hydraulic and electrical potential.

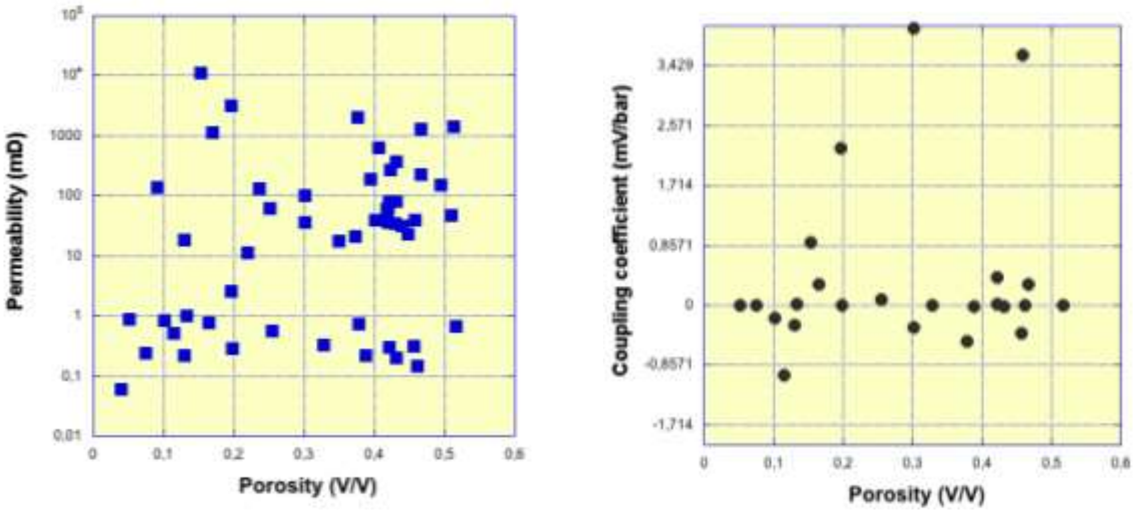

Figure 42. Crossplots of permeability (left) and coupling coefficient (right) versus porosity for samples from MC2. The coupling coefficient appear independant of porosity and close to zero in most cases in these reefal carbonates.

Plug flow experiments on MC2 samples

Plug flow experiments were continued in 2004. These measurements are often used to determine some parameters to constrain coupled geochemical and transport models. For that, some experiments have been realised at the University of Montpellier on different porous limestone from Campos site. The experiment allows the measurement of the permeability and the fluid chemistry changes in course of dissolution by reactive fluid using CO_2 enriched water as a proxy to saline-water controlled dissolution. The 3D geometry of the sample is determined using no destructive X-ray micro-tomography at different stage of the dissolution.

The sample presented here in this study comes from MC2 borehole, at 2.2 m depth. The carbonated rock is a secondary recrystallised due to near surface meteoric water circulation. The crystals are very fine, micritic to micro-sparitic; the porosity is high, about 30%; and the porous network is complex. CO_2 enriched water is flowing into the sample in the plug-flow apparatus; the temperature is constant and the confined pressure is controlled. The changes in permeability are monitored during the experiment using two pressure sensors set out upstream and downstream the sample (Figure 43).

Figure 43. Experimental set-up functioning at atmospheric pressure, 20°C, a partial pressure of CO2 of 0.1 MPa, for 9.5 mm diametter samples.

The changes in porosity are determined using the measurements of the cations removed by the sample during dissolution (Ca^{2+}, Mg^{2+}) and the 3D imagery. The changes in microgeometry are performed using X-Ray micro-tomography (ESRF synchrotron, Grenoble, France). The input and output fluids are collected for chemical analysis (Ca, Mg, Na, K) throughout the experiment. The rate of dissolution remains constant during the first hours of experiment (r=0.1 mmol.h^{-1}).

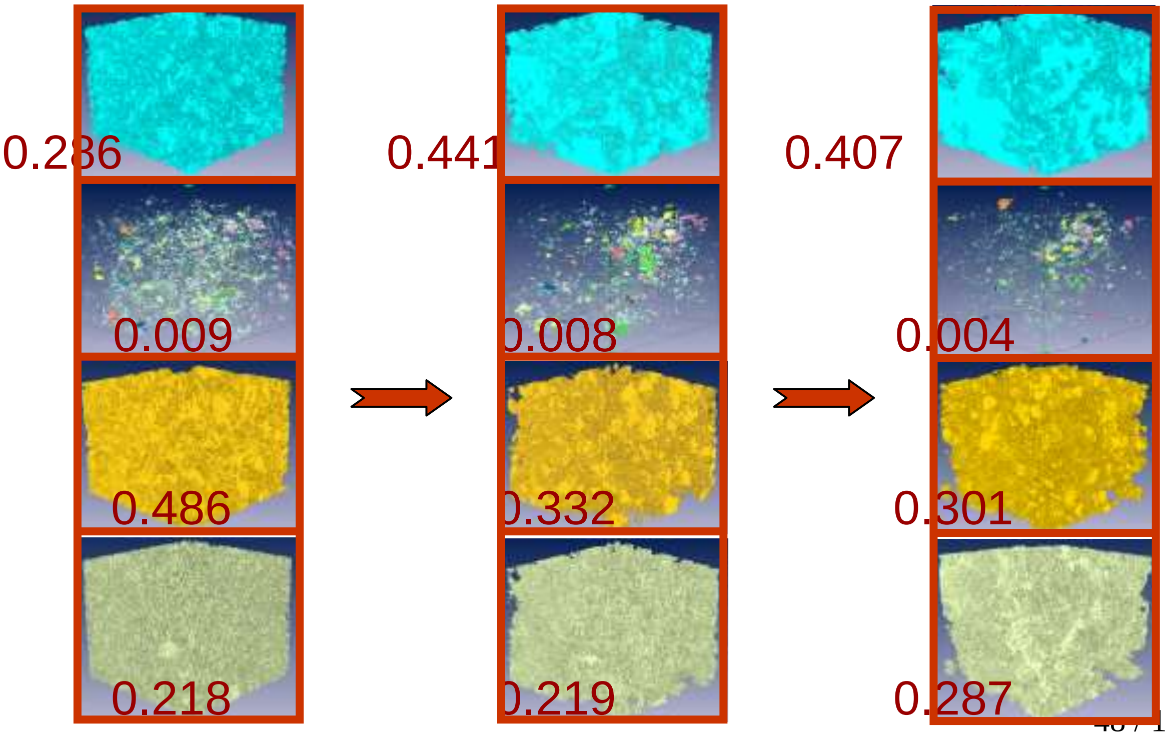

Figure 44. Left to right; evolution of the MC2 sample (from 2.2 m depth) after 1 hour of dissolution (middle) and 2 hours of dissolution (right), both at 50 ml/min. Image processing from X-ray tomography allows one to differentiate and quantify, from top to bottom: connected porosity (blue), unconnected porosity (colourfull), the calcitic solid phase (gold), and the microporous phase from past recrystalizations (beige).

Characterisation of structural changes

Microgeometry characterisation was performed using a non-destructive X-ray micro-tomography technique, with a 4.9 μm voxel size in this case. From image processing, it is possible to extract porosity, pore connectivity, the topology of fluid-rock interfaces, (reactive and non-reactive) surface changes.

In partial conclusion, the results from this study using the limestone from Mallorca show that the dissolution of the sample by water enriched in CO_2 is rapid. As a consequence, the permeability increases rapidly. While the connected pore space rapidly increases, the isolated pore phase tends to diminish. This pore volume increase comes from the dissolution of the matrix, with a reduction of more than 40 % of the initial calcitic phase. To the opposite, the microcalcitic phase tends to increase from precipitation overtime. Even more detailed analyses of the X-ray images lead to the description of the fluid-rock interface during the experiment (Figure 45). Further research will concentrate on quantifying these images in terms, for example, of surface topology, pore space tortuosity, and pore throat size evolution.

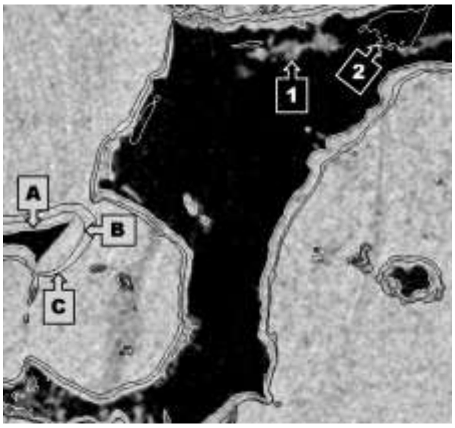

Figure 45. Evolution of the fluid-grain interface during the dissolution experiment (a to c).

Geochemical analyses of MC2 core

The isotopic composition of anion CO_3^{2-} is considered here as a source to study the downhole, hence "down section", evolution of lithology of carbonates. The ratios $^{18}O/^{16}O$ and $^{13}C/^{12}C$ are expressed as $\delta^{18}O$ and $\delta^{13}C$, according to:

$$\delta^{18}O = \frac{^{18}O/^{16}O_{ech} - {}^{18}O/^{16}O_{PDB}}{^{18}O/^{16}O_{PDB}} \times 1000$$

$\delta^{18}O$ and $\delta^{13}C$ are expressed in ‰, and with reference to the PDB standard reference.

The skeletons, calcitic cements, seawater and meteoric water have significantly different, hence caracteristic values for these two ratios. When parallel to each other, a change in isotopic composition cannot be traced (Bathurst, 1976). The successive diagenetic environments of this carbonates series can be deduced from geochemical analyses (particularly for carbon and oxygen) of cemented samples. The geochemical tracers of diagenesis indicate that each diagenetic domain is characterized by specific $\delta^{18}O$ and $\delta^{13}C$ values (Ebren, 1996). In order to reconstruct the successive diagenetic events of the Mallorcan reefal system, it was necessary to couple the petrographic analysis of samples with that of stable isotopes. These analyses lead to the characterization of pore waters that lead to the dissolution and precipitation of cements.

Stable isotopes of oxygen and carbon

These isotopes are often used to identify the diagenetic environment of reefal carbonates (Brand et Veizer, 1981; Quinn, 1991; Saller et Moore, 1991). The geochimical characterisation of meteoric cements in pleistocenes limestones such as those of Enewetak atoll (Saller et Moore, 1991) helps to study similar cements in older rocks, such as these studied in Mallorca. The $\delta^{18}O$ and $\delta^{13}C$ reveal the paleo-environment under which the cement was deposited, either marine or meteoric. The cements derived from a meteoric diagenesis show a relative enrichment in ^{16}O and ^{12}C, with values of $\delta^{18}O$ and $\delta^{13}C$ ranging from -6 to -1 ‰ PDB, and -12 to +2 ‰ PDB (Lohmann, 1988 ; Allan et Matthews, 1982), respectively. Negative values of $\delta^{18}O$ indicate, as a consequence, a diagenesis from meteoric water circulation. The $\delta^{13}C$ varies independantly, according to the source feeding the reefal system with carbon.

Changes of $\delta^{18}O$ as a function of $\delta^{13}C$ leads to the identification of the diagenetic environment to which the reefal sequence was submitted (Figure 46). The values of $\delta^{18}O$ are on the order of - 4 ‰ in MC2. These negative values are typical of a diagenesis from groundwater meteoric in origin. The ^{16}O enrichment of cements leads to these negative values. The $\delta^{13}C$ can underline a pedogenetic alteration process, revealing for example the presence of organic carbon from plants with negative values of $\delta^{13}C$ (Ebren, 1996). The typical $\delta^{13}C$ values of such a meteoric environment are negative but can be very variable, ranging in the case of MC2 from -6 ‰ to 0 ‰.

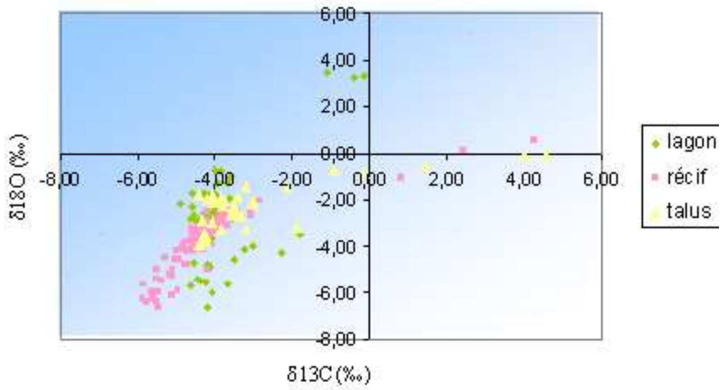

Figure 46. Cross plot of $\delta^{18}O$ and $\delta^{13}C$ measurements from the MC2 core.

The variations of oxygen and carbon ratios can be represented as a function of depth in the hole (Figure 47). These two diagrams show the evolution of geochemical data over the entire reefal sequence. The calcitic cements from meteoric water percolation are caracterized by a narrow range of $\delta^{18}O$ values, and a larger range of $\delta^{13}C$ values. These résults are similar to those obtained from the study of similar pleistocene carbonate systems such as those from Enewetak atoll (Western Pacific), Cat Island (Bahamas) and Yucatan (Saller et Moore, 1991).

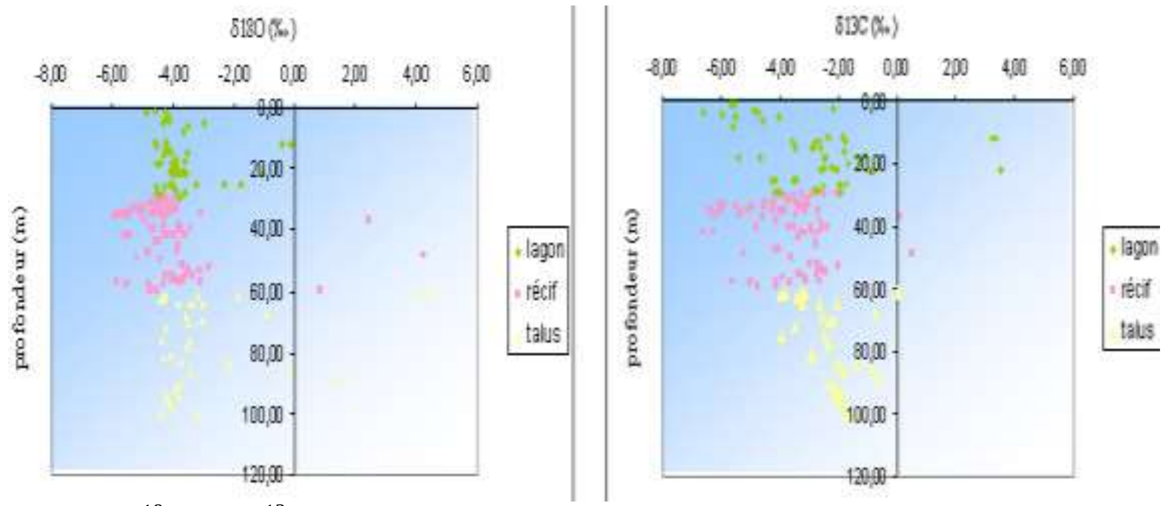

Figure 47. $\delta^{18}O$ and $\delta^{13}C$ as a function of depth in the MC2 hole.

The microscopic study of thin sections allows one to distinguish diagenetic from neomorphic cements. $\delta^{18}O$ and $\delta^{13}C$ values of these two crystalines phases (Figure 48) are different. The $\delta^{13}C$ values in MC2 are, in some cases, larger than that of the meteoric end-member. This reveals the presence of an equilibrium between meteoric pore water and the mineral phase (Meyer et Lohmann, 1985). The stable isotope values of the neomorphic end-member tends to migrate in the direction of the meteoric end-member (Figure 48). The diagenetic gradient extends from the neomorphic end-member (with calcareous sparite) to the meteoric one (with granular and drusy calcite cements). With mineral changes and cementation, the stable isotope composition of a grain undergoing diagenesis changes gradually from a marine signature to a meteoric one (Allan et Matthews, 1977, 1982).

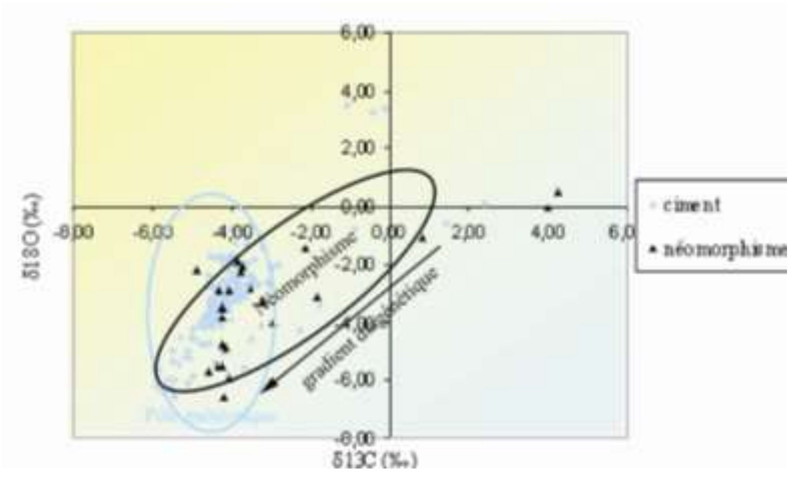

Figure 48. $\delta^{18}O$ et $\delta^{13}C$ fractions of ciments from the MC2 core, and expression of the diagenetic gradient between two cristalline end-members.

Partner 3 (ETH Zurich - Switzerland)

Microscale pore structure in limestones

Appropriate sampling for physical measurements is very important for representing the reservoir in highly heterogeneous cases, like a reefal limestone (Al-Hanai et al. 2003). It is important to understand and define the different scales of heterogeneity so that lab measurements and field-scale data can be compared correctly. Quantifying pore space using digital image analysis (DIA) on thin sections is well known and has been widely used (Ehrlich et al. 1984). Most methods however are somehow limited, because they use images only at a finer or larger scale. The method of DIA which covers a wide range of pore sizes over several orders of magnitude by integrating porosities measured at smaller scales into the values assessed at larger scales is relatively new (Anselmetti et al. 1998). They found, that permeability appears to be mainly controlled by the macropore shape in high-permeability samples and by the amount of intrinsic microporosity in the low-permeability samples. Micro-intercrystalline porosity contributes significantly to reservoir quality in many wells (Montgomery et al. 1999). A large range of scales from micropores up to larger pores can alternatively be assessed by using MICP as done by many authors but is a very time consuming process (Bliefnick and Kaldi 1996). In order to cover the whole range of scales up to the next larger log scale, within the framework of this thesis thin section scans will be introduced additionally. Thin section scans allow for gathering information about the pore structure, which is of a comparable scale as data from 1 inch plugs.

Digital image analysis on thin sections

On microscopic scale data is acquired by digital image analysis on SEM (scanning electron microscopy) pictures, thin section pictures and thin section scans. The introduction of thin section scans extends the technique of Anselmetti et al. (1998) in order to include larger scale pores that are very common in karstified reefal limestones. ESEM data is not yet available and therefore TOP-values do not include microporosity, which can be even higher than the one measured by the optical microscope only. Plug data, which is of a comparable investigation scale of course does include all types of porosity (effective, trapped and closed down to the micro-scale) and will be discussed in detail in the next paragraph. Let’s now first concentrate on the features of the porespace observed on simple thin sections (see figure below). The inner lagoon shows the lowest total optical porosity (TOP), which is mainly of intergrain type. The sediments there are isotropic and homogeneous at thin section scale. Vadose blocky cements occlude most of the intergrain pore space. Within outer lagoon TOP can reach up to 50% and consists to a large extent of molds from shells and other dissolved aragonitic organisms. Pore structure is anisotropic but homogeneous distributed. Lowest porosities are observed within the framework of recrystallised reef core. Vuggy porosity leads to a heterogeneous pore structure. Proximal and distal talus both exhibit highest porosity of the whole reef complex. It is mainly of intergrain type and micritic cements or crusts are common. Close to the reef core as well moldic porosity is present. Whereas the upper part was affected by turbidity currents during storm events, which lead to an isotropic and heterogeneous pore structure, lower parts were rather affected by a directional and slow deposition which leads to the observed anisotropic and homogeneous pore structure.

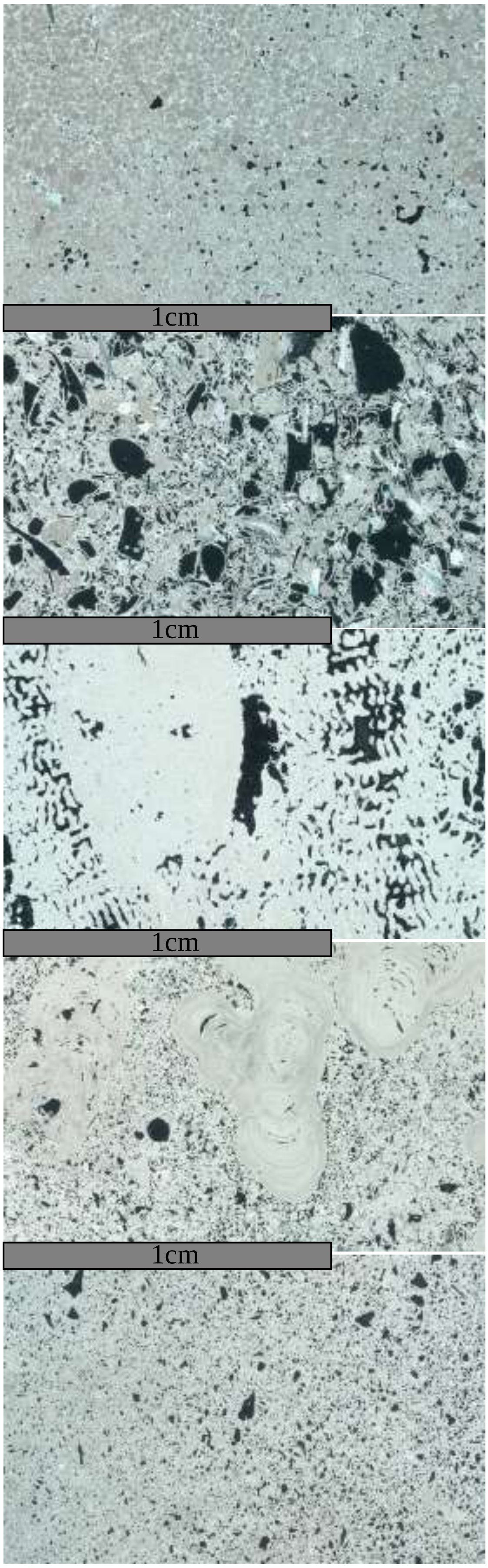

Sample of inner lagoon in borehole MC2 at 1.7 m depth, oolithic grainstone with shell fragments, restricted ecology, important sparitic cement, mainly intergrain porosity, some intragrain porosity and a few vugs, fabric isotropic and homogeneous, TOP of 4%

Sample of outer lagoon in borehole MC2 at 14.4 m depth, skeletal grainstone, abundant red algae and forams, ecology not restricted anymore, micritic cement, moldic and intergrain porosity, fabric anisotropic but quite homogeneous, TOP of 37%

Figure 49. Variability of rock types found in thin sections from MC2 core.

Sample of reef core in borehole MC2 at 30.5 m depth, framestone built by corals (Porites) with extensive borings, sparitic cement which partly occludes porosity, growth-framework porosity with important vugs, fabric is highly heterogeneous, TOP of 19%

Sample of proximal slope in borehole MC2 at 70.9 m depth, floatstone consisting of encrusting red algae in a grainstone-matrix, micritic cement, mainly intergrain and some moldic porosity, fabric is isotropic and heterogeneous, TOP of 13%

Sample of distal slope in borehole MC2 at 88.3 m depth, grainstone, fine grained, with molds of shells, only echinoids are preserved, exclusively micritic cement, mainly intergrain porosity and some moldic porosity, fabric is anisotropic and homogeneous, TOP of 16%

Anisotropy can be the result of a preferred orientation during sedimentation of the grains, e.g. currents, gravity, elongated fossil debris, topography and so on or the result of a directional growth of cement within the primary pore space due to fluid gradients or gravitational forces (vadose cements). The anisotropy can have a large influence on the flow behavior (permeability) of a porous medium making it necessary for example to take the orientation into account during permeameter test in the lab (small scale). Another effect could be distortion of the drawdown cone during pumptests on the large scale. In order to check this effect from the DIA-data a dataset of the angles with the following constraints has been extracted: Particles must exhibit a minimum size of 16 pixels and all edge particles are excluded. The measured angles describe the orientation of the large axis of an ellipse fitted to a single pore.

Digital image analysis revealed a clear anisotropy of the pore space of grainstones sedimented above wave base level of external lagoon as well as of grainstones and packstones of distal talus. Within this lithofacies types water dynamics led to a preferred orientation of elongated grains like peloids and fossil fragments which directly affected the intergranular pore space. The figure below shows two examples of anisotropy-measurements done by digital image analysis on full thin section scans (1.5x2 cm). On the right side a sample shows an overall isotropy for pores with diameters between 10 and 0.05 mm. The partition of the dataset into three different pore size classes reveal, that the pore-fabric is anisotropic for the pore size class 1-0.1 mm and isotropic for the pore size class 0.1-0.05 mm. The overall pore-fabric is isotropic. The main information out of this is, that even the hole sample seems to be isotropic, at an intermediate pore size (1-0.1 mm) elongated pores with a preffered orientation seem to occur and can be pontentially important for the permeability behavior of this rock type at the rock matrix scale. This proves that even on thin section scale isotropy can vary considerably for different investigation scales.

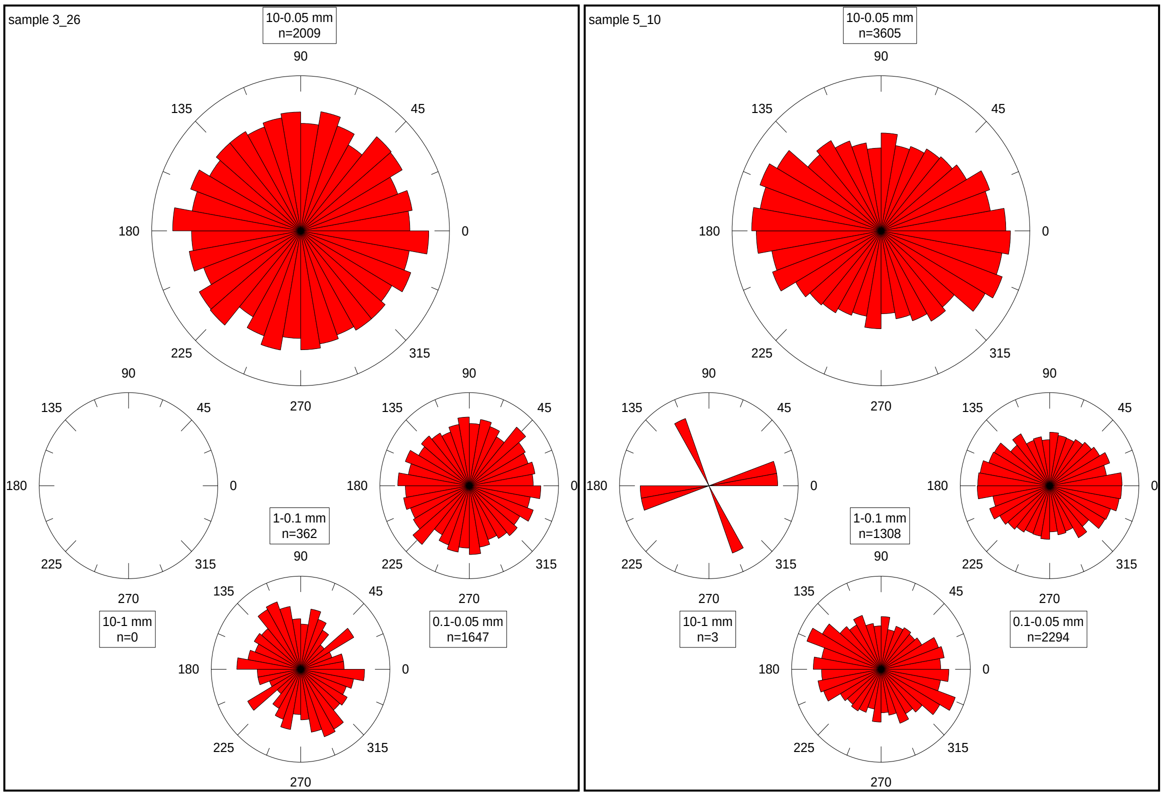

Figure 50. Pore space analyses from thin sections.

The sample on the right hand side on the other hand is anisotropic for all three pore size classes and the preferred orientation does not seem to change significantly between the individual pore size classes. The anisotropy could be detected not only by pore orientation plots, but also by the use of the autocorrelation function (ACF) which additionally provides information about heterogeneity, average grain size and grain shape. The big advantage of using the ACF is that the image does not necessarily have to be segmented prior to the analysis. The image below is from the same sample like above the rose diagrams on the right hand side. The binary image (1) shows that the porosity seems to be distributed quite homogeneous. From the eye only not anisotropy can be seen. The inset in the lower right corner represents the relative size of the ACF from the nucleus (2). The nucleus shows

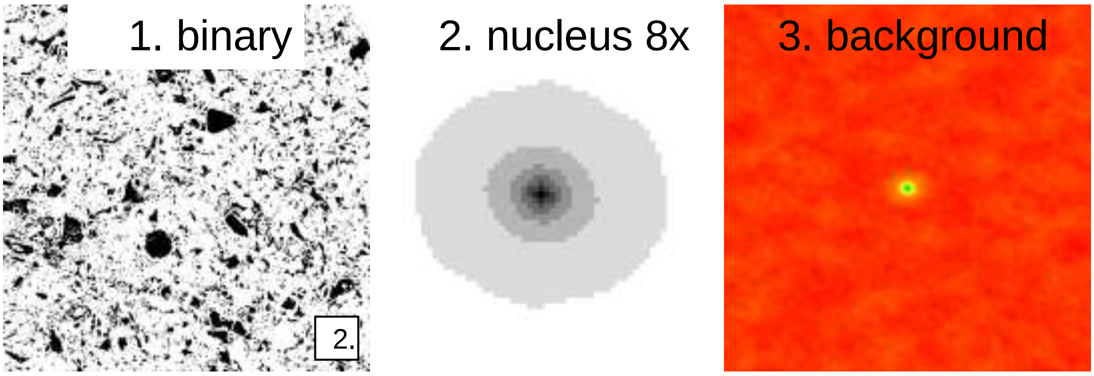

Figure 51. Image analysis for pore space quantification from thin sections.

anisotropy for all pore sizes and elongated, elliptical pore shapes. The background shows only weak correlation and quite a regular structure, which points to quite homogeneous porosity distribution on the imaged part of the thin section. Summary of the preliminary results obtained from digital image analysis on thin sections:

Lithofacies	Type of Porosity	Typical TOP from TS-Scans	Isotropic - Anisotropic	Homogeneous - Heterogeneous
Inner lagoon	Intergrain	0 - 20	Isotropic	Homogeneous
Outer lagoon	Moldic/Intergrain	20 - 45	Anisotropic	Homogeneous
Reef core	Framework	15 - 35	-	Heterogeneous
Proximal slope	Intergrain	20 - 55	Isotropic	Heterogeneous
Distal slope	Intergrain	25 - 50	Anisotropic	Homogeneous

Plug measurements

On 140 plugs total porosity has been measured by determining the bulk density of the samples in combination with an assumed matrix density of Calcite (2.71 g/cm^3) or Dolomite (2.85 g/cm^3). The measured values range between 3.8% measured in inner lagoon lithofacies and 52.7% measured in outer lagoon lithofacies. The measured total porosities are indicating an upper limit of the real matrix porosity at these locations if the mineralogy is determined correctly. The main reason for this is the loss of rock material during sample preparation (drilling, polishing and drying). The total plug porosity expresses the real (physical) porosity on the cm-scale which can be used for direct or indirect comparison to optical porosity and porosity from logs. Of course in most cases a direct comparison is not valid due to the different inherent scale of investigation of each method.

It is indispensable to analyze such data for each lithofaciestype separately in order to avoid sampling bias. The samples have not been taken at a constant sampling interval, which is in most cases anyway close to the Nyqvist frequency (Corbett 1998). Here the approach of genetic petrophysics has been chosen. This approach is considering the geological knowledge thus sampling was performed at relevant zones. From MC2 samples have been taken in order to compare the results to data from Oviedo. MC3 and MC5 have been intensively logged and their cores are stored in Zurich. In MC3 the focus has been put on the outer lagoon and the distal talus. In MC5 a dense sampling has been carried out on the proximal talus section.

MC2 borehole

MC2 has been sampled at 17 levels, mainly in outer lagoon and reef core. Measured values are highest in distal talus, above 40% and proximal talus, slightly below 40%. Within outer lagoon values occur over a large range from 10-45%. The crystallized reef core exhibits very low porosity values, between 5 and 15 %. From the distribution of the porosity values a clear distinction of the main lithofaciestypes can be made but of course the data set is too small for a reliable statistical analysis.

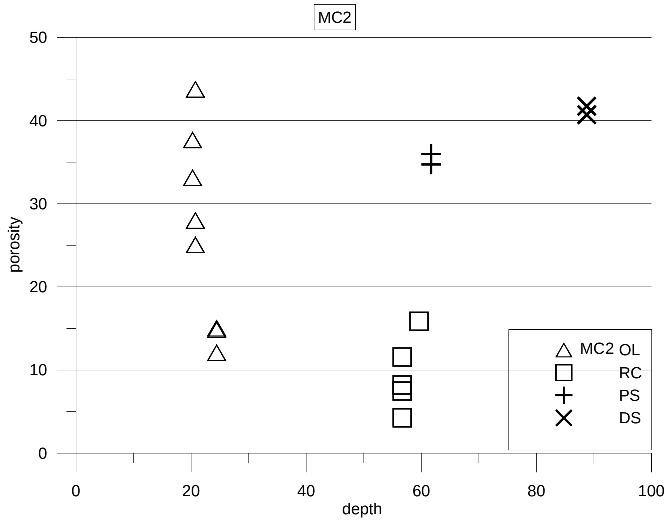

Figure 52. Porosity as a function of depth in MC2.

MC3 borehole

For MC3, a total of 45 measurements are available. Lowest values have been recorded within inner lagoon (around 10%). A sharp transition to outer lagoon raises the values to 40-50%. In contrast to MC2 the values in outer lagoon are quite uniformly lying within this band and this over a distance of 35 m! Reef core again exhibits lower porosities, around 20%. In the proximal talus values ranges from 15 to 45%. Distal talus exhibits values at a higher level.

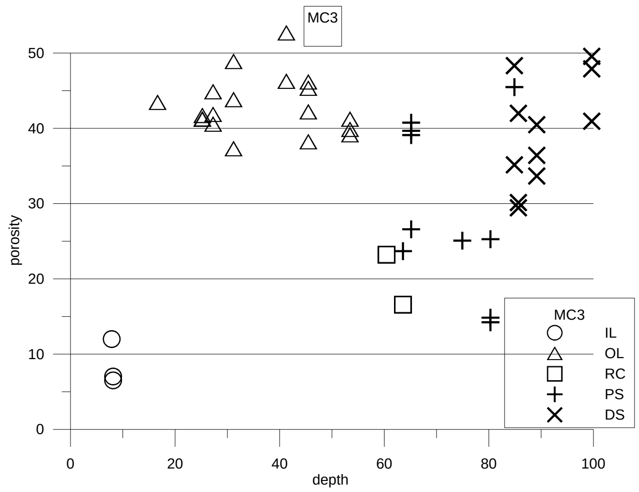

Figure 53. Porosity as a function of depth in MC3.

MC5 borehole

78 measurements have been made on this borehole, most of them in the proximal talus. Lowest porosities again have been recorded in inner lagoon environment. Much higher values between 30 and 50% seem to be typical for outer lagoon and the embedded patch reef shows porosities from 10-40%. This is due to the partly recrystallized rock material (coral patches) which is inter-filed with grainstones from the outer lagoon. Reef core again exhibits values between 15 and 20%. Surprisingly below the reef in the adjacent proximal slope even lower values are recorded (below 10%). This could be due to the there observed high velocity zone (see tomograms). Like the seismic tomograms as well ERT-data indicates very dense and low porous material. The lower part of the proximal talus again exhibits high porosity in the range of 30-50%. Values in distal talus are very uniform lying within a thin band (40-45%).

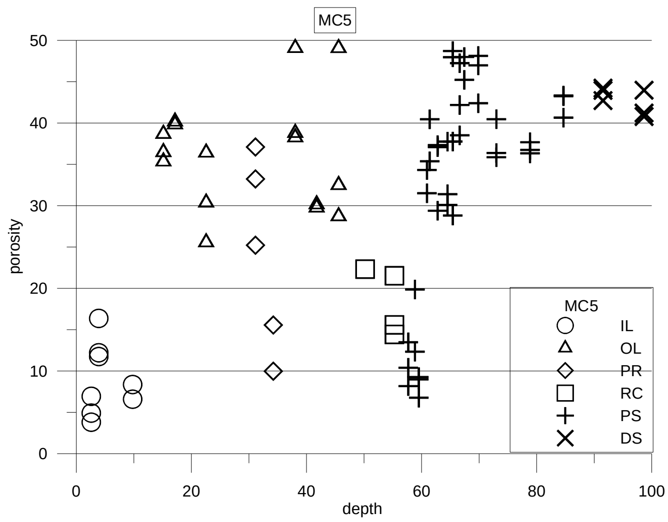

Figure 54. Porosity as a function of depth in MC5.

Statistics on the plug data

In order to get characteristic features for each lithofaciestype a simple statistic procedure has been applied. Each borehole has been divided into its lithofaciestypes and for each individual type the number of measurements, the average of the measurements made and the standard deviation has been calculated. The following plot shows the average values measured on each borehole for each lithofaciestype:

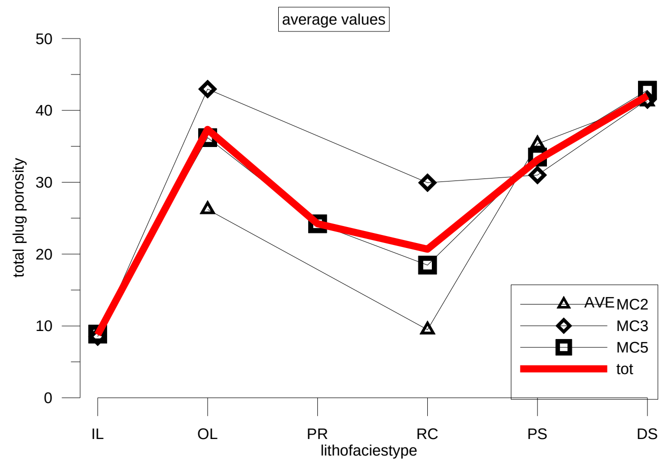

Figure 55. Porosity according to lithofacies in MC2, MC3 and MC5 (IL = inner lagoon; OL = outer lagoon; RC = reef core; PS = proximal slope; DS = distal slope).

Inner lagoon sediments exhibit the lowest values of the whole reef complex. A clear distinction can be made between the two lagoonal lithofacies types. Outer lagoon varies quite heavily from borehole to borehole. The mean at MC2 lies about 20% lower than at MC3. The patch reef at MC5 has a slightly higher mean than the normal reef core values. In reef core values vary again quite heavily. MC2 shows about 20% lower values than MC3. MC5 like at outer lagoon lies in an intermediate state. Reef core porosity is in average clearly lower than the porosities of outer lagoon or talus sediments. Only inner lagoon is still less porous. Below the reef core porosities increase remarkably to a mean value of about 30-35%. Here as well as in the distal talus with porosities above 40% the variability between the 3 boreholes is low.

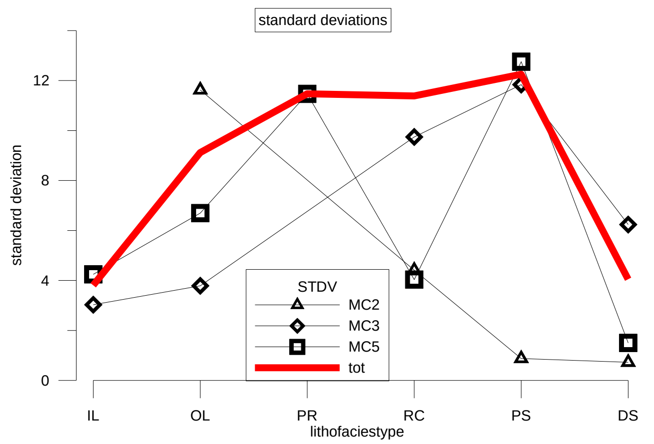

Figure 56. Standard deviation of porosity according to lithofacies in MC2, MC3 and MC5.

If we regard the standard deviations, the interpretation gets bit more refined. Low standard deviations (around 4%) are observed at inner lagoon and distal slope. Relatively high standard deviations are observed in the other lithofaciestypes (up to 12%). This is surely due to the inherent heterogeneity of the reef complex at this scale of investigation. Especially the distal slope is quite homogeneous and therefore most measured porosities lie more or less within a narrow band. High standard deviations in outer lagoon and proximal slope are explained by rudstones originating from storm events, which typically consist in reef debris and shell fragments. In the reef core large standard deviations originate from the unevenly distributed, little cemented internal sediment, which has intruded between the strongly recrystallized framework of the coral heads.

Due to the large number of measurements at MC5, this borehole dominates the curves averaged over all boreholes! The figure below shows the number of measurements for each lithofacies type carried out at each borehole. A significant number of data is available for outer lagoon and proximal slope. The dense sampling at the proximal slope of MC5 is due to a closer inspection of the zone right at the reef bottom in order to explain the anomalies observed on the seismic tomograms.

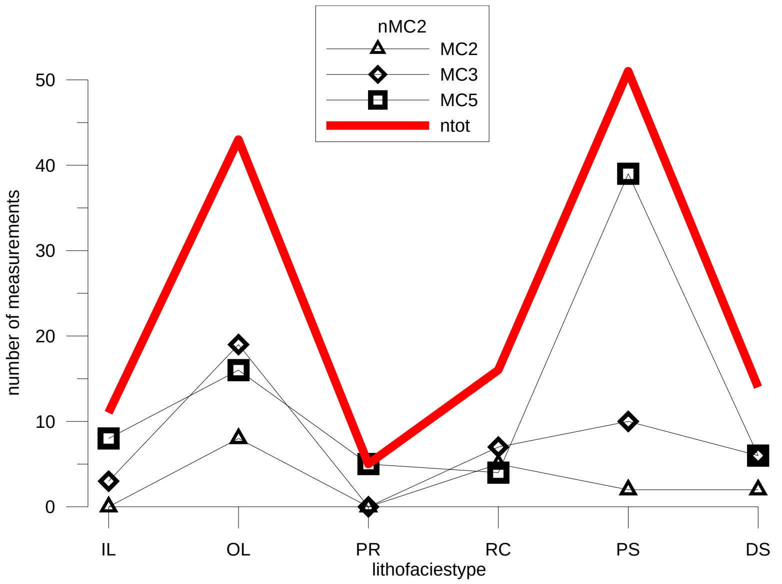

Figure 57. Total number of porosity measurements according to lithofacies (in MC2, MC3, MC5, and total).

The MC5 borehole where a total of 78 measurements on mini-cores at 29 different depths have been performed is the most suitable for creating a synthetic porosity log. On most halve core scans several (up to 4) measurements have been performed in order to characterize the heterogeneity. Most plugs were drilled horizontally but whenever possible, a vertical sample was taken as well. Min, max and average curves have been created in order to check the variability of the plug porosities with depth. The figure on the next page shows on the left side min and max, which encase the white band of measured porosities at corresponding depths. In the middle follows the simplified geological profile of MC5 on which inner lagoon is violet, outer lagoon green and patch reef or reef core red. Proximal talus with steep beds and distal talus with a moderate slope are not colored. The curve on the right side is indicating the depths, where the plugs have been extracted and the corresponding averaged porosity value. Tomography shows, that the high velocities do not occur exactly at the reef core, but are in some cases at least shifted towards the proximal slope. This can also be seen in the plug porosity data where lowest values (around 10%) are not measured within the reef core, but slightly below it in proximal talus. The first 10-15 m below the reef core show an interesting porosity behavior, which has also been indicated by sonic and induction measurements. Characteristic features of this zone are alternating rudstones and grainstones, enhanced moldic porosity due to circulating fluids and a higher amount of originally aragonitic reef rubble and solitaire corals. In contrast to lower parts of the reef core this zone is not karstified at all. The heterogeneity distribution along the borehole (cm-dm-scale) is nicely displayed in the figure. In homogeneous zones like inner lagoon and distal slope the band bounded by min and max is narrow. Especially in outer lagoon, but also in reef core and in the upper part of proximal slope the bandwidth is much larger and irregular. Although not all lithofazies types are sampled with a sufficient density, these trends seem to support the preliminary hypothesis. In the next chapter the curves will be supplemented with measurements from the He-pycnometer (effective porosity and closed porosity).

Lowest porosities of the reef complex have been measured in IL and RC. Highest porosities have been measured in DS with slightly higher values than PS and OL. These very high values in DS can to a large extent be explained by the grain size or pore size distribution, which is very uniform. If a uniform grain size is assumed with ideal spheres the porosity in the space in between is highest. This effect is theoretically independent from the grain size. Due to its distal location only one dominant grain size occurs, which of course is very small. A non uniform grain size distribution in which different sizes occur which can fill out easily the space between the larger spheres leads doubtless to a less porous sediment. This is the case for the PS, where storm events and its location very close to the main carbonate factory leads to a variety of grain sizes. Of course the ideal grain (a sphere) will never be present but the principle remains the same for more complex grain shapes. In an environment with lots of moldic porosity, where the grains have fully been replaced by molds, the grain size distribution is somewhat equal to the pore size distribution. The mentioned effects can therefore be studied by pore size distributions, obtained by DIA on thin sections. Total porosity of plug data will not be comparable to TOP from thin sections as long as microporosity is not incorporated into the digitally analyzed values. Especially in MC5 PS close to RC exhibits very low values (high-v-zone!). This phenomenon has been recorded in other boreholes with other techniques (sonic, induction) as well and seems to be mainly affected by the presence of the overlying reef core which produced a high amount of aragonitic reef rubble and gave rise to intensive fluid circulation. OL-porosity in MC2 ranges from 10-45% and in MC5 from 30-50%. In MC3 with thick lagoon (more than

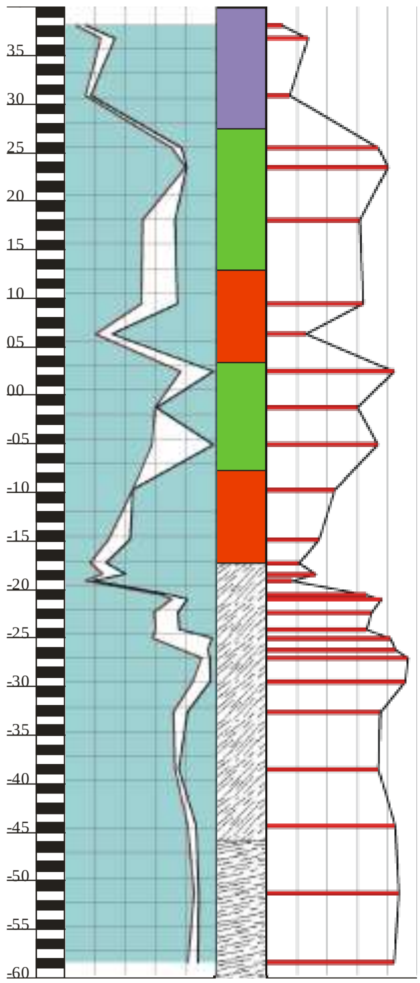

35 m) and no patch reef a very uniform distribution at a high level between 40 and 50% has been recorded. The porosity values and their distribution within a lithofacies-type are therefore strongly controlled by the local reef geometry or the sedimentation stage of the reef complex. For IL, PS and DS the latter seems not as important as for OL an RC! Mean values for individual lithofacies types measured at the 3 boreholes are similar for IL, PS and DS. For both, OL and RC much lower values have been measured at MC2 than at MC3. The RC in MC3 is not as developed as in the other boreholes. Furthermore no patch reef occurs which could give raise to recrystallization processes. The average curves show similar shapes even if they lie on different levels. In other words: If the OL-porosity is high, also RC-porosity is high (MC3). MC2 lies at a low level and MC5 at an intermediate level. The question arises whether this is due to a genetic process. In MC3 RC is thin, low lying and covered by thick OL. The intermediate MC5 is spatially and from a porosity point of view located between MC3 and MC2! RC here is much more developed and a remarkable PR occurs within OL. In MC2 RC again is low lying and thin but like in MC5 capped by a PR. MC2 and MC5 are probably closer to a low order aggradational stack which is located towards the sea and which produces few graded sediment? Homogeneous zones (concerning porosity) like IL and DS exhibit low standard deviations for porosity measurements. This is also expressed by the thin band of measurements at these lithofacies types in MC5. OL, RC and PS, which exhibit high standard deviations are affected by deposits from storm events and unevenly distributed recrystallization. PS shows similar averages for all boreholes but also very high standard deviations (except MC2, where dataset is too small). Due to the depositional cyclicity with storm events and background sedimentation a sufficient number of measurements lead to similar average values at high individual variability. In other words the depositional pattern remains the same. The synthetic figure which compares geology to the min, average and max plug-porosity-curves nicely displays that the bandwidth (max-min) not always exactly outlines the geological lithofacies borders: The border IL-OL is consistent with the geological border. In OL due to its inherent heterogeneity the bandwidth is mostly quite large. The boarder OL-RC is marked through a reduction of the local range. The transition RC-PS lies lower than the geological one and the transition PS-DS from plug data only would be set about 10 m higher than the original one. A large bandwidth implies a high degree of heterogeneity at cm to dm-scale. The distribution of hetereogeneity at this scale seems not only to be controlled by primary processes like lithofacies distribution (reef geometry) but also by secondary processes e.g. diagenesis, recrystallization. This fact remarkably complicates the prediction of fluid flow within the reservoir.

Hydrogeochemical evaluation at Ses Sitjoles

For the evaluation of hydrochemistry two different data sets are used:

1) spatially distributed data collected mainly during one field campaign
2) temporally distributed data collected during the upconing experiment

<u>Spatially distributed sampling</u>

According to the idea of setting up a test site within a saltwater intrusion zone, the groundwater composition at the Saline Wedge Site Ses Sitjoles was believed to be spatially different. Following the results of the fluid logging campaigns, the boreholes were sampled in three different depth zones during a single field campaign:

- near the groundwater table at 42 - 50 m bgs
- in the middle of the transition zone at 65 to 68 m bgs

- in the saltwater zone near the bottom of the boreholes in 80 – 87 m bgs

The objective was to characterize the hydrogeochemical variation of groundwater composition both laterally and vertically at site scale. Overall 28 samples from 10 boreholes and one sample of seawater for comparison purposes were taken.

Sampling procedure

A 500 ml groundwater bailer with a controllable closing valve was used to obtain groundwater samples at different depths. The bailer was lowered to the desired depth and the valve was opened. After waiting 3 minutes to allow the groundwater to enter the bailer, the valve was closed and the bailer recovered. The sample was split in two 50 ml PE-bottles for subsequent laboratory analysis on main ions and a measuring cup for on-site measurements of phyico-chemical properties (electrical conductivity, temperature, acid capacity, base capacity, oxygen content). The PE-bottles were cooled and analyses were performed later at the ETH hydrochemistry lab in Zurich.

Data processing and evaluation

After checking all analysis for electro neutrality balance three samples with errors >5% were excluded from the evaluation. Lateral differences in groundwater composition at site scale are not present. The plot of electrical conductivity EC (µS/cm) resembles the fluid logs with the EC-probe (Figure 59) In principal, two different groundwater types are present: the top-type in the uppermost 15 m of the aquifer with EC around 4000 µS/cm, and the bottom-type at depth >80 m bgs with EC around 56’000 µS/cm. In between a transition zone exists between 60 and 75 m bgs.

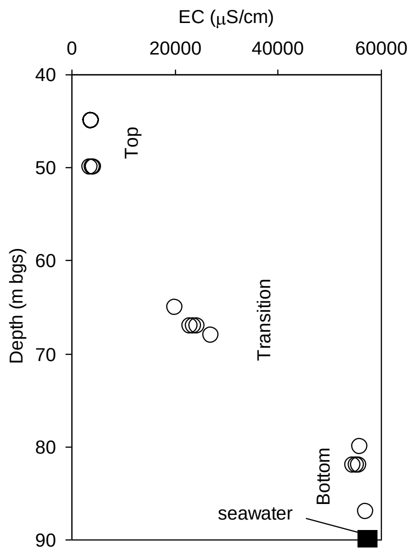

Figure 59. Transition from freshwater to seawater with depth of sampling.

Even in the highest part of the aquifer the groundwater contains more than 2 g/l total dissolved solids and cannot be termed “freshwater” in hydrogeochemical classification. This groundwater has already undergone alteration processes on its way from rainwater in the recharge area to the field site through the unsaturated zone and the groundwater passage. The EC of the bottom samples is very close to seawater at 55’000 to 57’000 µS/cm, but the composition is different. This shows that the bottom groundwater as compared to seawater is enriched in calcium and bicarbonate and depleted in magnesium. Furthermore, the ratio of

Na/Cl increases with depth to an extent that the bottom groundwater has even higher values than seawater. Mixing of top-type groundwater and seawater can therefore not be the only process to generate this composition of the bottom-type groundwater. Processes under consideration are:

- mixing of seawater with top-type groundwater,
- dissolution of calcite → increase in Ca^{2+} and HCO_3 concentration,
- precipitation of dolomite → less than proportional increase in Mg^{2+}-concentration with depth,
- cation exchange → increase of Na/Cl-ratio.

Groundwater of the transition zone is explained by mixing of the top-type and the bottom-type groundwater.

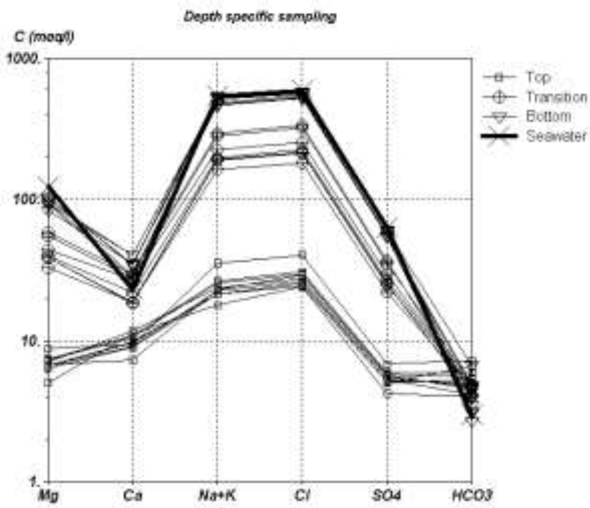

Figure 60. Schoeller-diagram of all samples.

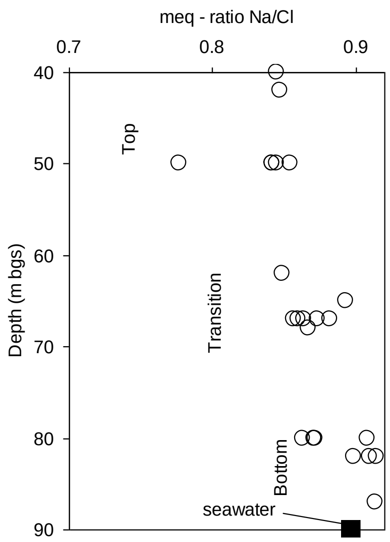

Figure 61. *Na/Cl-ratio with* depth of sampling.

Sampling during the upconing experiment
The pumping phase of the upconing experiment (16 – 28 April 2004) was accompanied by regular sampling the withdrawn water and measuring on-site the physico-chemical parameters temperature, electrical conductivity, and pH. The main purpose was to verify the degree of mixing between top and bottom-type groundwater, the latter entering the pumped well from deeper parts of the aquifer due to the upconing of the transition zone beneath the pumping well (MC6). Ideally, top-type groundwater should be withdrawn exclusively and the decline of the piezometric head should induce the upconing of the transition zone beneath and around the pumping well.

Data processing and evaluation
Generally, the concentrations of chloride as well as for other main cations and anions show little increase with time as a result of mixing with deeper groundwater. This indicates flow in upward direction and is explained by the partial penetration of the well.

Since the deeper groundwater has higher Na/Cl-ratios than the top-type groundwater, no additional process other than mixing is required to explain the change of Na/Cl-ratio over time. Given the accuracy of the analysis, the increase of this ratio by only 1.9% over the pumping time is at the detection limit and cannot be quantified further in order to evaluate the original depth of the added groundwater.

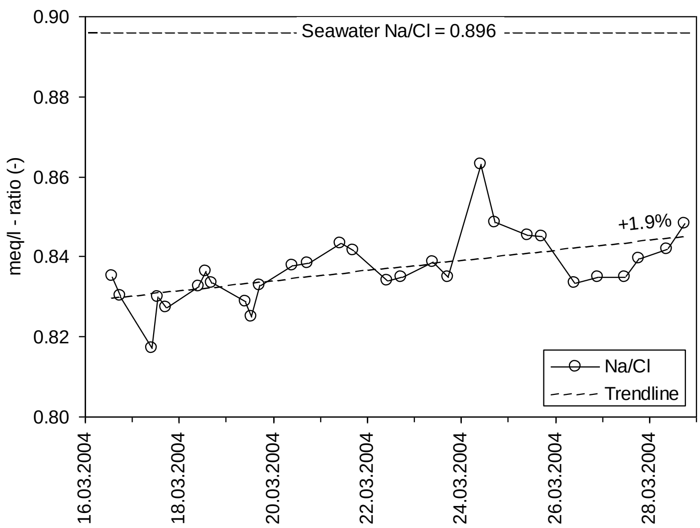

Figure 62. Time series of Cl-concentration during pumping.

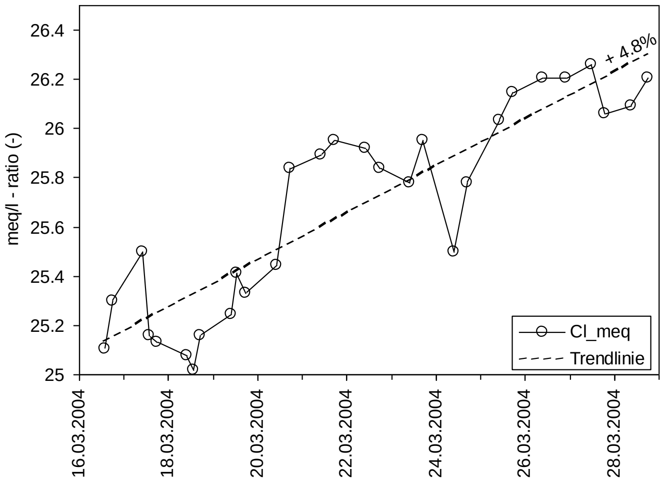

Figure 63. Time series of Na/Cl-ration during pumping.

The preliminary conclusions of the hydrogeochemical evaluation at Ses Sitjoles are:

- groundwater composition can be explained by mixing of two end members, i.e. the top-type groundwater with relatively low total dissolved solids, and the bottom-type groundwater with high total dissolved solids.
- additional processes other than mixing with seawater are required to generate the existing groundwater composition.
- the vertical permeability in the upper part of the aquifer is high enough to provoke significant flow when vertical hydraulic gradients apply.

Partner 2 (University of Birmingham - UK)

Positron Emission Projection Imaging (PEPI) of fractures

This work is conducted in collaboration with the Department of Physics at the University of Birmingham. Following delays in 2003 in obtaining the required radioactive isotopes, a series of tests on non-destructively estimating fracture apertures using Positron Emission Projection Imaging (PEPI) have been undertaken with a new set-up tested in 2003 (Figure 64). These tests are precursors to the proposed experiments on imaging the solutional widening of fractures in carbonate rocks due to the flow of acidic rainwater. Previous tests, using an old PEPI camera, were encouraging and provided good estimates of the thickness of thin layers of to liquid. The original camera has now been replaced by an updated version.

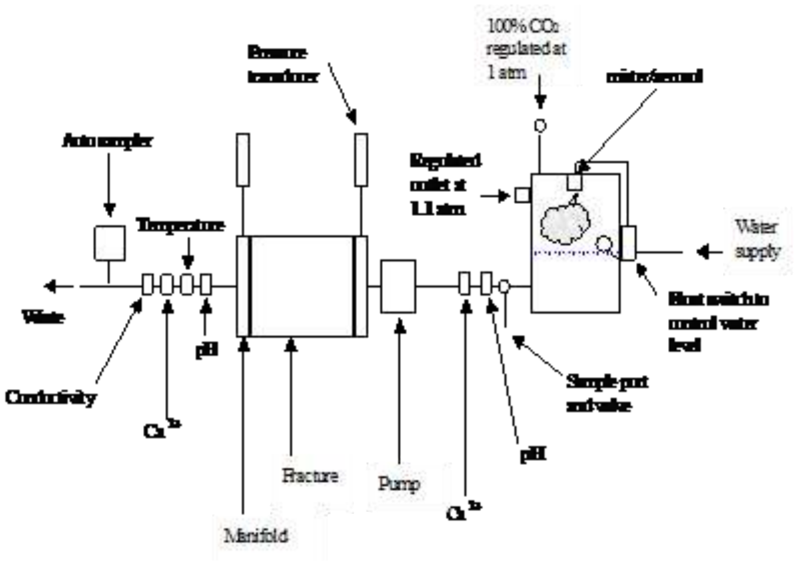

Figure 64. Schematic design of the PEPI experimental set-up.

To test the accuracy to which the new imaging system can measure fracture aperture, tests have been conducted on three artificial fractures. First, an artificial wedge-shaped fracture formed by two sheets of glass was imaged to test the ability of the system to measure slowly varying apertures. A test fracture, engineered in Perspex (Figure 65), was tested to assess the resolution of the technique in rapidly varying aperture fractures. Finally, the rock block containing a parallel-sided artificial fracture, which was to be used in the dissolution experiments, was tested to investigate the effect of the presence of carbonate rock.

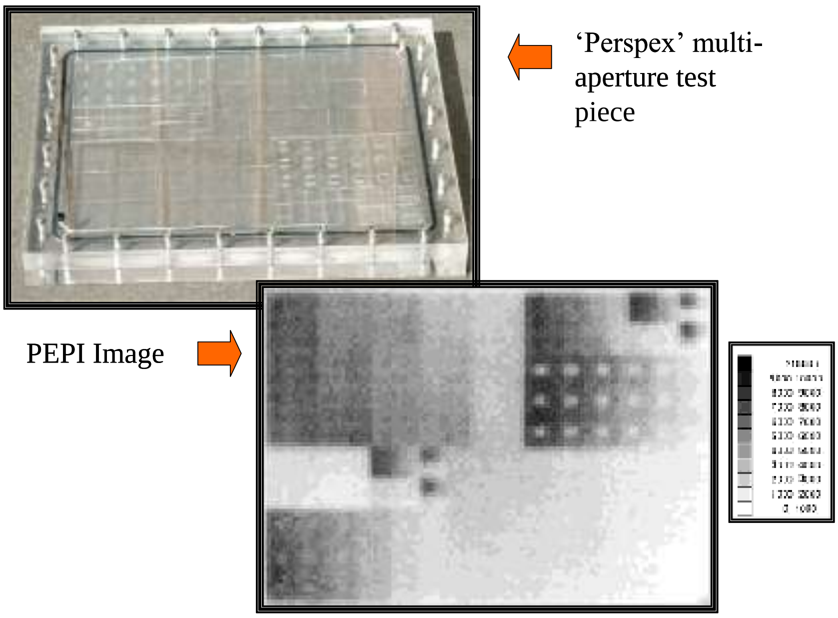

Figure 65. Artificial fracture made of "Perspex" and associated PEPI image.

The initial problems encountered at the end of 2003 have persisted through 2004. First, both the wedge and the rock block show clear non-uniformities (Figure 66). The wedge shows a circular feature in the aperture estimation and the rock block a clear ‘x’ shape on a uniform aperture fracture. All test pieces show overestimated fracture apertures. Refinement of the software developed to analyse the images reduced the overestimation problem in the glass wedge to around 10% of the true aperture and have improved the image non-uniformity, but the same technique applied to the rock block resulted in persistent errors of up to 150%. The large white areas in Figure 66 represent the inlet and outlet manifolds, which contain large quantities of radioactive tracer. Test with these areas shielded with lead to eliminate any scattering affects from them that might be producing the ‘x’ shaped feature were conducted with little improvement to the results. The preliminary conclusion is that, with the current apparatus, the PEPI technique is insufficiently accurate for the investigation into the dissolution of carbonate. In particular, the measurements are affected adversely by the presence of the rock itself. The experimental apparatus for the dissolution experiments has been constructed, as described in the 2003 progress report, and alternative techniques for estimating aperture are being investigated.

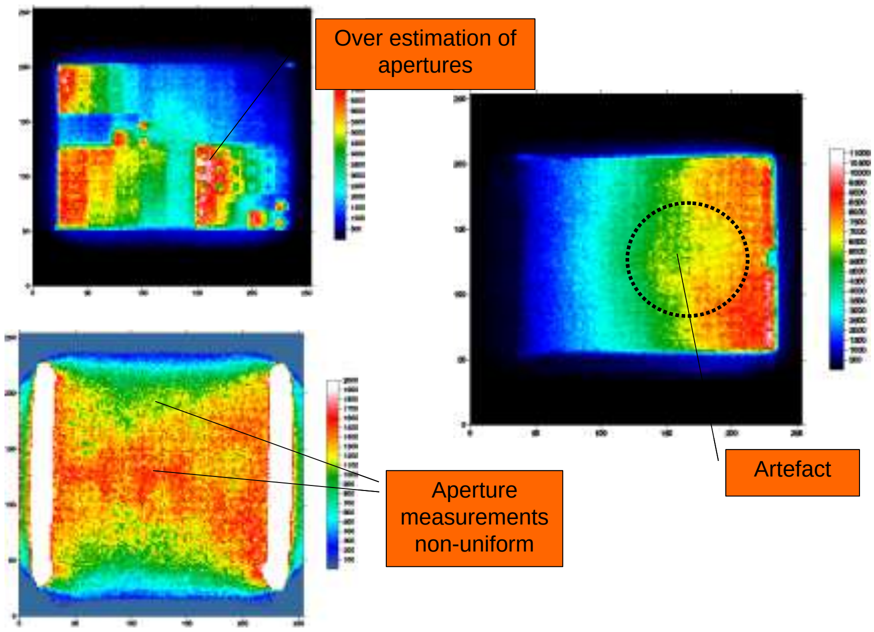

Figure 66. PEPI image of artificial test fracture.

Work package number: 5
New slimline and tools

Objectives and input to work package :

(a) Build and test 2 new hydrodynamical testing tools (H2E, CoFIS),
(b) Build and test 3 new slimline logging sensors (DopTV, SHyFT and MuSET),
(c) Design interpretation software adapted to saline wedge settings for these new tools.

Partner 1 (ISTEEM - France)

*Hydrological sources for downhole tests (**CoFIS** and **H2E**).*

The **CoFIS** (for « **Controled Fluid Injection Sonde** ») is designed to perform pressure and salinity controled fluid injection experiments. It is a multipurpose tool inspired from a fluorescent dye-tracing prototype developped by Participant 1 and designed for variable salinity fluid experiments in small diameter boreholes. It permits periodic injection or abstraction of fresh water and/or brine at chosen insulated levels in the well and flush in/flush out tracing experiments in order to scan fracture network dispersivity in the vicinity of the well, using water conductivity as a tracer.

CoFIS was designed and assembled in Montpellier, then deployed for the first time in the experimental boreholes of Lavalette (Figures 6 and 68) during a methodological experiment which included 6 tracer injections at variable flow rates, injection durations and tracer concentrations (Table 1).

Figure 67. Modified logging unit for CoFIS assembly and downhole deployment installed in LAV1 at Lavalette (Montpellier).


Figure 68. Surface pumping/injection unit with individual containers for tracer (yellow tank, to the right) and pushing fluid (blue tanks, to the left) for CoFIS experiments.

During the first set of experiments with CoFIS at Lavalette, the following protocole was followed for each of the 6 tracer injections:

1. set-up of a stationary flow regime while injecting fresh water (from Lav1) at a flow rate Q,
2. injection of the tracer during a time Δt,
3. injection of fresh water during a time T ('push' duration),
4. inversion of surface pumps to capture the tracer back into CoFIS.

Experiment	Q (l/min)	Δt (min)	T (min)	C_0 (ppm)
1	5	10	5	0.50
2	5	10	10	0.80
3	5	10	15	1.20
4	5	6.5	20	1.80
5	2.5	10	10	2.39
6	7	10	10	1.90

Table 2. Summary of CoFIS injection experiments at Lavalette (Q: injection flow rate; Δt: tracer injection duration; T: fresh water 'push' duration after tracer injection; C_0: initial concentration initiale of the tracer).

Comparing experiments 2, 5 and 6, with identical injection times and push durations, and with variable flow rates, the restitution curves remain nearly identical, which is coherent with numerical simulations. The amount of tracer recovered by CoFIS is on the order of 90 % for each experiment.

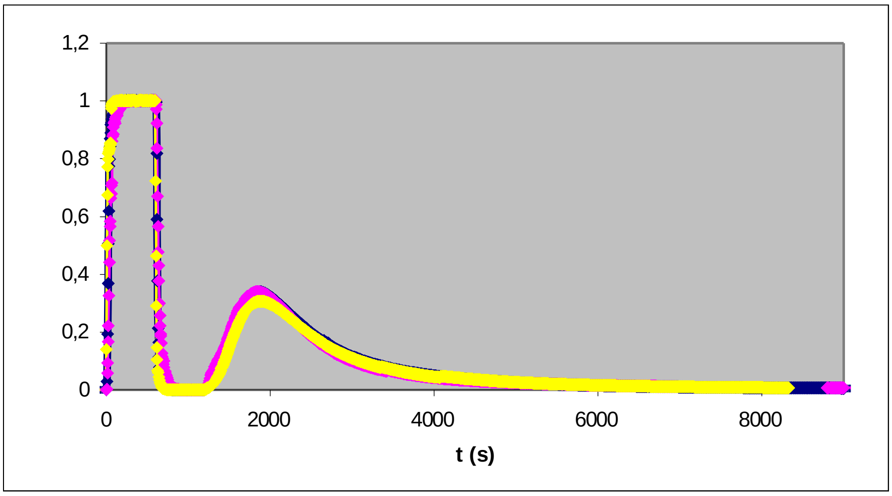

Figure 69. CoFIS restitution curves corresponding to experiments 2, 5 et 6.

Now comparing experiments 1 through 4, with identical flow rates (5 l/min), identical tracer injection duration (10 minutes) except for the 4th experiment (6.5 minutes) due to a power supply problem. The tracer concentration was increased from each experiment to the next to avoid data 'contamination' from previous experiments. The following results are presented in terms of of normalized concentration. The only variable parameter during these 4 experiments is consequently the 'push' duration, from 5 to 20 minutes. The results (Figure 82) are textbook examples for such experiments. CoFIS will be deployed at the EXS (Ploemeur) and SWS (Campos) during the ALIANCE extension, in 2005.

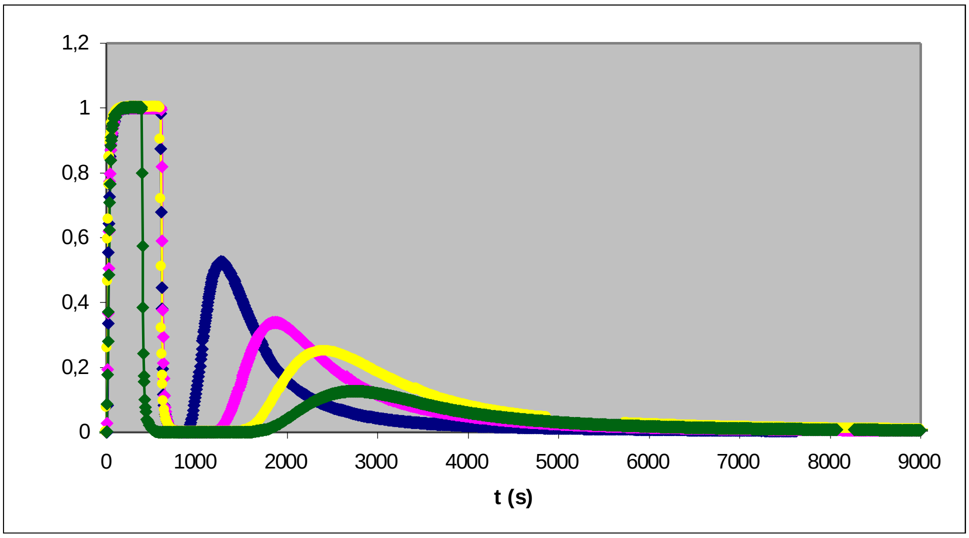

Figure 70. CoFIS restitution curves corresponding to experiments 1, 2, 3 et 4.

The H_2E testing tool, for « **Harmonic Hydraulic Endoscopy** » is designed for multi-directional scaning of the hydraulic transmissivity and fracture network connectivity using harmonic pressure perturbation. It is designed for paired-well experiments to achieve directional measurements. The experimental system comprises a stimulation probe set in the hole, a surface signal/control device and satellite pressure gauges set in nearby holes. This new design (**H_2E**) is derived from a single hole harmonic permeability probe developed for deep reservoir evaluation, with a down-sizing, inboarding of the harmonic pressure source to minimize signal damping, interfacing of **H_2E** with a standard logging platform. The tool will be completed and tested at the Montpellier experimental site (Lavalette) in 2005.

Geophysical receivers for downhole tests (DopTV, MuSET, ShyFT)

These 3 new tools are designed under the supervision of Partner 1, involving meetings and communications with Partners 5, 6 and 7.

Partner 6 (ALT - France)

Doppler acoustic imaging of flow at the borehole surface (DopTV).

DopTV is an extrapolated version of the FAC40 acoustic imager already used as part of ALIANCE. On the basis of laboratory experiments (see WP6), a new Doppler tool was built in 2004. It will be field tested in 2005.

Multi-sensors electrical tool (MuSET)

The aim of the **MuSET** tool (for « **Multiple Sensor Electrical Tool** ») is to measure the downhole spontaneous potential as a function of depth to evaluate a new method of monitoring of the long-terms variations of the fresh water/brine transitions in saline intruded aquifers. This method may be deployed either in natural situation or during active pumping tests. MuSET is an extrapolated version of the ALT Idronaut hydrochemical downhole tool. In 2004, the tool was completed and tested with sucess (Figure 71) at the Lavalette experimental site (ALIANCE, 2004). Most of the spontaneous potential originates from membrane potential associated with the presence of marly limestone in the LAV1 (Figure 72), as illustrated by the high natural gamma values recorded in the hole. MuSET will be deployed at the EXS (Ploemeur) and the SWS (Mallorca) during the ALIANCE extension, in 2005.

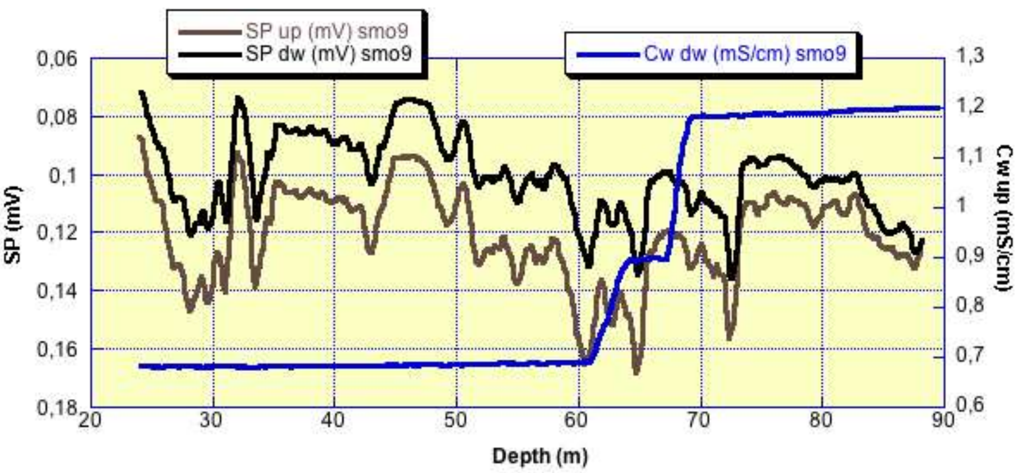

Figure 71. Up and down records of spontaneous potential obtained in LAV1 with MuSET, showing repreatability. The fluid conductivity profile in the hole is also presented (blue curve), showing zones of fluid inflow into the hole.

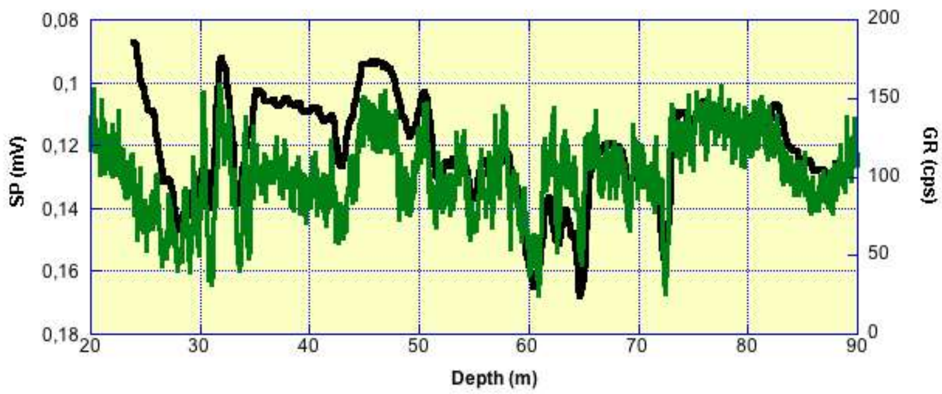

Figure 72. Spontaneous potential obtained in Lav1 with MuSET compared to a total natural gamma profile (green curve). The fit between the two curves indicates that membrane potentials associated with the presence of clay are responsible for most of the signal.

Partner 7 (Geo Energy - France)

Slimline Hydraulic Formation Tester (SHyFT)

The tool is a "RECEIVER" in the context of ALIANCE. This new tools could be used either independently or, in a more appropriate manner, in conjunction with the SOURCES for cross-hole aquifer investigation. It is conceived to provide a complementary description of key parameters; in summary, SHyFT will improve the capacities to:

- measure in-situ pore fluid pressure between packers or from a pad,
- sample fluids from discrete horizons in the aquifer,
- evaluate dm-scale permeability during testing and sampling.

For coastal environments, SHyFT is in particular designed to provide continuous fluid conductivity measurements during testing, and a controlled fluid sampling procedure. As in the oilfield device, individual measurements of permeability, pore pressure and in-situ fluid conductivity will be made, then repeated at different depths, as many times as required. Fluid samples will also be taken for later analysis in the laboratory.

After a design phase in 2002 and 2003, there has been no progress made in 2004 towards the build of SHyFT by Partner 7. This is explained by repetitive economical difficulties encountered by partner 7. This delay will be detrimental to the project in the testing phase of new instruments, in 2005, as precise in-situ sampling of fluid from the formation remains an important goal of ALIANCE. Traditional techniques of fluid sampling will be used instead, causing no arm or delay to the testing of other devices or methods.

Work package number: 6
Acoustics and signal processing

Objectives and input to work package :

(a) Determine the optimal signal processing method for the DopTV recording of flow rate images, using the borehole televiewer principle and Doppler-shift analyses,

(b) Identify the optimum functioning mode of the acoustic transmitter from prototype testing in a water tank simulating borehole conditions.).

Partner 5 (LMA - France)

In the first part of this report for WP6, the principle and the characteristics of the most widely used borehole flowmeters are reported. Theirs limitations are briefly discussed, after what part 2 provides a hydrodynamical characterization of the near-zone of round and plane jet exits with small flow rates. Recommendations for positioning of the sample volume is also discussed in terms of the relative size of the openings and of the inflow rates. Finally, part 3 describes the experiment designed at the Laboratory of Mechanics and Acoustics of CNRS in Marseille (LMA), to relate the acoustically measured velocities with the exact fluid velocity. Comparison and estimations of errors made on the horizontal inflow rates are reported.

Part 1 : Downhole logging sensors: flowmeters

1.1. Introduction

Borehole geophysics is the science of recording and analyzing measurements in boreholes or wells, for determining physical and chemical properties of soils and rocks. Borehole geophysical logging is a commonly used technique for the in situ characterization of aquifers. The measurement of flow within the borehole is one of the most useful well-logging methods to interpret the movement of groundwater and contaminants. Generally, geophysical logs provide information about the in situ physical and chemical properties in the vicinity of boreholes, which are only indirectly related to hydraulic parameters at a larger scale. Paillet, Crowder and Hess (1996) present a description of how the heat pulse flowmeter, in combination with acoustic borehole wall images, can be used to characterize the hydraulic properties of fracture systems intersecting a borehole. The flowmeter logs and acoustic-televiewer logs at these sites could enable the characterization of permeable fractures.

Yet, heterogeneous aquifers are difficult to describe using data obtained in a limited number of boreholes. Although the logs provide detailed information about subsurface flows, one can never expect to drill enough boreholes to characterize ground-water flow systems on the basis of borehole data alone. Besides, recent results indicate that the hydraulic conductivity of bedding planes and fractures cannot be inferred from the features of borehole image logs or from the apparent aperture of those features on caliper logs (Paillet, 1998). Although the full set of logs provides no information about how far the hydraulic features extend away from the borehole, the flow log does allow some analysis of the limited set of these features where flow actually occurs. This is an important step beyond simply identifying the fractures and the physico-chemical features of the solutions that intersect boreholes.

As stressed by Wilson & al. (2001) "*additional research is needed to determine how the borehole-flow measurements relate to flow in bedrock aquifers. The flowmeters may need to be evaluated under controlled laboratory conditions to determine which of the methods accurately measure ground-water velocities and flow directions. Additional research also is needed to investigate variations in flow direction with time, daily changes in velocity, velocity corrections for bedrock aquifers and unconsolidated aquifers, and directional differences in individual wells for hydraulically separated flow zones.*"

Thus, the purpose of this study is to provide a detailed description of simple flows flowing into the borehole. We consider simple round and plane jets, as an ideal source of water production in the ideal cylindrical borehole. Experiments are done in the case of the round jet, to known firstly whether one can extract velocity information from an operational Acoustic televiewer (ATV). The measured velocities will be compared with the real flow velocities, in order to propose a reliable algorithm of in-flow rate inversion from ATV measurements. This would be an interesting alternative to the Acoustic Doppler velocimeter (ADV) Son Tek prototype.

1.2. Borehole flowmeters

Borehole flowmeters data indicate where ground water is entering and exiting boreholes and can assist in interpretation of contaminant transport. Cross-borehole-flow logging tests can indicate the degree of connectivity of fractures beyond the well bore, and transient tests can be used to estimate hydraulic properties of fractured aquifers (Kearl and others, 1994). Flowmeters can be used to measure borehole flow under ambient as well as pumped conditions. Borehole-flow measurements made under ambient conditions can help to delineate transmissive fractures and other permeable zones and to indicate the direction of vertical hydraulic gradients; they also are useful in interpreting fluid-conductivity logs and borehole water-quality data. Borehole-flow measurements made under pumped conditions can be used to develop hydraulic-conductivity profiles of aquifers.

Hydraulic data for small-scale borehole features historically have been estimated from borehole-dilution and tracer tests and by use of spinner or impeller flowmeters. Spinner flowmeters have been used widely to measure vertical flow but are somewhat limited by relatively high stall speeds that range from 1 to 5 cm/s (Crowder and others, 1994). These stall speeds equate to flows of 300 to 1500 l/h in a 10-cm-diameter well. The spinner flowmeters can be stationary or can be trolled up and down the borehole. Conventional impeller flowmeters that are widely used in ground-water studies have a lower measurement limit of about 2 meters per minute, whereas the high-resolution flowmeters that use heat-pulse and electromagnetic methods can measure extremely low vertical flow rates in boreholes, namely having lower measurement limits of less than 0.03 meters per minute. Besides, conventional flowmeters provide no information about the velocity and direction of horizontal flow in the borehole.

In order to provide direct measurements of hydraulic quantities in the borehole, high-resolution flow logging equipment such as the heat-pulse (Hess, 1986) and electromagnetic (Molz and others, 1994) flowmeters were developed. Their primary application is to measure vertical flow within a single well, but measurements of lateral flow through a single well or flow between wells also may be recorded by borehole-geophysical methods. Recent studies have documented the development of high-resolution flowmeters like the hydrophysical logging, the horizontal heat-pulse flowmeter (KVA flowmeter), and the acoustic Doppler velocimeter (ADV).

1.2.1. Heat-Pulse and electromagnetic flowmeters

Heat-pulse technology allowed the development of a vertical flowmeter capable of measurements in the range of 0.2 to about 20.0 ft/min (i.e 0.102-10.16 cm/s), corresponding to discharges from about 0.01 to 1.5 gal/min (2.27 to 340,7 liter/hour) in a 6-inch-diameter borehole. The vertical heat-pulse flowmeter can measure velocity differences as small as 0.033 ft/min (0.017 cm/s). A pulse of heat is generated within ground water in the borehole, and temperature sensors (thermistors) positioned around the heat source monitor the heat (thermal) transmission through silica (glass) beads as affected by ground-water movement through them. The thermistors that measure the largest change in temperature after generation of the heat pulse are considered to be on or near the axis of the direction of groundwater flow. Thermistor machine-unit values correspond to ground-water-flow velocities and are related to the rate at which temperature changes are convected by ground-water flow across the thermistor array.

Additional flowmeters that use other properties of the physical system or other technologies have been proposed. Young and others (1991) and Molz and Young (1993) describe the development and application of an electromagnetic flowmeter with a minimum threshold velocity of about 0.3 ft/min and no theoretical upper measurement limit. The minimum threshold corresponds to a discharge of about 0.02 gal/min (4.54 liter/hour) in a 6-inch-diameter borehole when flow diverters are used to force all flow through the measurement section of the logging probe. Conventional vertical flowmeters have been used to estimate the vertical profile of permeability in the borehole and to infer the presence of hydraulic head gradients adjacent to the borehole (Paillet, 1998). This information has limited value, however, because it is recognized that the borehole facilitates vertical flow between aquifers and fractures that would not normally be present.

The horizontal heat-pulse flowmeter (KVA flowmeter), data collection, and calibration procedures are described by Kerfoot and others (1991). American Society for Testing and Materials (ASTM) methods has been documented for a KVA flowmeter (Kerfoot, 1995). Although a two-dimensional and three-dimensional heat-pulse flowmeter have been developed (Ker-foot, 1982), only the two-dimensional (horizontal) and one-dimensional (vertical) flowmeters are available commercially. The KVA flowmeter has a velocity-measuring range of 0.1 ft/d to 500 ft/d ($3.5.10^{-5}$-0.176 cm/s) in well screens, and 0.01 ft/d to 500 ft/d ($3.5.10^{-6}$-0.176 cm/s) if placed in native soil without screen resistance. The capability of the flowmeter to measure horizontal ground-water-flow direction and velocity representative of aquifer conditions relies on the hydraulic connection between the fuzzy packer and the surrounding media. If hydraulic short-circuiting occurs across the packer and surrounding formation, localized channeling may occur and resulting streamlines may interfere with obtaining a representative measurement. The KVA flowmeter does not compensate for borehole inclination, which may be a factor with deep wells that deviate from vertical with depth. In uncased wells, the maximum operating depth may be limited by the texture of the borehole wall. Because the fuzzy packer fits against the borehole wall, irregularities on the borehole wall may catch the fuzzy packer and prevent it from passing.

Heat-pulse and electromagnetic flowmeters are calibrated routinely in units of borehole discharge through the measurement section of the probe. Both measurements are made with flow diverters used to block leakage of flow in the annulus between the probe and borehole wall. Flow diversion is 100-percent effective in smooth-walled calibration tubes where probe response is calibrated in flow units. Rough-walled boreholes may allow some leakage, and calibrated flow measurements may need to be multiplied by a leakage factor. This factor usually is established in the field by comparing calibrated flowmeter response to known flow rate immediately below the pump during aquifer tests.

1.2.2. Hydrophysical logging

Hydrophysical logging also has been referred to as fluid-conductivity logging and fluid-electrical-conductivity logging. Hydrophysical logging is a method of estimating the magnitude of flow on the basis of flow-induced changes of fluid conductivity in the borehole.

Tsang and others (1990) describe the theoretical development of equations used to calculate inflow velocities and the numerical analysis of the borehole data. Assumptions and limitations of the calculations also are described in Tsang and others (1990). Hydrophysical logging involves replacing the borehole fluid with deionized water, followed by a series of temperature and fluid-electrical-conductivity (FEC) logs that profile the borehole to determine where formation water is entering and leaving (Tsang and others, 1990). A time series of FEC logs can identify the locations and rates of inflow and outflow. Loew and others (1991) modified the numerical equations proposed by Tsang and others (1990) to include solutions for multiple interfering fractures and time-varying inflow salinities and discharges.
Hydrophysical logging can provide measurements of horizontal velocity, but not of direction, as well as vertical flow velocity. Because hydrophysical logging produces continuous profiles of the fluid conductivity, a major benefit of the technique is its usefulness in identifying and quantifying flow zones in deep, uncased wells or in wells with long screened intervals.

In fact, hydrophysical logging provides estimates of the ground-water velocity in the borehole over a range of depth rather than at a discrete point, as with the other flowmeter methods, since it provides flow measurements estimated from measured changes in fluid-electrical conductivity along a length of borehole. Rather it provides an average volumetric velocity V based on the relation $Q = VA$, where Q is the measured volumetric inflow rate and A is the cross-sectional area of the borehole (A = diameter borehole x sampling vertical length). This method should be reliable for porous and weakly permeable aquifers, for which the volumetric inflow rates are in the range 0.001-0.04 gal/min (0.23-9.08 liter/hour) in a typical borehole with diameter of about 6 inch (15.24 cm).

1.2.3. Acoustic Doppler velocimeter

Conventional tools for measuring flow within a borehole include the impeller flowmeter, heat-pulse flowmeter, colloidal boroscope, and hydrophysical logging. Most of these tools are limited in their dynamic range and cannot simultaneously measure lateral and vertical flows through the borehole. The development of the borehole acoustic Doppler velocimeter (B-ADV) allows direct three-dimensional (3-D) measurements of borehole flow across a range of velocities from 0.0003 to 8 ft/s. The B-ADV was first successfully applied to a coastal monitoring well completed in an alluvial aquifer in 1996 (Ursic, 1996). Since then, modifications have improved the accuracy of depth placement in the borehole and the stability of the B-ADV during data acquisition. More recently, the B-ADV has proven to be a valuable geophysical tool for measuring flow in coastal aquifers in California (Newhouse and Hanson, 2000) and carbonate aquifers in Indiana and Tennessee (Wilson and others, 2001). Because the ADV was recently developed, its application has limited documentation. The technical specifications and applications of the ADV have been introduced by Kraus and others (1994) for surface-water measurements.

The acoustic Doppler velocimeter (ADV) for borehole research was developed for the U.S. Environmental Protection Agency by SonTek Inc (1996). The borehole ADV is a prototype based on the ADV SonTek manufactures for making three-dimensional measurements of flow for oceanic and surface-water applications. The ADV is approximately 4 ft long with a 3-inch outer diameter. The probe tip consists of one centrally mounted acoustic emitter and three receivers/transducers positioned on radial arms. The sample volume of the ADV is roughly cylindrical in shape. Volume is a function of the diameter of the transmit transducer (0.177 inch / 2.697 cm) and user-defined parameters of transmitter-pulse length and receiver-window length that are adjusted with the acquisition software. The focal point of the sample volume is about 1.9 inches in front of (below) the emitter, and the sample volume ranges from 0.008 to 0.028 cubic inches (or 131 to 459 mm^3). The frequency of measurement is 25 times per second, resulting in a large particle-tracking database that includes X, Y, and Z directions (corresponding to east, north, and up in the borehole coordinate system); pitch from vertical; signal-to-noise ratio; and a correlation factor.

The ADV does not measure fluid velocity directly but tracks the velocity of suspended particles in the water column. Real-time graphic and tabular displays by the data-acquisition software allow the user to monitor the measured velocities, data quality, and the stability of the sampling environment. Borehole flow can be measured accurately as low as 25.9 ft/d (0.0003 ft/s = 0.009 cm/s), using centralizers, and to 86.4 ft/d (0.001 ft/s = 0.030 cm/s) without centralizers. The upper limit of velocity measurement is about 691,000 ft/d (8 ft/s=243 cm/s). Operation of the ADV depends on user-specified velocity limits over which the system searches for the velocity signal. The closer the specified limits are to the true velocity field, the more accurate the measurement of velocity of the tracked particles in the flow field.

1.3. Inter-comparison studies

In summary, the "minimum velocity" resolution of the method ranges from stagnant or zero flow, up to 25.9 ft/d. The KVA flowmeter can measure velocities from 0.1 to 500 ft/d when used with the fuzzy packer. The KVA flowmeter also can measure zero-flow conditions indirectly by recording data that are indeterminate for direction. When a flow vector cannot be resolved, it is usually because velocities are near zero. The ADV has the highest minimum velocity resolution at 25.9 ft/d and the highest upper limit at 691,200 ft/d (8 ft/s). The colloidal borescope can detect stagnant or zero-flow conditions if colloids are visible. The upper limit of velocity measurement with the colloidal borescope, theoretically, is about 7,085 ft/d. The hydrophysical logging can determine velocities down to about 0.01 ft/d, and it can determine a maximum flow rate of about 1,000 gal/min.

Usually, vertical flow is common in most wells that are open to more than one aquifer and flow can be induced by either pumping or injecting water. The effect of the vertical flows can be important for large flow rates in the borehole. It depends on the type of aquifers (composition, fractures, etc...), and on either natural or pumping-induced vertical hydraulic heads supported by the borehole. Usually these vertical flows are not difficult to measure for low flow rates. The nature of the aquifer heterogeneities also can affect the ground-water-flow measurement. Flowmeter measurements are particularly sensitive to flowmeter positioning relative to the preferential flowzone. Steeply inclined fractures also may produce results that are difficult to interpret because of non-horizontal flow across the borehole.

The time required to record a measurement with each tool varies. The time required for a measurement with any of the flow logging tools also varies with the flow conditions in the well; higher ground-water velocities can allow for quicker measurements. The KVA flowmeter typically requires about 30 to 45 minutes for each measurement. Lower velocities require more time for the heat pulse to dissipate in the vicinity of the thermistors. The ADV typically requires about 10 to 15 minutes for each measurement. The time required for measurements with the colloidal borescope ranges from about 15 minutes to 2 hours, depending on the flow conditions at the test interval. The hydrophysical logging requires about 1 day for each test at a given well. As with the point-measurement methods, the time required for hydrophysical logging probably would decrease with higher ground-water velocities.

Also, the interpretation of flow measurements can be complicated by flow regimes changing with time as measurements are being made. It is sometimes difficult to determine if a change in measured flow represents a difference in flow over the thickness of the aquifer or just a change in flow field with time (Paillet and others, 1994). The presence of the flowmeter in the borehole may produce eddies in vertically moving ground water that can affect measurements; in some cases, measured flow directions have indicated a vertical hydraulic head known to be incorrect (Kearl and others, 1994; Paillet and others, 1994). Tool insertion can cause a pressure-pulse effect from fluid displacement by the tool that, in turn, affects flow measurements (Kerfoot, 1988). Indeed, repeated measurements in the same borehole but at different times reveal that none of the tools could consistently provide repeatable measurements of velocity and direction (if available). In some instances, the original and repeat measurements were made on different days; this could explain some of the variability because hydraulic conditions could change over a 12- to 24-hour period. The ability to measure horizontal flow independently from vertical flow is a unique and important feature of the B-ADV. Horizontal flows can reveal the direction and speed of migrating contamination plumes, and vertical flows can reveal possible cross contamination between different aquifer systems penetrated by a well bore.

1.4. Concept of DopTV flowmeter: past studies

The concept of DopTV tool for "Doppler Televiewer" corresponds to the development of a Doppler-based analysis protocol, as part of the existing BoreHole TeleViewer technology (BHTV) using ultrasonic pulses to image with high resolution fractures intersecting a borehole. The objective of this tool is to provide information on the distributions of fluid velocities through millimeters fractures, in order to estimate horizontal inflow and outflow rate while scanning vertically the borehole wall. The principle of the DopTV tool relies on the analysis of the so-called Doppler effect on backscattered ultrasonic pulses from fine moving particles in the borehole fluid.

This concept has been successfully tested using a laboratory experimental model (Saito and Niitsuma, 2001). These studies have also demonstrated the need for a comprehensive signal processing study, in order to identify the most appropriate method to detect and measure fluid velocities near the borehole wall. During the first year of the ALIANCE project, the LMA has developed laboratory experimental and numerical models associated with signal processing tools to study the performance of various algorithms of velocity estimation.

This study has addressed narrow-band and wide-band velocity estimators, using both experimental and numerical tests (Monnier et al (a), 2003). The conventional autocorrelation method (ACM), also called the "pulse-pair" method, was selected among the considered narrowband velocity estimators, since it allows "relatively" accurate measurements of the mean flow velocity using a reduced number of samples. It was also demonstrated that other narrow-band velocity estimators, based on extraction algorithms of the mean frequency shift that is proportional to the mean velocity within the sample volume, were less accurate than the ACM method. It is important to notice that in this report, we use the expression "mean frequency shift" rather than "mean Doppler frequency" to differentiate between the interaction between the moving scatterers and the pulse, yielding the well-known "mean Doppler frequency", and the inter-pulse movement of the scatterers. The latter is usually the effect detected in pulsed wave ultrasound systems.

Wide-band velocity estimators were also studied in this study, although the performance were not compared with that of the considered narrow-band velocity estimators. Wide-band velocity estimators measure the time shift between successive range-gated backscattered RF echoes. This time shift, which is proportional to the mean velocity of the targets passing through the sample volume, can be estimated using either an "active" or "passive" cross-correlation technique. Monnier et al, 2003 (a) have tested different "passive" cross-correlation techniques, whereby one cross-correlates successive pairs of range-gated echo data to determine the time lag of the peak value of the resultant cross-correlation function. This time lag is proportional to the mean velocity contained within the sample volume. This technique is known as the cross-correlation method (CCM). It is well known that this technique is computationally expensive, and that a about 50 pulses are required to ensure convergence of the different velocity estimators under the flow rate conditions considered in Monnier et al, 2003 (b).

During the second year of the ALIANCE project, experiments at LMA were carried out in a water tank with the ultrasonic probe installed on the ATL-ABI 40 borehole televiewer to testing the possibility of using the above-mentioned velocity estimators. First measurements revealed that with the ABI 40 probe, no useful signals could be detected when the cross-borehole inflow rate is too low, like in borehole conditions. Further experiments with different ultrasonic probes have confirmed the possibility to make "Doppler-shift" measurements at low flow rate (Guillermin and Sessarego, 2004). This study has suggested that not enough reflected energy can be received with the actual design of the ultrasonic ABI 40 probe below mean velocity of few cm/s. This was explained as interference might occur between parasitic signals and the Doppler signals. It was therefore suggested to consider either further signal processing techniques to separate the parasitic signals from the Doppler signals, or the possibility to re-design the ABI-40 borehole televiewer.

Although these studies (Guillermin and Sessarego, 2004; Monnier et al, 2003a,b) have provided useful information to identify the most appropriate signal processing methods for velocity estimations in borehole conditions, few expected characteristics of the velocity estimations were not observable as the decrease of the measured flow velocities with the distance from the borehole wall. Besides, it was reported that there were large fluctuations of the estimations for the same experimental conditions, and this was explained as large fluctuations of the actual flow rate emitted from the round-shaped modeled fracture. Any quantitative study on the reproducibility of the experiments has been carried out, and this fact motivates the study of this report.

The present work is concerned with the study of the relationship between the estimated measured velocities and the actual fluid velocities. The measured velocities are determined from the characteristics of the backscattered waves from fine particles, which follow the fluid motions. Thus, the knowledge of the characteristics of the fluid motion is of primary importance, as well as the choice of the model for the received signals in such pulsed Doppler systems.

Part 2 : Physical modeling of borehole flow from an idealized fracture to evaluate fluid velocities

2.1. Introduction

With conventional pulsed wave ultrasound systems, velocity information is extracted from the reconstructed Doppler signal, which results from scatterers crossing the ultrasound beam. The Doppler signal is reconstructed by using samples from a number of pulse RF echo lines. A region of interest is selected, and the received signal is range gated to infer the spatial distribution of velocity after processing data.

Usually, the performances of such pulsed Doppler systems depend on the adopted estimation strategy which, in turn, is limited by the assumptions used to define a backscattered signature model. The model for the scattering medium requires specific statistical assumptions in order to describe random variation in the returned signal over the region of interest. The best physical model should account for transducer geometry, scattering process by the particles, attenuation due to geometrical effects, fluctuations of the concentrations of particles and non-uniform velocity distributions within the sample volume.

Of particular interest is the relation between the movement of the particles and the statistical properties of the estimates of the fluid velocity within the sample volume. In most studies, mainly in medical sciences, the flow are usually considered as uniform and stationary within the sample volume, in order to define a signature model which is used to develop velocity

estimation techniques. When these conditions do not occur in the flow, the performances of the estimators usually degrade. The variance of the estimates subsequently increases dramatically. Actually, this drop of performance can occur, either because the underlying physical model is not corresponding to what happens in the sample volume or because of the decrease of the signal-to-noise ratio of the received signal.
The objective of this work is to study the flow configuration studied in the water tank at LMA, in order to correlate mean velocity estimates with pulsed Doppler system and "true" fluid velocities in the flow. It is important to stress that this work is not concerned with a study of signal processing techniques, but rather with the physical understanding of the experimental measurements. The first part of this chapter will, nevertheless, provide a physical model to account for a general distribution of scatterers in the sample volume. This might provide a starting point on sound physical basis for further studies and development of signal processing techniques. In the second part, this report will focus on the existing knowledge of the characteristics of plane and round jets, which have been chosen as idealized fractures at the borehole wall. Finally in the last part, the possibility to use jointly a model of mean velocity profile for jet flows and measurements from the pulsed Doppler system, will be considered in order to infer the borehole inflow rate.

2. Signal model and velocity estimation

As far as the velocity estimation is concerned, an estimator should ideally combine high precision so that random fluctuations do not interfere with the perception of the true flow patterns, high spatial and temporal resolution to enable detection of spatially localized and transient flow events, and reasonable computational complexity which is critical owing to the requirements for real-time data processing.
In order to develop any estimation strategy for the fluid velocity, a model for the returned signal is required. This model should describe the received signal from a group of scatterers passing trough the ultrasound beam, for a transmitted signal that consists of a periodic series of short pulses. With a model of received signals, an estimation method is used to determine the characteristic parameters of the returned signals from which the velocities are inferred. In particular, the correlation function plays an important role in the estimation of fluid velocity parameters. Most velocity estimators are based on the correlation function. Indeed, this is because the total backscattered signal can be modeled as a correlated Gaussian random process and is therefore completely specified by its mean and its autocovariance.

2.1. Signal model

In order to evaluate the mean and autocovariance of the random process, we must make some assumptions on the statistical models. To justify the Gaussian assumption, the received signal is modeled as a sum of independent signal components from a large number of point-scatterers, each contributing a slightly modified replica of the transmitted pulse, with a delay according to the distance from the transducer.
The signal model presented here is based on a random continuum model for the scattering from blood (Angelsen, 1980) for general velocity distribution in the sample volume. The small-scale spatial fluctuations in mass density and compressibility which determine the incoherent part of the scattering, are assumed to be proportional to the spatial fluctuations in the scatterers concentration $n_{sc}(\mathbf{r},t)$, where r is the spatial position and t is time. The particles concentration $n_{sc}(\mathbf{r},t)$ is therefore considered as a random process in space and time.

$$n_{sc}(\mathbf{r},t) = n_0(\mathbf{r},t) + n(\mathbf{r},t) \quad (2.1)$$

where $n_0 = \langle n_{sc}(\mathbf{r},t) \rangle$ is the local ensemble average of the scatterers concentration, and n is the local fluctuation of n_{sc} around its mean.

In fact, the statistical characteristics of the received signal are related to the fluid velocity field. When the correlation lengths of the fluctuations are much smaller than the dimensions of the resolution cell through which they are observed, i.e the Doppler sample volume for a fixed time t, the autocorrelation function for the concentration can be approximated as, neglecting diffusion,

$$\left\langle n(\mathbf{r},t)\, n\left(\mathbf{r}+\vec{\xi}, t+\tau\right)\right\rangle = \Upsilon(\mathbf{r},t)\cdot \delta\left(\vec{\xi} - \vec{\zeta}(\mathbf{r},t,\tau)\right) \tag{2.2}$$

where $\vec{\zeta}(\mathbf{r},t,\tau)$ is the displacement of the fluid element at position $\mathbf{r}$ during the time interval t to $t+\tau$. The variance per unit volume in the number of particles,

$$\Upsilon(\mathbf{r},t) = < n^2(\mathbf{r},t) >, \tag{2.3}$$

is assumed to be proportional to the backscattering coefficient from the scattering region of interest. For stationary velocity fields, the function $\Upsilon(\mathbf{r},t)$ as well as the displacement function $\vec{\zeta}(\mathbf{r},t,\tau)$ will be independent of time t. In this case, the process $n_{sc}(\mathbf{r},t)$ is stationary in time. If in addition the velocity field is uniform, and the quantity Υ is constant in space, the process $n_{sc}(\mathbf{r},t)$ will be stationary in both space and time.

Let z be the distance between the transducer and the center of the sample volume along the beam axis. The range gate $t = 2z/c$ corresponds to the round-trip time for the echo between pulse emission and reception. To obtain the total signal from this depth location, the point scatterer response $e(\mathbf{r},t)$ is multiplied with the scatterers concentration at the time when the transmitted pulse arrives at the point $\mathbf{r}$, and the product is integrated over the entire region of non zero integrand,

$$g(t) = \int e(\mathbf{r},t)\, n_{sc}\left(\mathbf{r}, t-\frac{r}{c}\right) d^3r \approx \int e(\mathbf{r},t)\, n_{sc}\left(\mathbf{r}, \frac{t}{2}\right) d^3r. \tag{2.4}$$

The last approximation results because, when the sound speed c is much larger than the fluid velocity, it is reasonable to neglect the displacement of the scatterers during the short time when the pulse transverses the sample volume. Here $r = |\mathbf{r}|$ is the distance from the origin, which is in the center of the transducer, and $r = z$ on the beam axis.

The signal waveform as well as the amplitude of the point scatterer response are influenced both by the aperture geometry, and scattering characteristics of the insonified medium. Both the waveform and the amplitude $e(\mathbf{r},t)$ will vary with spatial position of the scatterer. In a region near the beam axis and the focal point, the received waveform will be a close to a replica of the transmitted waveform, whereas in the side lobes of the beam, the received waveform will have a longer, and more irregular shape. The spatial variation of the point scatterer response amplitude depends to some extent on the transmitted pulse waveform. For continuous wave excitation, the beam profile in the far field has a form close to a sinc function with one main lobe and periodical side lobes. For the short pulse excitation, the main lobe has almost the same shape , while the side lobes are smeared out.

For N_p coherent pulse transmissions, the received signal obtained from a sample volume containing N_T identical point scatterers in the far field of the transducer, can be expressed

$$g(t) = \mathrm{Re}\left\{\sum_{k=0}^{N_p-1}\sum_{i=1}^{N_T} D\left(\mathbf{R}_{i,k}\right) \tilde{s}\left(t - kT_R - \tau_{i,k}\right) e^{i(\omega_0+\omega_{d})(t-\tau_{i,k})}\right\} \tag{2.5}$$

which assumes that the net component of the motion is toward the transducer. In (2.5), k is the transmit burst number, $\tilde{s}(t)$ represents the pulse's complex envelope following convolution with the impulse response of the system and scatterer, ω_0 is the mode angular frequency of the received pulse, T_R is the pulse repetition frequency (PRF), and $D(\mathbf{R}_{i,k})$ is the transducer two-way directivity function for the *i*th scatterer whose vector position is $\mathbf{R}_{i,k}$. Also the angular Doppler shift frequency of the *i*th scatterer moving with a velocity vector $\mathbf{v}_i$ is given by:

$$\omega_{i,d} = \frac{2v_i\omega_0\cos\theta_i}{c} \tag{2.6}$$

where θ_i is the angle between the velocity vector and the beam axis, and $v_i = |\mathbf{v}_i|$. This model is valid for a very general fluid flow. Here, we will assume that all the particles follow the mean motion of the flow whose direction is aligned with the beam axis direction. Thus, for all scatterers $\theta_i = 0$. The time shift

$$\tau_{i,k} \approx \frac{2}{c}\left(R_{i,0} - v_i kT_R\right) \quad for \quad k = 0,1,\dots,N_P - 1 \tag{2.7}$$

represents the two-way propagation time of the *k*th reflected pulse from the *i*th moving scatterer initially located at position $R_{i,0}$ within the sample volume.

For a large number of scatterers that are uniformly distributed with respect to their initial positions in the sample volume, the central limit theorem states that the summation over N_T scatterers in (5) will have a signal signature of a Gaussian distributed amplitude. Hence (5) can be expressed as:

$$g(t) = \mathrm{Re}\left\{\tilde{g}(t)e^{i\omega_0 t}\right\} \tag{2.8}$$

where

$$\tilde{g}(t) = e^{i\omega_d^m t}\sum_{k=0}^{N_P-1}\tilde{r}\left(t - kT_R - \tau_k^m\right) \tag{2.9}$$

in which ω_d^m is the mean angular Doppler shift frequency, $\tilde{r}(t)$ is a complex bivariate Gaussian process, and τ_k^m is the mean time shift of the complex envelope following the *k*th transmit burst. The real and imaginary part of $\tilde{g}(t)$ correspond to the in-phase and quadrature components of the baseband signal. Velocity information can be obtained, either from the Doppler shift frequency or from a time shift corresponding to the changing scatterer position within a sample volume between successive bursts. The resultant estimate should be proportional to some average velocity contained within the sample volume. The size and the shape of the sample volume are determined by the length of the transmit pulses, as well as the shape of the ultrasound beam that is characterized by the lateral beamwidth and length of the focal zone (axial depth-to-focus) of the transducer.

2.2. Narrow-band velocity estimation

In general, narrow-band processing of the backscattered signal $g(t)$ requires the assumption that the mean time shift τ_k^m is small compared to the decorrelation time of the entire Gaussian distributed backscattered signal. As such, the time shift corresponding to the changing scatterer position is ignored. Only the phase associated with the Doppler shift frequency component is used to obtain a velocity estimate with the following relation,

$$v_m = \frac{c}{2}\frac{\omega_d^m}{\omega_0}. \tag{2.10}$$

Narrow-band estimation is characterized by the use of a fixed range gate, such that the phase quadrature demodulated complex envelope is sampled every T_R seconds. In a single-gate pulsed system, this yields the discrete complex Doppler signal available for the analysis,

$$g(kT_R) = e^{i\omega_d^m kT_R} \cdot f(k\beta T_R) \quad for \quad k = 0,1,\ldots,N_p - 1 \tag{2.11}$$

where

$$\beta = \frac{2v_m}{c} \tag{2.12}$$

is stretched time factor.

To obtain velocity information from this complex Doppler signal, the moment of the Doppler spectral density function must be estimated. Specifically, the Doppler spectrum mean frequency, $\bar{\omega} = \omega_d^m$, can be estimated from

$$\bar{\omega} = \frac{\int_{-\infty}^{\infty} \omega P_{\tilde{g}}(\omega)\, d\omega}{\int_{-\infty}^{\infty} P_{\tilde{g}}(\omega)\, d\omega} = \frac{\dot{R}_{\tilde{g}}(0)}{i\, R_{g}(0)} \tag{2.13}$$

in which, $P_{\tilde{g}}(\omega)$ is the power spectral density of the noise free complex Doppler signal given in (2.11), and $R_{\tilde{g}}(\tau)$ is the complex autocorrelation function which can be obtained from $P_{\tilde{g}}(\omega)$ using the Wiener-Khintchine theorem,

$$R_g(\tau) = \frac{1}{2\pi}\int_{-\infty}^{\infty} P_g(\omega)\, e^{i\tau\omega}\, d\omega. \tag{2.14}$$

The angular "variance" of the Doppler spectral density is a measure of spectral spread. It is defined as

$$\sigma_{\varpi}^2 = \frac{\int_{-\infty}^{\infty} (\omega - \bar{\omega})^2 P_g(\omega)\, d\omega}{\int_{-\infty}^{\infty} P_{\tilde{g}}(\omega)\, d\omega}, \tag{2.15}$$

and is often referred as the mean-square bandwidth of the Doppler spectral density. Two distinct velocity estimation methods can be distinguished. The frequency-domain approach considers estimate of the Doppler spectral density $P_g(\omega)$, while the time-domain approach involves estimate of the autocorrelation function $R_g(\tau)$.

Among the different narrow-band velocity estimators that have been reviewed by Monnier et al., 2003 (b), the pulse pair method has always the lowest estimation variance, even when the bandwidth of the received signal is broad. Using the approximation $R_g(\tau) = |R_g(\tau)|\, e^{i\Phi(\tau)}$ in (2.13), the pulse pair method is based on the following approximation

$$\bar{\omega} \approx \frac{\Phi(T_R)}{T_R} = \frac{1}{T_R}\tan^{-1}\left[\frac{ImR_g(T_R)}{ReR_g(T_R)}\right] \tag{2.16}$$

However, its estimation variance increases greatly when the bandwidth of the received signal is wide. On the other hand, reducing the bandwidth of the emitted signal limits the range resolution, so there is a trade-off between velocity estimation variance and range resolution.

2.3. Wideband velocity estimation

Wideband velocity estimation methods measure the time shift between successive range-gated

backscattered echoes. the time shift, which is proportional to the mean target velocity, can be estimated using either an active or passive cross-correlation technique.
Active time shift estimation is accomplished by using a tracking range gate and cross-correlating the RF echo data with some a priori model of the data. Such an approach was a first applied to blood velocity estimation by Ferrara and Algazi, 1991(b), and is referred as the wideband point maximum likelihood estimator. For further details, the reader is referred to Ferrara and Algazi, 1991(a).
Alternatively, one can use a passive time shift estimator, whereby one cross-correlates successive pairs of range-gated echo data to obtain an estimate of a classical cross-correlation function. The lag that corresponds to the peak of the resultant cross-correlation functions is proportional to the mean velocity contained within the sample volume. The mean time shift τ_k following the kth transmit burst can be related to the mean velocity estimate by

$$v_m = \frac{c}{2}\frac{\tau_k^m}{T_R}. \quad (2.17$$

This technique, known as the time-domain cross-correlation method is superior to the narrowband techniques in some aspects. A detailed study of this technique for blood velocity estimate has been done by Jenssen (1993). It was shown that due to the nonlinear character of these estimators, based on peak detection algorithm of the cross-correlation functions, small perturbation of the cross-correlation function can lead to detection of a wrong peak and, thus, a wrong velocity. The deviation depends on the amount of data available, on the bandwidth of the transducer and on the signal-to-noise ratio. All these factors will introduce a variance on the position of the peak location. Another problem with this method, compared to the pulse pair method, is the difficult task of making real-time implementation because of the tremendous amount of calculations. For further details, the reader is referred to Jenssen (1993, 1994).
This approach has been studied at LMA, and estimations using the cross-correlation function were obtained for various flow rates (Monnier et al. (b), 2003). Although the effect of ensemble length (number of pulses) on the convergence of the estimation was examined, those of the range gate length and of flow regime were not investigated. The present study will analyze the series of data collected at LMA (see chapter 3), in order to provide supplementary information on the relation between the estimations and the "true" velocities.

3. Analysis of three-dimensional jet flows

In this part, we briefly review the knowledge of three-dimensional jet with low Reynolds number. We will see that description of the flow near the exit is a very difficult problem. The near zone of such jets is influenced by the existence of naturally unstable modes of the shear-layers surrounding the core jet. Generally the modes are excited near the exit and grow while propagating downstream. As we shall see it is important to know the relative importance of these modes in function of the position in the jet and of the Reynolds number. Indeed they determine the characteristic of the jets and of the associated large-scale vortices. This may under certain circumstances affect the performance of flowmeter systems, which are usually calibrated on a basis of simple flow configuration.
There have been numerous experimental studies on free jets, since the pioneering work of Reynolds (1962) [?] who observed experimentally the characteristics of laminar axisymmetric jet by varying the Reynolds number of the jet. The Reynolds number is a non-dimensional number $Re = UD/\nu$, where U is the typical velocity at the exit of the jet, D the jet diameter at injection and ν is the kinematic viscosity of the fluid. It represents the ratio of hydrodynamical forces to viscous stresses. Usually when $Re > 300$ the viscous effects are

negligible, and for $Re > 1000$ the jet is generally turbulent.
Thereafter we present the physical description of the spatial development of an axisymmetric (round) jet. It is generally accepted that the free round jet is unstable for Reynolds number greater than the critical value $Re_c = 10$ (Viilu, 1962), and become turbulent for $Re > 1000$ (Crow & Champagne, 1971). In fact the critical Reynolds number depends on the shape of the exit jet profile and on the structure (amplitude, dimension) of the disturbances.

3.1. Physical description

In fact, turbulent jets are present in many physical processes and technological applications, like for instance in combustion chambers where the efficiency of turbulent mixing is important with regard to the performance of combustors. Thus it is not surprising that most of theoretical, numerical and experimental studies deal with fully turbulent jets, which often occur in industrial applications. A general review on laminar and turbulent jets is given by List (1982) for plane jets and by Michalke (1984) for axisymmetric jets. In contrast, detailed examinations of the jets for low Reynolds number and in the near zone of the exit are scarce in the literature.
We give here the physical description of a jet flowing into the same quiescent fluid through a circular orifice in a vertical plane. It is well-known that for high enough Reynolds number the jet is unstable, and the axisymmetric shear layer near the exit jet roll up into coherent vortices which interact strongly downstream before they explode into turbulence. Numerous studies give evidence of the existence of two distinct zones in jet flows, a transition zone and a turbulent zone. In the literature, we note that the turbulent zone has received much more attention than the transition zone, especially at low Reynolds number.
The transition zone starts from the exit jet and has a length of approximately three times that of the inlet height D. For $Re > 300$ it is characterized by the development of the well-known Kelvin-Helmholtz instability. It represents the intrinsic instability of the axisymmetric shear layer formed by the discontinuity of longitudinal velocities cross-stream. Indeed this shear layer is unstable to a large class of infinitesimal perturbations which may originate from the boundary layers inside the pipe flow.
These instabilities are convective instabilities, in the sense that an applied local disturbance will grow exponentially as it propagates downstream, convected by the flow. In this region the velocity profiles comprise a large potential core inside where the longitudinal velocity is quasi-uniform, and a thin shear layer which entrains the ambient surrounding fluid. The thickness of the potential core diminishes with distance, while the concentration of vorticity due to the KH instability evolves into ring-like vortices (roll-up). These coherent structures evolves in a complex manner before they collapse at the end of the transition zone initiating turbulence.
In the turbulent zone, there exist small scale vortices which are the result of the blow-up of the large-scale ring vortices formed upstream. Further downstream the jet flow becomes fully developed, and the jet profile shows a geometrical similarity along the jet axis.
Thus, if we want to determine how a round jet or plane cross-borehole jet flow can be measured with a flowmeter based on the motion of suspended particles, attention should be paid to the transition zone near the exit jet. Indeed the variability of the measured velocities might be important and correlated with small turbulent eddies, if for instance the sampling volume would be positioned in the far zone of the jet. In the transition zone, the instability are developing and weak. Thus we might expect and assume that the flow is almost stationary with an almost uniform profile.
The near zone of three-dimensional laminar jets has been less studied than the far turbulent zone. However we know that this zone becomes unstable, when $Re > 10-30$ and is

characterized by the development of K-H instabilities. The characteristics of this zone vary when the Reynolds number increases or when the initial/boundary conditions change. For large Reynolds number $Re > 1000$, the near-zone is rather well-known for both planar and round jets, however it is only recently that the behavior of this zone has been studied for lower Reynolds number. These results might be important for the analysis of flow-logging data, and are reported after.

3.2. Plane jets

The velocity profile of a laminar planar jet, first obtained by Bickley (1937), gives an accurate description of two- dimensional jet flow provided one is not too close to the source of the jet, approximately $x/D > 10-20$. In this far region, the steady plane horizontal jet velocity along the centreline in the **x** direction diminishes like $x^{-1/3}$ while the jet spreads in the y direction like $x^{2/3}$, and has a symmetric $sech^2 y$ profile. The Bickley profile has been observed experimentally by Andrade (1939) and Sato & Sakao (1964), among others.
However, a planar jet is unstable when the Reynolds number is of the order of 10. Small-scale velocity disturbances, which arise naturally in any experiment, are amplified as they move downstream and can generate large-scale flow structures in the form of vortices that dominate the flow field. Stability analysis shows that the planar jet is unstable to two different types of velocity disturbance, one symmetric about the jet centreline and the other antisymmetric (Lessen & Fox 1955; Tatsumi & Kakutani 1958; Clenshaw & Elliot 1960). The disturbances travel as a wave along the jet, with a characteristic wavelength and frequency.
The perturbation velocity of the symmetric mode has a maximum on the jet centreline; oscillations on either side of the centreline are in phase. In contrast, the amplitude of fluctuation is zero on the jet centreline for the antisymmetric mode, and oscillations on either side are in anti-phase. When a velocity perturbation is applied to the planar jet, it can excite these two spatial modes of instability. After the jet has amplified a preferred mode of instability, nonlinear effects give rise to a roll-up of large-scale spanwise vortices that dominate the flow field.
Sato [14] found experimentally that these instabilities were predominantly dependent on the jet's inlet velocity profile. A uniform jet inlet velocity profile was found to be associated with symmetric or varicose mode instability, whilst a fully developed parabolic jet inlet profile was found to be associated with asymmetric or sinuous mode instability. However observations of the near field planar jet at slightly greater than the critical Reynolds number, by Beavers and Wilson [4], showed that the natural breakdown of the jet was essentially symmetric for low Reynolds number and that the instability and vortex formation were sensitive to external perturbations irrespective of the inlet velocity profile.
However linear stability analysis, assuming an inviscid parallel flow, results in the well-known Orr-Sommerfeld equation. Solving the Orr-Sommerfeld, subject to the appropriate boundary conditions, shows that the first mode predicted to become unstable is the anti-symmetric mode, at $Re \approx 4$; the symmetric mode is found to remain stable until $Re \approx 80$. Usually, the observed coherent structures in the near-zone have characteristic growth rate and frequency which match rather well the linear stability predictions. However, the linear stability results should depends on the local profile of velocity, and thus of the position along the centerplane jet. Finally the growth rate of the modes depends on the Reynolds number and on the type of profile.
For these reasons, most previous experimental studies assume that the anti-symmetric mode is the most unstable for all Reynolds numbers, and therefore more likely to arise in experiment. It can be reasonably accepted that this is true, although the symmetric mode have been found to exist intermittently, in the transition zone and for sufficiently high Reynolds number. It was

mixed with a strongly amplified anti-symmetric unstable mode.
The nonlinear evolution of the dominant anti-symmetric mode is recognized by the formation of large-scale spanwise vortices occurring alternately about the jet centerplane. Further downstream self-induction of the rolls and secondary spanwise instabilities deform the spanwise rolls in the turbulent zone (far zone). The interactions of the coherent structures in the far region is extremely complicated, and has enabled scientists to analyze the dynamics of new three-dimensional coherent structures in the flow field.

3.3. Round Jets

The near zone of a round jet is an evolving coherent structure where an axisymmetrical shear layer encapsulates an irrotational core that has a length of approximately three times that of the inlet jet diameter D. The axisymmetric shear layer is defined by the exit jet profile V_{z0} and the jet diameter $D = 2R_0$. The exit jet profile is characterized by the jet diameter D and the momentum thickness Θ_0,

$$\Theta_0 = \int_0^{\infty} \frac{V_{z0}(r)}{V_{z0,max}}\left(1-\frac{V_{z0}(r)}{V_{z0,max}}\right)dr \qquad \textit{and with } Re = \frac{V_{z0,max}D}{\nu} \tag{2.18}$$

It is generally accepted that the free round jet is unstable for Reynolds number greater than the critical value $Re_c = 10$ (Viilu, 1962), and become turbulent for $Re > 1000$ (Crow & Champagne, 1971). However the transition to instationarity is not well-known.
Among the scarce experiments reported in the literature, we must report the experiment conducted by Reynolds(1962), who observed a variety of jet break-up by varying the Reynolds number in the range 10 to 1000. he reported four different forms of flow structure. For $10 < Re < 30$ a weakly unstable stationary jet flow; for $30 < Re < 150$ axisymmetric structures are observed; for $150 < Re < 300$ long sinusoidal undulations of the jet axis dominate the flow field; for $Re > 300$ the jet becomes turbulent very close to the exit jet. The first bifurcation of the flow is the Hopf bifurcation is the sense that the observed axisymmetric structures are associated with periodic variations of the local velocity.
Batchelor & Gill (1962) attempted to predict theoretically (linear local stability) the disturbance characteristics observed in the axisymmetric jet observed by Reynolds (1962). They considered the instability of a uniform, so called "top hat", jet profile

$$\frac{V_z(r,z)}{V_z(0,z)} = \begin{cases} 1 \; si \; r < D/2 \\ 0 \; si \; r > D/2 \end{cases}$$

They considered an inviscid flow subject to three type of disturbances: axisymmetric (varicose) disturbance, simple helical disturbance and a double helical disturbance. For this profile, analytical solutions of the Orr-Sommerfeld equation can be obtained. It shows that the profile is unstable to all disturbances, and that they have the same growth rate.
Taking experimentally measured profiles for a jet with $Re = 300$, Mattingly & Chang (1974) have found that the most amplified mode is the axisymmetric mode in the near zone of the exit jet, while the simple helical mode become dominant when $z / D > 3$. The preferred mode are characterized by their natural frequency f_n or its Strouhal number $St = f_n D / V_{z0}$. Large Strouhal numbers are associated with dominant axisymmetric instabilities in the flow, while small Strouhal numbers are associated with dominant helical instabilities (see Plaschko, 1979). Similar results are reported by Cohen & Wygnansky (1987).
Michalke (1965, 1984) considered different profiles in tangent hyperbolic form for the mean longitudinal velocity

$$\frac{V_z(r,z)}{V_z(0,z)} = \frac{1}{2}\left[1+\tanh\left(\frac{1}{2}\frac{R}{\Theta}\left(1-\frac{r}{R}\right)\right)\right]$$
$$\frac{V_z(r,z)}{V_z(0,z)} = \frac{1}{2}\left[1+\tanh\left(\frac{1}{2}\frac{R}{\Theta}\left(\frac{R}{r}-\frac{r}{R}\right)\right)\right]$$

in order to account for the spatial dependence of the mean profile and of the corresponding growth rate of the disturbances, from the exit up to the transition zone. As the distance from the exit increases, the parameter R/Θ decreases and modifies the characteristics of the instabilities. For an inviscid flow, this parameter is the only parameter specifying the characteristics of the instabilities.

- for $R/\Theta > 25$, the axisymmetric and helical mode have similar growth rates;
- for $5 < R/\Theta < 10$, the axisymmetric mode is the most amplified instability;
- for $2 < R/\Theta < 5$ the helical mode is the most amplified.

However for a viscous flow, Moris (1976) has shown that, for a fixed value of R/Θ, the influence of the Reynolds number may be important when $Re < 1000$. Using the same previous profiles for the whole near zone, he has shown that:

- for $Re = 500$, the growth rate of the axisymmetric mode and of the simple helical mode are almost identical.
- for $100 < Re < 500$ the helical mode was found to be dominant.

Besides, he showed that the dominant observed modes in the near zone depends sensitively on the characteristics of the initial perturbations.

The same analysis was done by Mollendorf & Gebhart (1973) for a mean-flow profile similar to that of boundary layers to analyze the stability of the far-zone. The axisymmetric mode is always unstable, and the helical mode becomes unstable for $Re > 36$ with a monotone increase of its growth rate with increasing Reynolds number. There is furthermore no preferred (with maximum growth rate) frequency for the helical unstable modes, in contrast with the profiles used in the near-zone of the jet.

In summary, the typical wavelength of the initial dominant instability is $0.6D$ for an **unforced free round jet**, and we may consider that for $Re > 300$ the near-zone of the jet extends to about 3-4 diameters and is dominated by the development of a preferred axisymmetric instability whose characteristics depends on the parameter R/Θ, and for the viscous cases also on the Reynolds number.

In the case of a **forced free round jet**, the characteristic frequencies will depend on the excitation frequency and on the amplitude of the disturbances. For small to moderately large Reynolds number, the selection of the most amplified mode is the near-zone of the jet is related with the distribution of initial energy contained in the "external" disturbances between the axisymmetric and helical modes.

4. Hydraulic modeling and inversion with acoustic flowmeters

Here, we consider borehole in which the vertical flow is negligible in order to study only cross-borehole flows. This can be justified by simple considerations on the hydrodynamic stability of pipe-flows. It is well known that these flows become unstable when the Reynolds number based on the diameter of the borehole D_b and the mean vertical velocity in the borehole, is greater than about 1000. For a borehole filled with water (viscosity $\nu \approx 10^{-6}$) and with a typical 6-inch diameter ($D_b = 15.24\,cm$), the critical velocity for the flow to become unstable equals to $V_{vert} = 0.66\,cm/s$, which is equivalent to a critical averaged flow rate $Q \approx V_{vert} D^2 \approx 2.4$ gal/min (551 liter/hour). This value is much larger than observed vertical

flow. Thus we will consider that if the vertical flows are usually quasi-stationary, we can easily extract this flow from the data by comparative analysis of different borehole logging data.
If we focus on cross-borehole flows, we understand that the sampling volume should be preferentially positioned in the near-zone of the exit of the open fracture. In this region, the flow is expected to be weakly varying in time for low Reynolds number, typically for $Re < 100$. Now this Reynolds number is based on the diameter or the height of the fracture across the borehole and the exit velocity at the opening.
In practice, if an aperture producing water in the borehole is thinner than the vertical dimension of the sampling volume, the log will seldom provides accurate measurement of the thickness or physical properties of that bed because. Under these conditions, the volume of investigation may include mixing with smaller adjacent apertures. This implies that fractures with thickness greater than the height of the sampling volume can not be investigated reliably.
However, we have seen that three-dimensional jets behave like noise amplifier since they are unstable to almost all type of perturbations. Besides it is well-know that acoustic perturbations are very efficient excitations of jet instabilities if the Reynolds is sufficiently high. This aspect has never been considered in the context of acoustic borehole logging systems, and will be investigated after.
Finally we will provide simple models for mean-flow profile description in the near-zone and in the far-zone of plane and round jets. If the size of the sampling volume is greater, but of the order of the height of the fracture, then we expect inversion of flow rates to be possible with simple analytical models of the mean-flow in the near-zone. If however the sampling volume cannot be positioned in the near-zone, a mean-profile for the far-zone is provided too.

Chapter 3 :Experimental studies

1. Introduction

Complementary experimental studies have been carried out in the water tank at LMA, in order to improve our understanding of the measurement of the mean velocity of the fluid within the sample volume of the ultrasonic system. Special attention was paid to the positioning of the sample volume relative to the round jet exit at the wall.
The goal of this research work is to provide useful information on the jet flow, in order to explain some features of the variations of the estimated velocities. However, it should be pointed out that the experimental conditions prevent us from going to far in this analysis. Indeed, a deep-analysis would require highly controlled experiment with regard to, for instance, the design of the jet exit which determines the characteristics of the flow regime near the exit of the jet exit for a given mean inflow rate. In these experiments, we have an insufficient knowledge of the variability of the flow, but this should not prevent an analysis to be done in order to correlate the estimations of the mean velocity within the sample volume with the characteristics of the transducer and the fluid motion.
This chapter reports an analysis of different flow regimes near the exit of a round-jet at the idealized plane borehole wall. Special attention is paid to the positioning of the sample volume relative to the axis of the round-jet flow. This happens to be very important in the case of low flow rate, when the gravity forces dominate the displacements of the outgoing scatterers that fall down just at the exit of the jet. For moderate to high flow rate, the positioning of the sample volume is also important since there is spatial variation of the axial velocity profile along the axis of the transducer or, equivalently, with the distance from the borehole wall.

2. *Description of the experiments*

The experimental set-up has already been described elsewhere and will not be reported here. The reader is referred to Monnier et al. 2003 and Guillermin and Sessarego 2004, for further details.

Briefly for the present experiments, the ultrasonic data sets consist of acoustic echoes from Kaolinite particles added to the water flow. A 5-MHz Panametrics spherically focused transducer was used to emit large-band, burst signals at the pulse repetition frequency *PRF*=5 KHz, i.e the time interval between two consecutive bursts is $T_R = 1/PRF = 200\mu s$. The parameters of the experiments are summarized in the following table

Transducer frequency f_e	5 MHz
Transducer 6-dB bandwidth	2.5 MHz
Focal length	2.54 cm (1 inch)
Length of the focal zone F_z	6.4 mm
Beamwidth D_{6dB} (at focal plane)	0.51 mm
Transducer diameter	15 mm
RF sampling rate f_s	10 MHz
PRF	5 KHz
Acoustic velocity	1480 m/s

Three different series of experiments were carried out at LMA for three different values of the distance between the transducer focal point and the wall, namely $d_w = 0.78$, 1.5 and 2.74 mm . The focal point is assumed to be at the center of the sample volume of measurement. The size of sample volume depends on the characteristics of the transducer, as well as on the pulse waveforms. However, it may be roughly seen as a cylinder with a section corresponding to the 6-dB beamwidth in the focal zone $D_{6dB} = 0.51$ mm, and an axial length that equals to the transducer length of the focal zone $F_z = 6.4$ mm. The axis of the transducer was aligned with the axis of the round-jet exit at the borehole wall. The diameter of the circular exit of the jet flow is $D = 5$ mm.

For each series of experiments the flow rate is fixed, and 2 sets of data are created separately. Each set of data consists of 10 series of 50 pulses emitted successively without interruption of the acquisition system. The data are stored by series of 50 records of RF echo-lines of duration equal to T_{PRF} . To analyze the reproducibility of the measurement a second set of data are collected under the same conditions. Thus, for a given flow rate and position of focal point relative to the borehole wall, the total number of saved files is 20, and it corresponds to a total number of $2 \times 10 \times 50 = 1000$ records of RF-echo lines. Analysis of the data collected during the experiments will be presented in the next section.

3. *Results*

The vast majority of pulsed Doppler systems use the autocorrelation technique, also referred as the one-dimensional (1D) autocorrelator or pulse-pair technique, for velocity estimation. The most attractive property of this technique is its modest computational requirements, while its performance has been judged to be satisfactory, both on the basis of simulations and experimental measurements (Monnier et al. 2003, Leuwwen et al. 1986).

Nevertheless, the pulse-pair method has a number of limitations, some of which have been identified by Loupas et al. 1992. The inferior performance of the (1D) autocorrelator in comparison with other estimators using data from several range cells have been presented by Bonnefous et al. 1986, Ferrara and Algazi 1991, Loupas et al. 1995. Lai et al. 1997. In this case the movement of the scatterers between the range cells has an influence on the statistical properties of the estimates. These algorithms belongs to the class of wide-band velocity estimators, and their performance depends on the accuracy of the underlying theoretical model to account for the effect of the velocity on the received signal.
In this study, each range cell along the beam has been processed individually without filtering the received RF signals. The effect of using receiver filter (finite-length window) can be used to averaging over a range cell the output from the Doppler signal at the desired range (depth location). The effect of using receiver filter has been studied in the context of blood velocity estimations to suppress clutter from moving tissues and other spurious echoes. Nevertheless, the benefit of using such filtering technique to increase the performance of the pulse pair method is rather limited as it was demonstrated by Loupas et al. 1995. However, we will see in the next section that an optimal range of cells or depth locations can usually be associated with low values of variance of velocity estimates obtained with narrow-band techniques. These optimal range cells depend also on the characteristics of the transducers, and is generally located near the focal plane where the signal-to-noise ratio is expected to be the best in the sample volume.

3.1. Preliminary analysis

In this subsection, we consider one series of experiments when the focal plane was located at 0.78 cm from the jet exit located at the borehole wall. Statistical properties of the velocity measurements are inferred from estimation of mean frequency and variance of the Doppler spectral density. Thus, we will use narrow-band estimation techniques.
In a practical system, the RF signal is sampled in the continuous time parameter t, which corresponds to the axial position $z = ct/2$. After sampling with radial increments $dz = 0.075$ mm ($dt = 0.1\mu$ s, $f_s = 10$ MHz), the range-gated RF data can be represented by a 2-D complex random matrix $G(n,m) = \tilde{g}_m(2ndz/c)$. Along the vertical dimension are units of slow time separated by the pulse repetition period T_R and in the horizontal direction are units of fast time that is proportional to axial distance from the center of the transducer, bounded by the receive gate length. Hence, each row represents the range-gated portion of the signal signature as given by (2.8) and (2.9). The signatures are given by:

$$g_k(t) = \mathrm{Re}\left\{ g_k(t) e^{i\omega_0 t} \right\} \tag{3.1}$$

for $2z_1/c \le t \le 2z_N/c$ where

$$\tilde{g}_k(t) = e^{i\omega\beta t} \sum_{k=0}^{N_p - 1} \tilde{r}\left(t - k\beta T_R\right) \tag{3.2}$$

and where z_1 and z_N are the initial and final depth of the receive gate. Each column vector of the matrix G corresponds to a sampling depth $z = ct/2$, and successive elements are separated by T_R. This vector will be referred to as a signal snapshot of the Doppler process. In theory, each vector is assumed to be a realization from a zero-mean, complex, Gaussian process. The stationarity of this process can be justified when the observation time over N_p transmission cycles is much less than a characteristic time of the fluid flow, under which the velocity has varied within the sampling zone.
The number of statistically independent snapshot vectors in the complex matrix G is

determined by the spatial time-bandwidth product of the range-gated portion of the backscattered echoes (Vaitkus et al. 1998). It can be compared with the number of realizations of independent samples needed to estimate the probability density function of a stochastic process. The spatial time-bandwidth product or "effective" number of independent snapshot vectors over the range cell is given by

$$N_{eff} = N\frac{B}{f_s} \tag{3.3}$$

where B is the RF echo bandwidth. For example with the 5-MHz Panametrics, $B = 2.5$ MHz, and if we use the focal zone ($F_z = 6.4$ mm) the range gate window will be $8.6\,\mu$s, and there will be 86 vectors in total, and the number of independent vectors will be about 21 !
We will consider that the volume of analysis is defined by the depth-to-focus length F_z and beamwidth D_{6dB} of the transducer. Here, the distance between the focal plane and the wall is $d_w = z_{wall} - z_{foc} = 7.8$ mm. The sample volume is defined by $z_1 = 2.20D$ and $z_N = 0.93D$, where D is the jet diameter. Because $D_{6dB} = 0.51$ mm and $D = 6.4$ mm, there is an uncertainty in the positioning of the sample volume. However, we will assume that the axis of the transducer is aligned with the axis of the circular jet. Thus, we will consider that the estimated velocities correspond to the axial velocities of the fluid.
Figure 1(a) shows the first RF echo line contained in the file 'd02b000001.dat' which consists of 50 RF echoes lines over the fast-time range $130-150\,\mu$s. The signal from the borehole wall occurs at approximately 145 μs, while the useful backscattered signals occur within the range $130-140\,\mu$s for this example.
In the sample volume, we compute for each cell the total energy of the Doppler signal, defined as

$$E(t) = \frac{1}{N_P T_R}\int_0^{N_P T_R} \tilde{G}(t,\tau)^2\, d\tau \tag{3.4}$$

1(b) shows the total energy of each Doppler signals at cells ranging from 130 to 139 μs. This curve is normalized by the energy of the most energetic Doppler signal in the sample volume. The dot-cross symbol labels the position of the Doppler signal sampled at the focal plane, about 134.32 μs. In this case, the region about the focal plane shows Doppler signals with large energy.

However, this is not always the case. The amplitude of the backscattered echoes depends on the concentration of particles within the sample volume. Thus, the location within the sample volume is not always at the focal plane but vary randomly, from file to file, i.e from series to series of 50 pulse shots. This is shown in figure 2 and 3

Figure 4 and 5 show that when the inflow rate decreases to $Q_0 = 2$ l/h, the energy of the Doppler samples is lower. From experimental observations, this can be explained since less particles move towards the transducer as they fall under gravitational effects. Moreover, one should point out that the flow with Q_0=2 l/h and Q_0=6 l/h are in very different hydrodynamic regimes. The lowest flow rate produces a swirling jet (axis moves sinusoidally) along the mean axis of the circular jet, while for Q_0=6 l/h the flow if fully turbulent. This can also explain the variation in amplitude of the Doppler signals when the flow rate varies, since the particles concentrations will be affected by different transport processes. At low flow rate, the particles are transported by the mean motion, while for high flow rate the turbulence can play a role by modifying both the mean flow and the statistical properties of the particles concentration.

To analyze the velocity estimations along the transducer axis, we have used the Pulse-Pair method and the Periodogram and Welch method to estimate the Doppler spectral density $P_z(\omega)$ (see Chapter 2), from which we could estimate the mean frequency Doppler shift and the Doppler bandwidth of the signal by using formula (2.13) and (2.15). The variance of the velocity estimation at each depth location is given by

$$var(V_z) = \frac{c}{2}\frac{\sqrt{\sigma_\omega^2}}{\omega_e} \tag{3.5}$$

where $\omega_e = 2\pi f_e$. .

Figure (6) shows the velocity estimates along the beam axis of the transducer with the three different methods, for $Q_0 = 2$ l/h and $d_w = 0.78$ cm. As expected, the pulse-pair method has the lowest variance in the estimation of the velocities. In general, the lowest variance in the estimation corresponds to the depth locations where the energy in the Doppler signals is significant. Low energy in the Doppler signal results in great variability of the velocity estimation. In the bottom graphic of figure (6), the crosses labels the depth locations with normalized energy in the Doppler signal greater than 0.7. The tables 2 and 3 provide the velocity estimates corresponding to the crosses in the bottom graphics of figures (6) and (7).

gate	V_z (Period.)	V_z (Welch)	V_z Pulse pair)
1	5.46	6.34	5.17
2	5.67	6.08	5.28
3	5.39	6.12	5.28
4	5.64	6.17	5.25
5	6.04	6.70	5.36

Table 2. $Q_0 = 2$ l/h and $d_w = 0.78$ cm, file: d2b000001.dat

gate	V_z (Period.)	V_z (Welch)	V_z (Pulse pair)
1	6.00	6.19	5.30
2	5.22	5.88	5.15
3	5.23	5.92	5.14
4	4.80	5.72	4.88

Table 3. $Q_0 = 2$ l/h and $d_w = 0.78$ cm, file: d2b000008.dat

Figure (7) shows that it can be dangerous to use spatial averaging filter, as the energy of the Doppler samples can be very low over a large region of the sample volume. Usually, these regions of the sample volume with low energy Doppler signals produce very irregular spatial velocity distributions due to very low signal-to-noise ratio. If we use the depth location corresponding to the focal point (middle circle in bottom graphic of figure 7), the velocity will be estimated as 7.15 cm/s. Instead, when we use only the range cells whose normalized energy exceeds a certain critical threshold (here the threshold value is chosen to be 0.7), we see that the estimates are more consistent. From file to file, tables 2 and 3 shows that we can obtain reproducible estimates of the velocities at random locations in the sample volume. The mean of the velocity estimates , obtained by the pulse-pair method, is 5.27 cm/s for table 2, and 5.12 cm/s for table 3. With this criterion threshold one can thus isolate a group of range cells, here about 4 to 5 cells, where the estimation is expected to be reliable. This is an important conclusion because we usually do not know a priori of the values of signal-to-noise ratio in the Doppler samples.

With this protocol, we increase the probability of correct estimation of the velocity. Usually, an axial window is used to analyze the RF lines, independently of the estimation method. However, the length of this window will be determined by the pulse characteristics and the presence of noise. With this protocol, we can determine the optimal depth location with a threshold criterion, as well as the window-length. We have used short pulses for which the best windows have length equivalent to four to six times the acoustic wave length. Although, we do not use spatial averaging filter in this study, we note that the threshold criterion leads to a group of 4 to 6 consecutive gates for the velocity estimation which corresponds to the best length. This indicates that the value of the threshold criterion should be considered with window-length consideration.

For a larger flow rate, $Q_0 = 6$ l/h, the flow is highly turbulent and instabilities develop immediately at the exit of the jet. Figures 8 and 9 show 2 estimations of the velocity distribution for the same set of experiments. It is clear that the flow is non uniform in time (from file to file). Processing the file 'd6000002.dat' gives lower velocity estimations than with 'd6000008.dat'. We can only approximate the time elapsed between the savings of these records to be 7*(50*200) μs $\approx$ 7 ms. Indeed, the true time is greater since we do not known the time taken for input/output operations in each file.

Because of the random occurrence of large concentration of particles within the sample volume, the range cells are selected randomly within the sample volume. Tables 4 and 5 give the velocity estimations for each of the 4 groups of cells associated with the bottom graphics of figures 8 and 9. Because the flow is highly turbulent, we expect to measure the instantaneous velocity of the fluid in different regions of the sample volume.

gate	V_z (Period.)	V_z (Welch)	V_z (Pulse pair)
1	7.68	7.59	7.76
2	7.52	7.77	7.28
3	6.52	7.95	6.80
4	7.67	7.29	7.21
5	7.15	8.12	7.03
6	7.58	7.82	6.76
7	7.92	7.34	7.17

Table 4. $Q_0 = 6$ l/h and $d_w = 0.78$ cm, file: d6000002.dat

gate	V_z (Period.)	V_z (Welch)	V_z (Pulse pair)
1	10.74	10.70	10.63
2	10.71	10.62	10.53
3	10.43	10.57	10.29
4	10.24	10.42	10.19
5	10.51	10.51	10.46
6	10.57	10.53	10.36
7	10.45	10.14	10.25
8	10.32	10.39	10.33
9	10.11	10.52	10.47

10	9.60	9.93	9.92
11	9.49	9.36	9.42
12	8.63	8.85	8.84
13	8.65	8.12	8.75
14	8.51	8.34	8.68
15	8.24	8.98	8.31

Table 5. $Q_0 = 6$ l/h and $d_w = 0.78$ cm, file: d6000008.dat

One can see that with this protocol, there is little variation of the velocity estimate for each group of cells. This analysis shows that the depth location for estimation should be considered with care to increase the probability of correct estimation of the velocity within the sample volume.

To illustrate this, we consider 1 series of experiment consisting of 10 data files, each corresponding to a series a 50 successive pulse echoes. We analyze each range-gated Doppler signal between $t_1 = 130\,\mu$s and $t_1 = 145\,\mu$s, while the focal zone extends between $t_1 = 130\,\mu$s and $t_1 = 138.6\,\mu$s. For $Q_0 = 2$ l/h and $d_w = 0.78$ cm, the series of files 'd2b00000n.dat' and 'd200000n.dat' (n=0,...9) are analyzed. Figures 10(a) and 11(a) show the significant scatter in the velocity estimations obtained from each Doppler signals in the focal zone. Each graph corresponds to one series of 10 data files for fixed flow rate and fixed distance from the wall. When we apply the threshold criterion to these data samples, we see that useful signal values can occur outside the focal zone. The threshold criterion significantly reduce the number of useful samples and the variability in the estimations, as shown on Figures 10(b) and 11(b). From these selected samples, we obtain from the series of files 'd200000n.dat' a mean velocity $V_z = 5.25 \pm 0.21$ cm/s, and from the series of files 'd200000n.dat' a mean velocity $V_z = 5.40 \pm 0.20$ cm/s. By choosing carefully the Doppler samples, we can obtain reproducible estimates of the velocities with good accuracy.

To see the effect of increasing the flow rate, we consider $Q_0 = 6$ l/h and $d_w = 0.78$ cm, and thus analyze the series of files 'd6b00000n.dat' and 'd600000n.dat' (n=0,...9).

In this case the flow is highly turbulent. The threshold criterion is still useful to eliminate spurious estimates. We can suppose that our estimates based on this threshold technique may be sufficient to obtain reliable estimates. Figures 12(b) and 13(b) show that in the first series of files 'd600000*.dat' reliable estimates are located about the focal plane near $t = 135\,\mu$s, while in the second series of files 'd6b00000*.dat' they are closer to the wall near $t = 138 - 140\,\mu$s. In the first series of files 'd600000n.dat' we get a mean velocity $V_z = 10.76 \pm 0.80$ cm/s, and from the series of files 'd6b00000n.dat' a mean velocity $V_z = 12.25 \pm 0.75$ cm/s. It is interesting to note that the results are consistent with an increase of the velocity as the sampling zone gets closer to the exit of the jet.

3.2. Influence of the sample volume position

We will briefly analyze the influence of the distance between the focal plane of the transducer and the wall, since we never know the "exact" position of the sample volume. We consider separately 2 series of 10 files for each flow rate and each position of the focal plane, $Q_0 = 1.2$, 2, 3, 4 l/h and namely $d_w = 2.78$, 1.5, 0.78 cm respectively.

We analyze each range-gated Doppler signal between $t_1 = 120\,\mu$s and $t_1 = 145\,\mu$s, while the focal zone extends between $t_1 = 130\ \mu$ s and $t_1 = 138.6\ \mu$ s. In the zone of interest we apply the threshold criterion for each file, and thus we obtain a random number of velocity estimation values at the selected depth gates. For each series of 10 files, the mean velocity is obtained by statistically averaging over these random estimations. The upper and the lower graphics of figure 14 correspond to one series of 10 files, varying the position d_w and the flow rate Q_0.

Figure 14 shows that the axis of the transducer was probably not correctly positioned with respect to the jet axis. Indeed, one can see that as the distance between the focal plane and the wall decreases, the velocity estimation values decrease. If the beam axis was aligned with the jet axis, the velocity values would have to increase. When off-axis, the velocity is expected to decrease when the distance from the wall decreases. Thus the sample volume with a characteristic width $\approx D_{6dB} = 0.51$ mm is probably located in the entrainment zone of the jet, off-axis. This can explain the tendency observed in figure 14.
The variance of the estimations decreases when the distance between the wall and the transducer focal plane is minimal. In this case, the sample volume is positioned near the potential core of the jet. Here we hope that when the jet is not turbulent, we can suppose that the flow is quasi-uniform and that we can use the profile of the linear stability analysis to represent the mean flow distribution at the jet exit.
Figure 14 shows that the analysis proposed in this report can reproduce reliable results of the velocity, consistent with the pattern of the flow. We expect the best velocity estimations to be obtained close to the wall by using the threshold criterion on the energy of the Doppler signals. we should emphasize here that this study reveals that "simple" signal processing technique can be used to obtained reliable velocity estimations that are consistent with the flow pattern. It would therefore be interesting to make a similar experiment, but with controlled positioning of the sample volume with respect to the circular jet, in order to study the spatial and the temporal characteristics of the jet. This study shows that this method allows to do this.

3.3 Estimations of inflow rates

Here we will consider the measurements obtained with $d_w = 0.78$ cm. In this case, the focal zone of the transducer covers the region between

$$2.20 < z_{wall}/D <= 0.93$$

where z_{wall} is the distance of the rang gate z from the wall. Although the previous analysis indicates that the sample volume in our measurements was not positioned on the jet axis, we will make this assumption for the following suggestion of inversion method. Here, we propose a solution which uses a velocity estimation inferred from experimental data and a model of flow, in order to determine the flow rate at the exit of the jet located at the wall.
From the measurements, we can obtain an average velocity V_z^{mes} which can be combined with one of the following models for the mean flow distribution with $V_z(0,z) = V_z^{mes}$

- model A

$$\frac{V_z(r,z)}{V_z(0,z)} = \begin{cases} 1 & si \quad r < D/2 \\ 0 & si \quad r > D/2 \end{cases} \tag{3.6}$$

- model B

$$\frac{V_z(r,z)}{V_z(0,z)} = \left(1 - \frac{2r}{D}\right)^2 \tag{3.7}$$

- model C

$$\frac{V_z(r,z)}{V_z(0,z)} = \frac{1}{2}\left[1 + tanh\left(\frac{1}{2}\frac{R}{\Theta}\left(1 - \frac{r}{R}\right)\right)\right] \tag{3.8}$$

with $R/\Theta \approx 0.5$ for $z > 6D$

From these profiles, we can estimate the total flow rate in the section. We assume that this is approximately the same flow rate at the exit, since we have chosen the closest positions to the wall to obtain the measurements.

Q_0^{expe} (l/h)	v_z^{mes}	model A (l/h)	model B (l/h)	model C (l/h)
1.2	3.81	1.76	1.72	1.95
1.2	4.42	2.40	2.00	2.26
2	5.25	2.42	2.37	2.67
2	5.40	2.49	2.44	2.76
3	6.70	3.09	3.03	3.43
3	6.71	3.09	3.03	3.43
4	8.01	3.70	3.62	4.10
4	7.77	3.59	3.51	3.98

Table 6. Estimated flow rate for a given Q_0^{expe} and v_z^{mes}

The model B seems to produce the best flow rate estimate. When Q_0^{expe} increases, we observe a transition from a swirling jet to a turbulent jet. It is interesting to note that the model C seems to more appropriate than the model B when Q_0^{expe}. This can be related with the transition to turbulence in the flow. Indeed when this occurs as Q_0^{expe} increases, the extent of potential core of the jet reduces until it disappears when the jet is fully turbulent. Thus, for a fixed position of the focal plane between $2.20 < z_{wall}/D \leq 0.93$, we expect to have a uniform profile of the model type A, while for a turbulent jet we would expect rather the model type C. Nevertheless, we must recognize that in our experiments, we could not know exactly the flow rate or the positioning of the sample volume. Thus this analysis is rather an indication that useful information on the jet flow can be obtained with the ultra sound probe system. More importantly, there appears to be a possibility to estimate the inflow rate from one point measurement of the velocity near the exit of the jet.

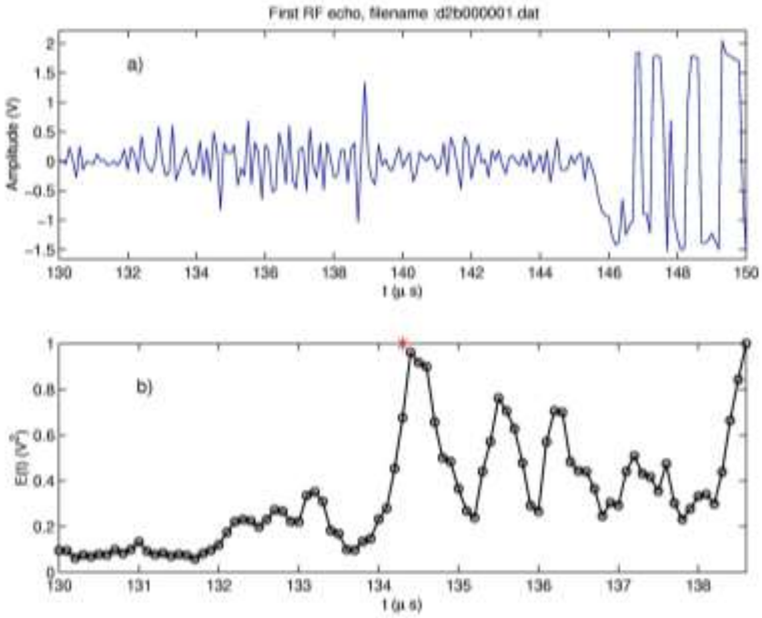

Figure 73-WP6/1. (a) example of RF echo line, (b) example of energy of Doppler signal (for various RF line).

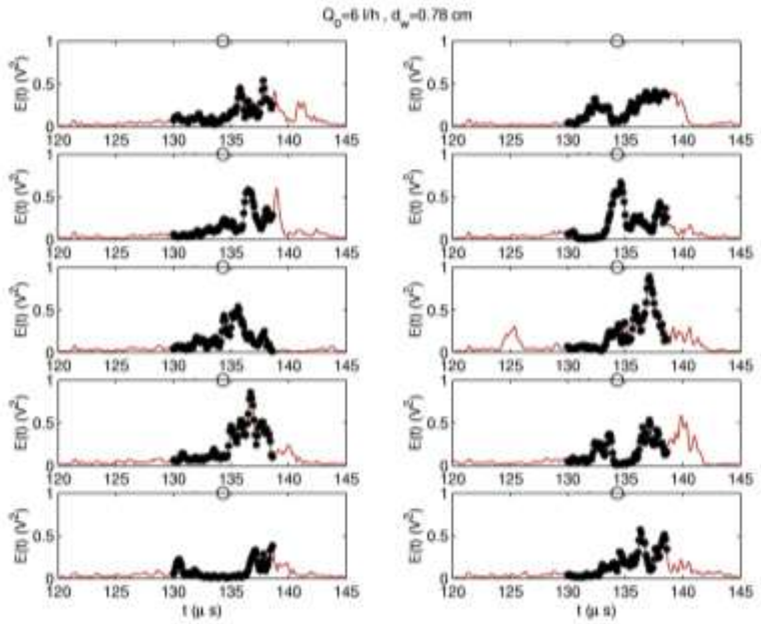

Figure 74-WP6/2. Energy of Doppler samples for 1st series of data with d_w = 0.78 cm and Q_o = 6 l/h.. Crosses label the focal zone, circle labels the focal point.

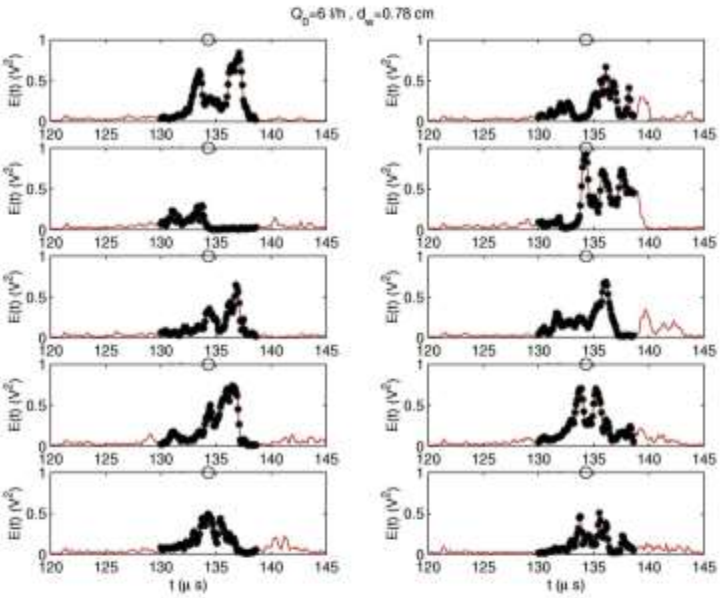

Figure 75-WP6/3. Energy of Doppler samples for 2nd series of data with d_w = 0.78 cm and Q_o = 6 l/h. Crosses label the focal zone, circle labels the focal point.

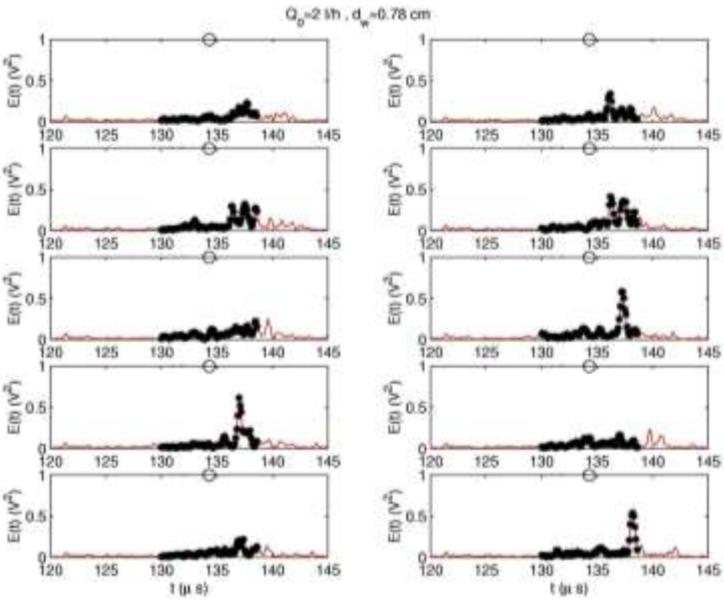

Figure 76-WP6/4. Energy of Doppler samples for 1st series of data with d_w = 0.78 cm and Q_o = 2 l/h. Crosses label the focal zone, circle labels the focal point.

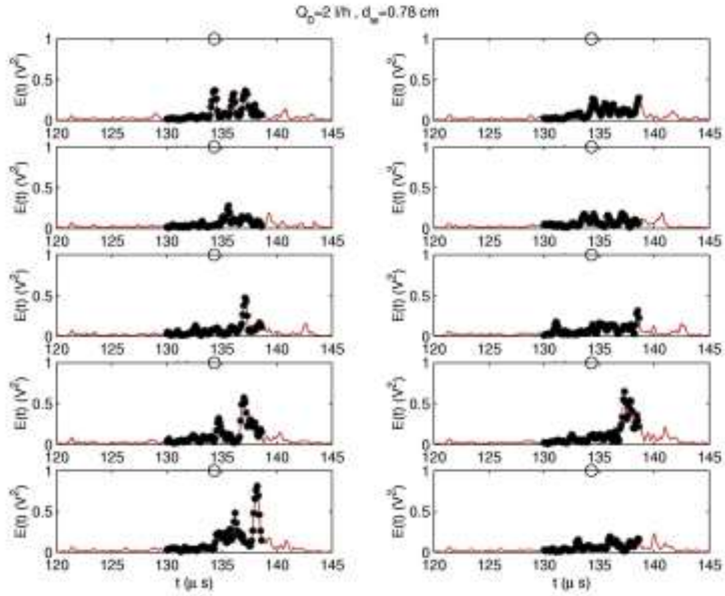

Figure 77-WP6/5. Energy of Doppler samples for 2nd series of data with d_w = 0.78 cm and Q_o = 2 l/h. Crosses label the focal zone, circle labels the focal point.

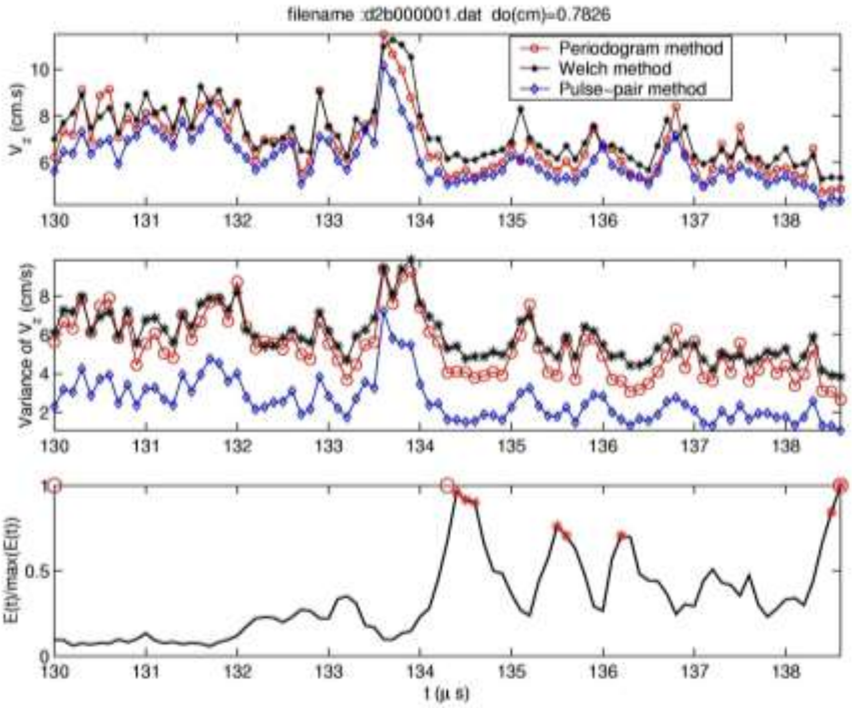

Figure 78-WP6/6. Velocity estimation by three different methods.

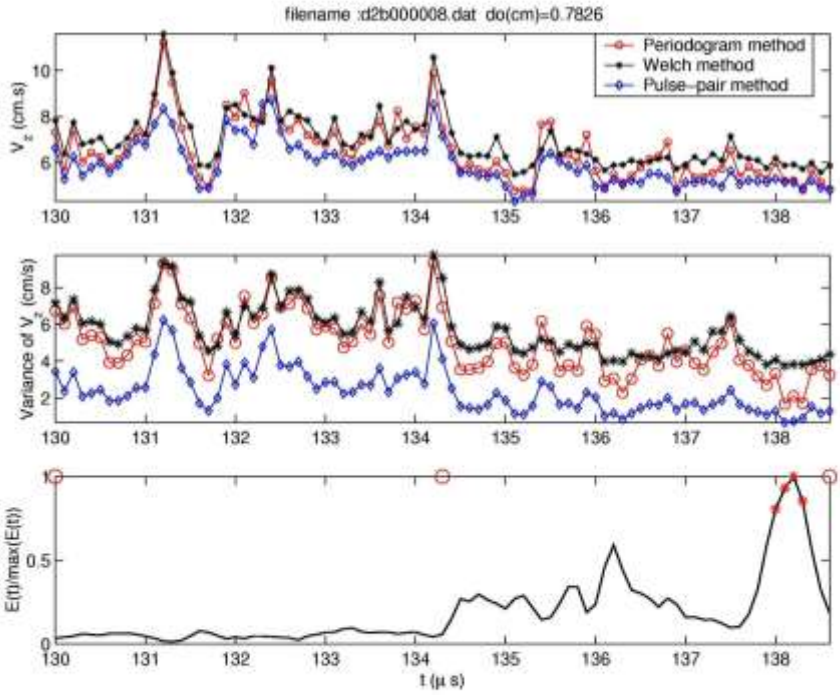

Figure 79-WP6/7. Velocity estimation by three different methods Q_0=2l/h.

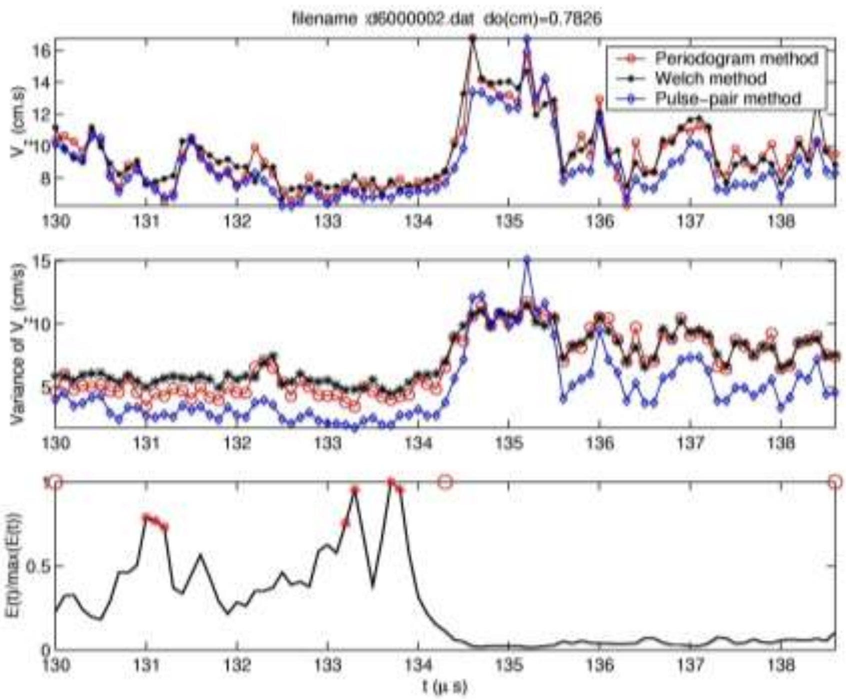

Figure 80-WP6/8. Velocity estimation by three different methods Q_0=6.0 l/h.

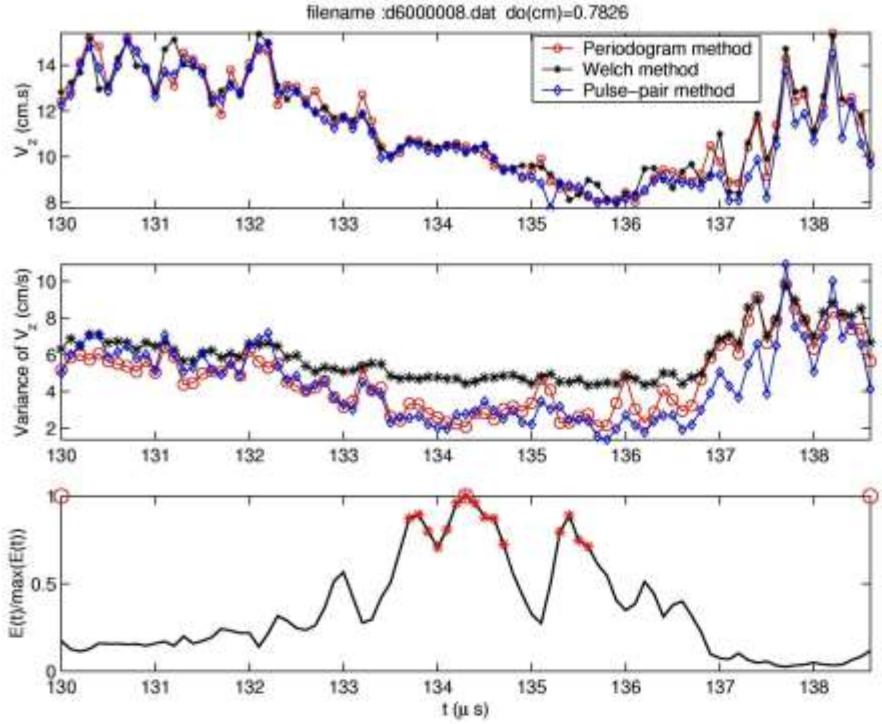

Figure 81-WP6/9. Velocity estimation by three different methods Q_0=6l/h (another experiment).

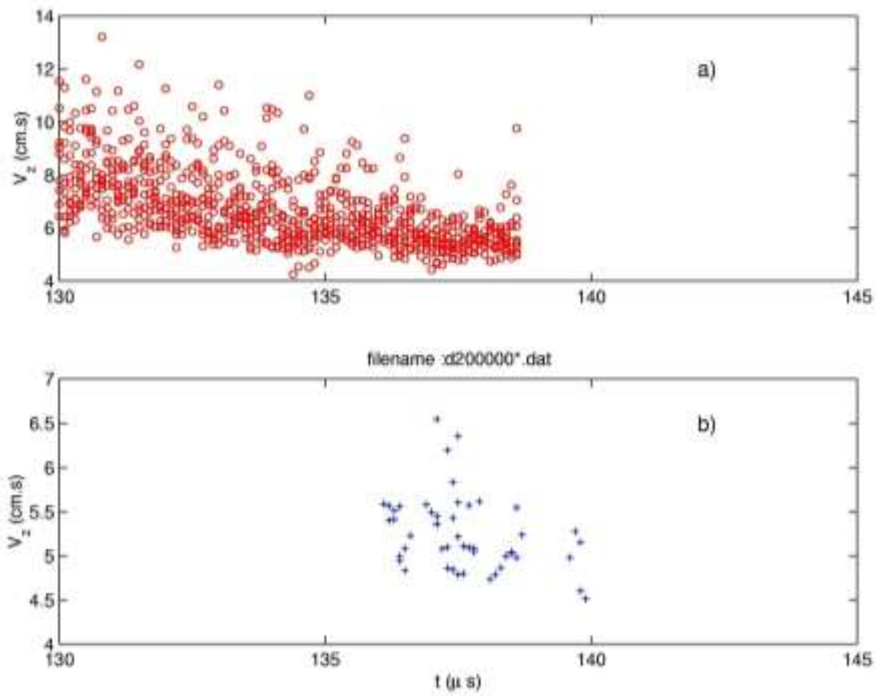

Figure 82-WP6/10. Dispersion of data for the velocity estimation in the focal zone.for different flow velocity (on this graph, the filename corresponds to a relatively low flow rate).

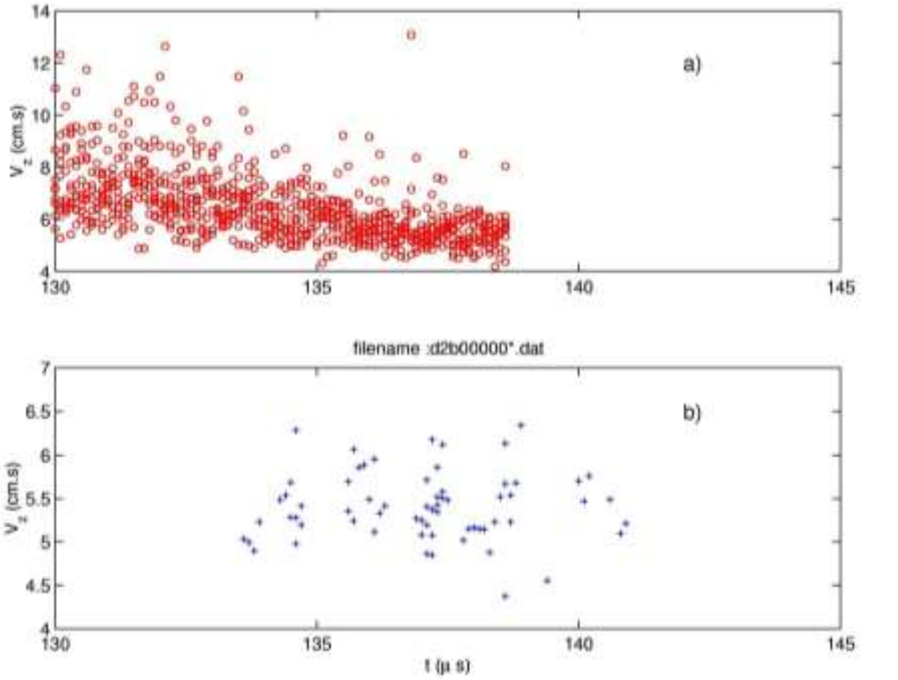

Figure 83-WP6/11. Dispersion of data for the velocity estimation in the focal zone for different flow velocity (on this graph, the filename corresponds to a low flow rate).

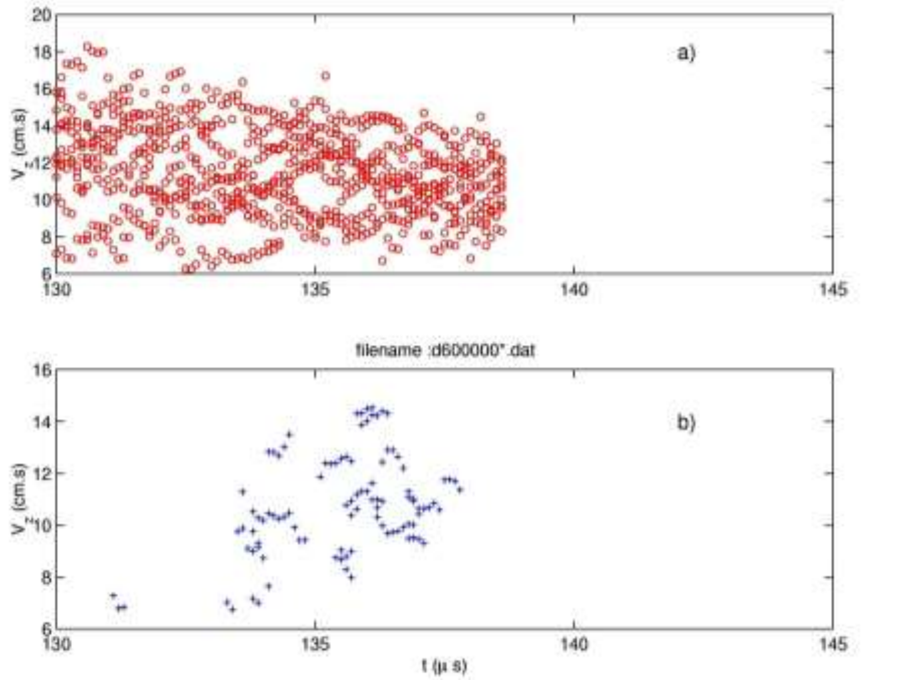

Figure 84-WP6/12. Dispersion of data for the velocity estimation in the focal zone for different flow velocity (on this graph, the filename corresponds to a highly turbulent flow).

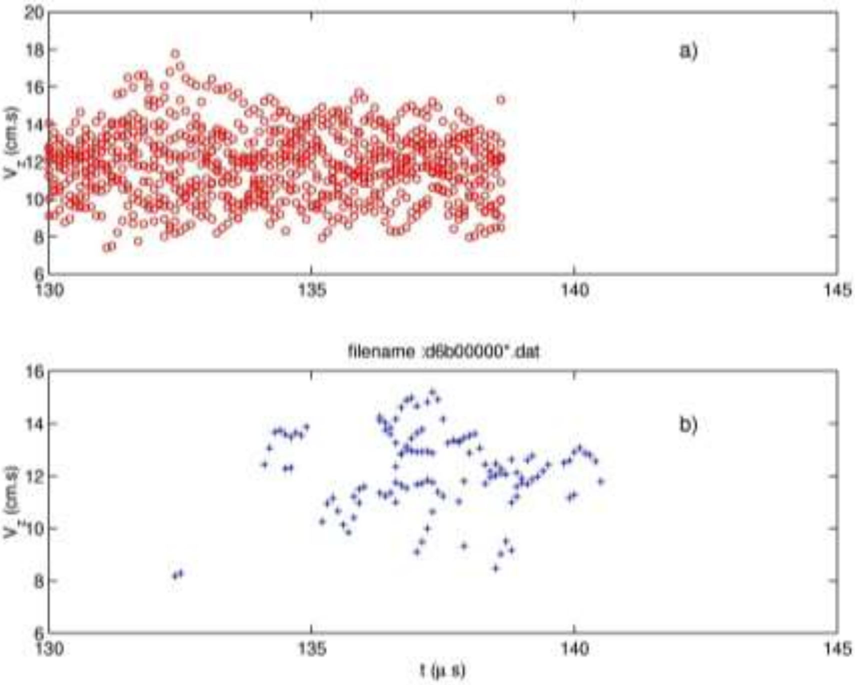

Figure 85-WP6/13. Dispersion of data for the velocity estimation in the focal zone for different flow velocity (on this graph, the filename corresponds to a highly turbulent flow).

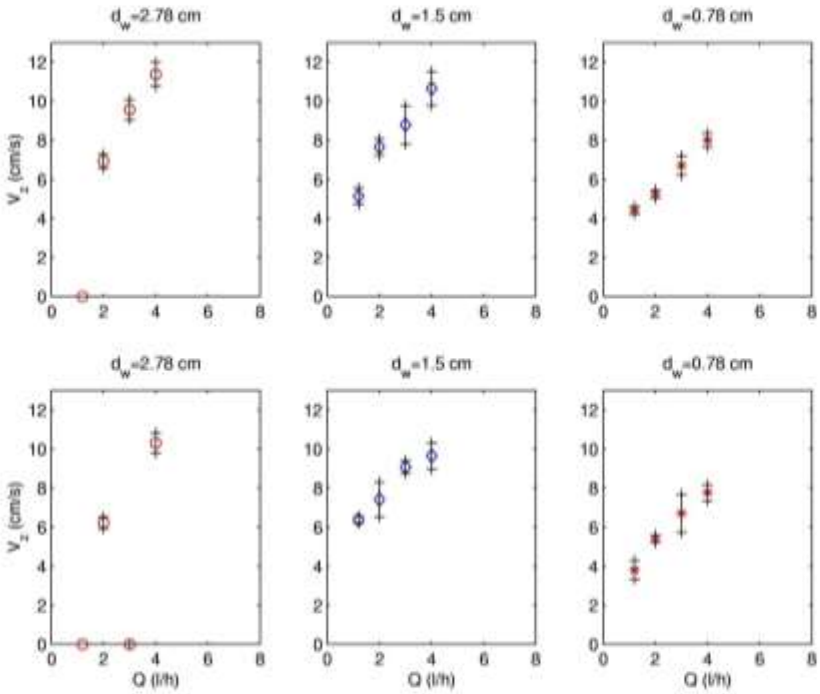

Figure 86-WP6/14. Velocity estimation for different flow rates and for different distance d_w between the focal zone and the wall of the tank.

Work package number: 7
Modelling the EXS / new tools

Objectives and input to work package :

(a) Develop the modelling tools necessary for data processing from new logging/testing equipments and experiments,

(b) Integrate the initial characterisation phase (from WP 1 to WP 4) within a numerical modelling procedure for quantifying transfers processes (hydraulic, brine transport and hydro-electrical effects) at EXS scale.

Task 7.1 Data interpretation modelling: development of logging/testing data modelling tools with a special effort on new sensors and experimental setup.

Partner 2 (Birmingham University - UK)

Modeling water flow and salt transport in fractured rock (software development)

Work on this workpackage at Birmingham has concentrated on the verification and further development of the fracture network modelling software, VodoLei (Figure 8).

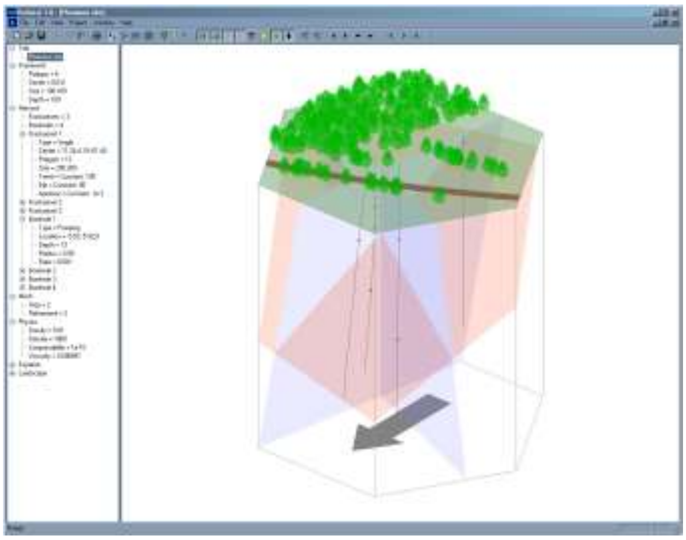

Figure 87. Example of screen from the new code "**VodoLei**" developped by Partner 2 in the course of ALIANCE.

Tests on flow simulations

Quantitative tests on flow simulations have included steady state and transient flow to a well intersecting a fracture. Figure 88 shows the simulated steady state head distribution close to a pumping borehole against the theoretical Thiem solution. With the semi-automatic local grid refinement built into the software, exceptional accuracy can be achieved even at the borehole itself. This accuracy will be essential in the analysis of the field tests.

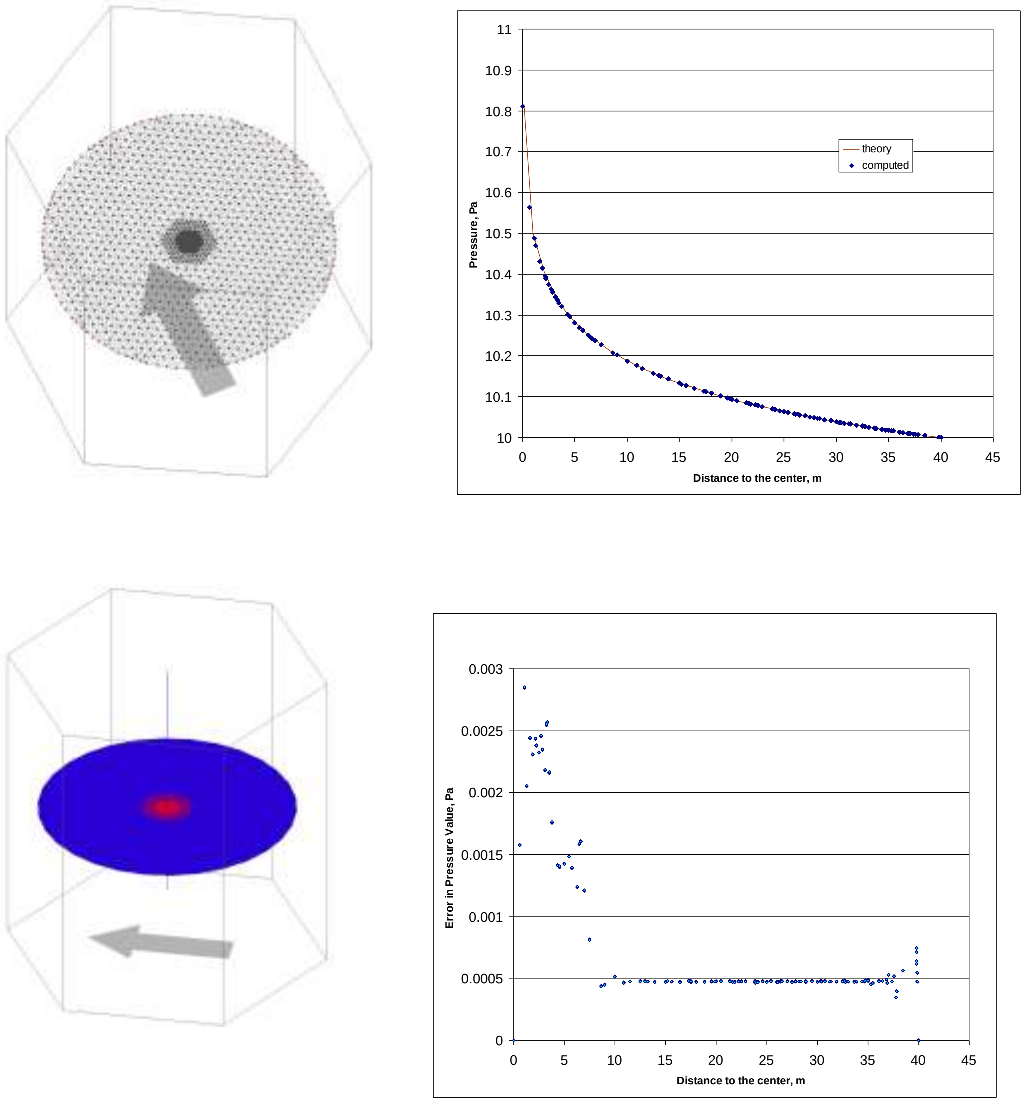

Figure 88. Simulated head values achieved under transient flow conditions, using a circular fracture with a uniform grid and fixed head boundary conditions on the perimeter, against a theoretical Theis curve and the errors in calculated drawdown. Even close to the abstraction well at early times, the accuracy is within 1.5 mm. The sudden turn down in the error curves indicate the effect of the boundary conditions on the cone of depression.

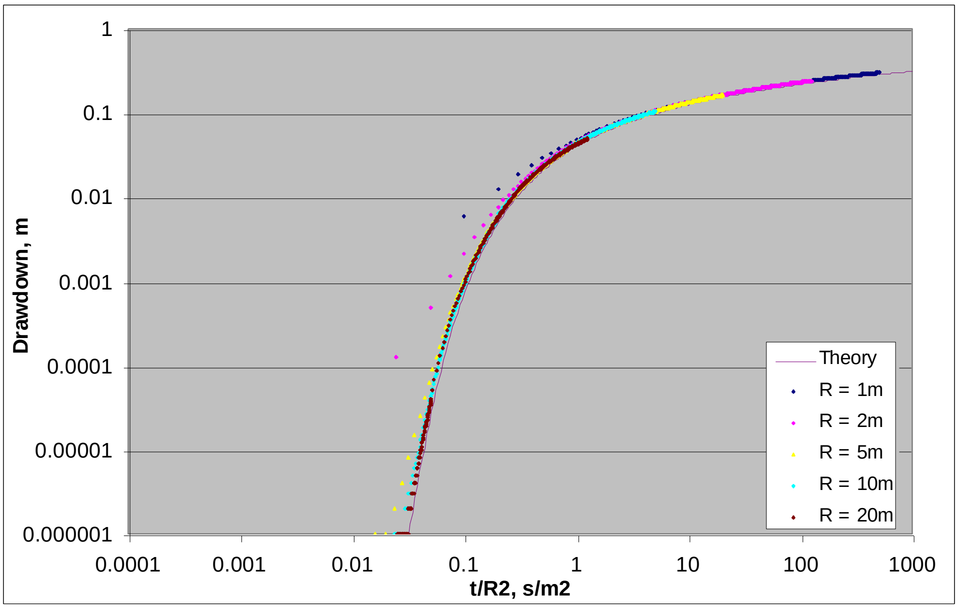

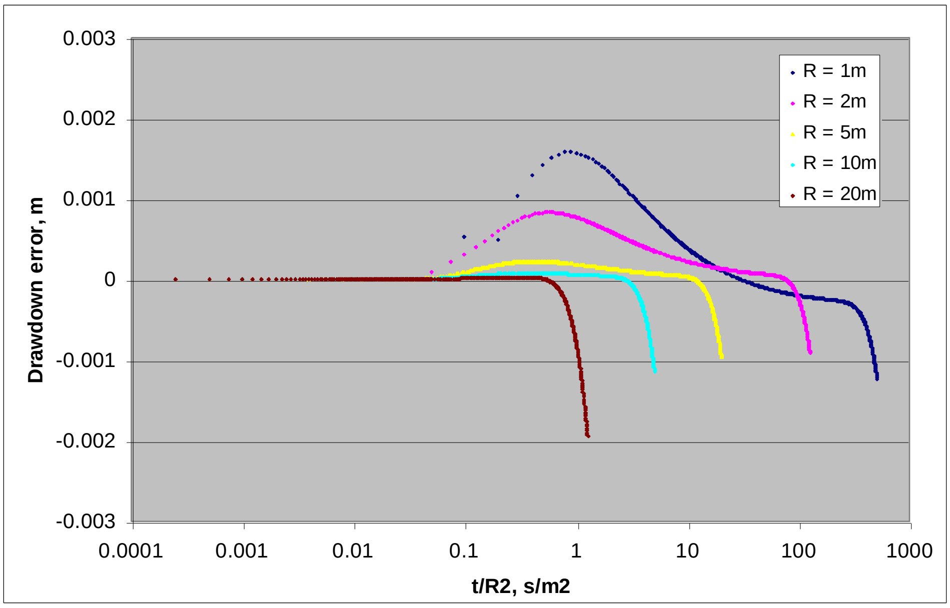

Figure 89. Influence of the mechanical coupling between fracture aperture (hence transmissivity) and fluid pressure. The steady state solution near an injection borehole with and without the effect of hydro-mechanical coupling is presented.

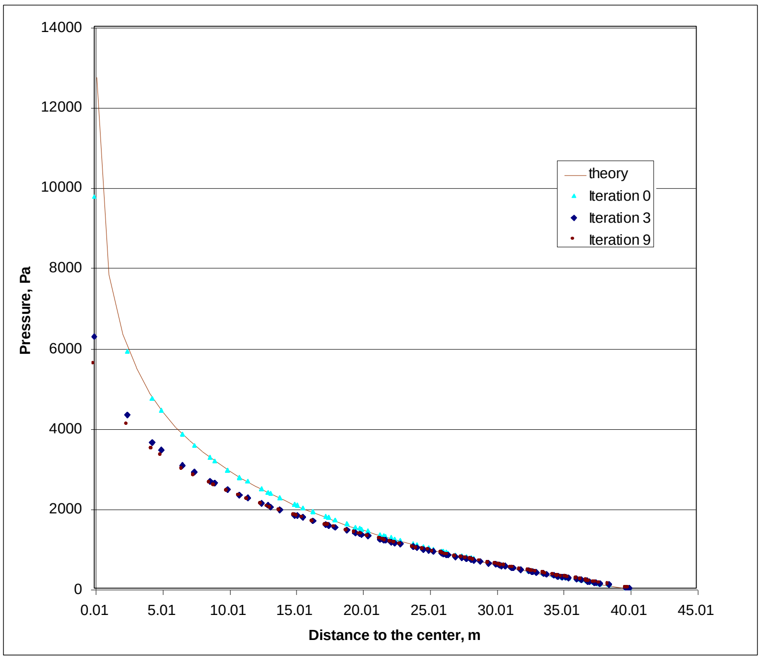

Figure 90. Tests of the transport code against analytical solutions. The capability of the code to model the field tests is demonstrated here.

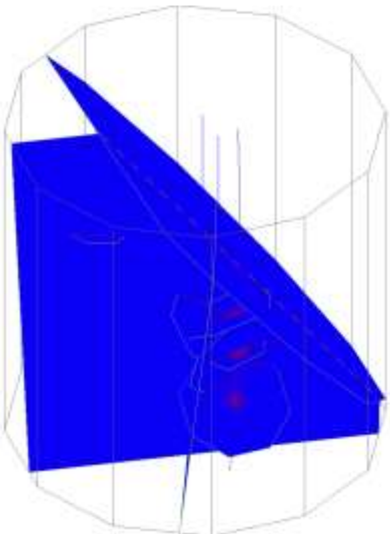

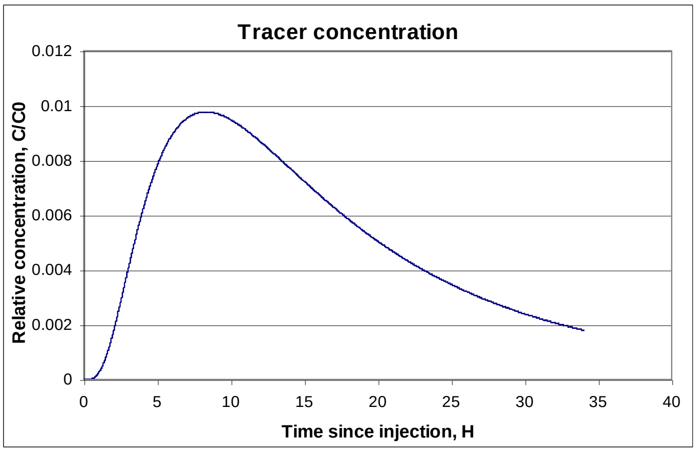

Figure 91. Work is underway on the rigorous verification of the coupling of flow and transport required to simulate density-dependent flow and hence salt transport.

Work package number: 8
Modelling the SWS

Objectives and input to work package :

(a) Apply specific tools / experiments modelling tools developed in WP 7 to the SWS,

(b) Integrate the initial characterisation phase data (from WP 2 to WP 4) as part of a numerical modelling procedure for quantifying transfers processes (hydraulic, brine transport, geochemical processes and hydro-electrical effects) at the SWS, then extrapolate to aquifer scale,

(c) Validate the data acquisition/modelling protocol for saline intrusion investigation using the experimental and monitoring results.

Partner 3 (ETH – Zurich – Switzerland)

Spectroscopic analysis of water level data

This chapter describes the analysis of the water level data recovered from the Ses Sitjoles saltwater wedge site in Mallorca. More specifically it investigates the relationship between sea level variations and the movement of the groundwater table as inferred from water level fluctuations measured in wells. From the magnitude and the delay of the sea-level signal at the site we can constrain the value of hydraulic diffusivity on a scale of many kilometres. In order to establish that the sea level and well level fluctuations are correlated and causally related, we carry out a cross-spectral analysis of three different signals: sea level variation, air pressure fluctuation and water level variation. The analysis yields the transfer function between sea- and well-level fluctuations that describes how the former affects the latter. In a second step we can fit the transfer function to that predicted to result from one-dimensional pressure diffusion to constrain the horizontal hydraulic diffusivity of the aquifer that transmits the pressure between the sea and the site.

Results

The form of the transfer function between the water level variations at well North in Ses Sitjoles and the sea level suggests that the coupling occurs through diffusion of a pressure wave through the reef unit. As a first attempt to investigate this, we have attempted to fit transfer function with that predicted from a simple a one-dimensional diffusion model. Rather than model the transfer function in the frequency domain directly, it is convenient and conceptually more enlightening to express the transfer function in terms of a Heaviside response in the time domain: that is, to calculate the well time-series response that is predicted to result from a unit step change in sea level. This is readily accomplished by taking the inverse Fourier transform of the transfer function in the frequency domain to obtain the delta-function response in the time domain (i.e. the transfer function in the time domain), and then integrating the result. The Heaviside response derived in this way can then be fit by responses predicted from 1-D diffusion models by specifying the distance over which diffusion occurs (such as the well-sea distance, although this is left as a variable), the magnitude of the step-change in pressure in the aquifer at the sea, and the diffusivity of the aquifer in which diffusion takes place.

The estimated Heaviside response for well North derived from the transfer function is shown by the red line in Figure . It is evident that pressure transmission between the sea and the well is very rapid, even though the distance between the well and the coast is 6 km. The decline in the response at long times is fictitious, an artefact of limited frequency resolution. Similarly, the sharp onset of the plateau in the response at 20 days is uncertain. Examination of the long period behaviour of the parent spectra shows that while the amplitude spectrum appears to be flattening at frequencies below 0.014 cpd (71 days), this is not resolved at the 1 standard deviation error level. Furthermore, the phase is still 20° from equilibrium but is trending in that direction. Thus, it is not clear that the maximum response of well level to sea level variations at very long periods is 0.5, as suggested by the plateau. Within the framework of the 1-D diffusion model, the level of the plateau essentially determines the magnitude of the step-change in aquifer pressure at the sea.

In attempting to fit the Heaviside response for well North with the 1-D diffusion model, three parameters were varied. The first is the distance, z, from the well to the sea. Although the distance from the well to the coast is about 6 km, this was allowed to vary between 3 and 8 km. Shorter distances account for the possibility that the aquifer had such a high permeability near the coast that the essential distance over which diffusion occurred was reduced. Longer paths were included because the precise path of diffusion was unknown and may not follow the line of shortest distance (i.e. tortuosity). Both shorter or longer paths are rendered plausible in the karstic environment in question. The second parameter varied was the amplitude of the step increase in sea level, P(z=0, t=0), this was allowed to vary between 1 and 0.6. For direct contact between the aquifer and the sea, the latter should take a value of unity (i.e. the Heaviside response). However, if the contact is indirect, such as resulting from loading of the aquifer by the sea, the induced pore pressure response within the aquifer beneath the sea would be less than unity. The third parameter is the diffusivity of the aquifer.

A total of 20 models were run using the parameter values listed in Table1. The results are summarised in Figure -Figure which show a series of plots in which the amplitude of the pressure-step imposed at the sea-end of the diffusion path, P(0,0), is varied between 1 (same value as the causal step-change in sea-level) to 0.6. The best-fit is obtained for a P(0,0) value of 0.7 (Figure). Larger values produce overshoot of the data-derived Heaviside response earlier, whereas smaller value does not fit the first and steepest part of the curve. For a P(0,0) value of 0.7, equally good fits were obtained for diffusion paths distances of 3.0 - 6.0 km, and for diffusivity values of 75 – 420 m^2/s. Even the smallest of this range of values is indicative of a very permeable aquifer.

A value of P(0,0) of 0.7 suggests that the aquifer in which diffusion is occurring does not have direct contact to the sea. As noted earlier, the value of this parameter is governed by the long-period asymptote of the transfer function, which we are not able to estimate at periods as long as we would like. Longer data series will help clarify whether the amplitude begins to flatten or continues to increase. If the latter, then the Heaviside response will also continue to increase more strongly beyond 20 days. However, at present it seems doubtful that the true function will increase as strongly as the predicted curve for P(0,0) = 1.0.

Table 2: Parameter values used and fitted in the trial and error calculations

NUMBER FIT	P(0,0)	Z (M)	D (M^2/s)
1	1	1000	4.5
2	1	1500	11
3	1	2000	20
4	1	3000	45
5	1	4000	80
6	1	5000	120
7	1	6000	180
8	1	7000	270
9	1	8000	340
10	0.9	3000	55
11	0.9	4000	80
12	0.9	5000	135
13	0.9	6000	210
14	0.9	7000	290
15	0.7	3000	75
16	0.7	4000	130
17	0.7	5000	220
18	0.7	6000	310
19	0.7	7000	420
20	0.6	6000	800

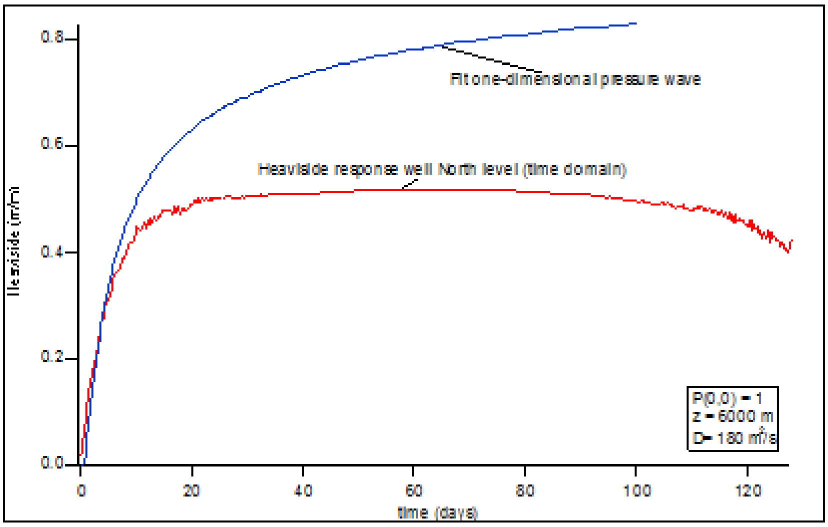

Figure 92. Heaviside response of well North to sea level derived from the transfer function (see above). Also shown is the best fit obtained from a 1-D diffusion model in which the

amplitude of the step-change in aquifer pressure at the sea was taken equal to the unit step-change in sea level.

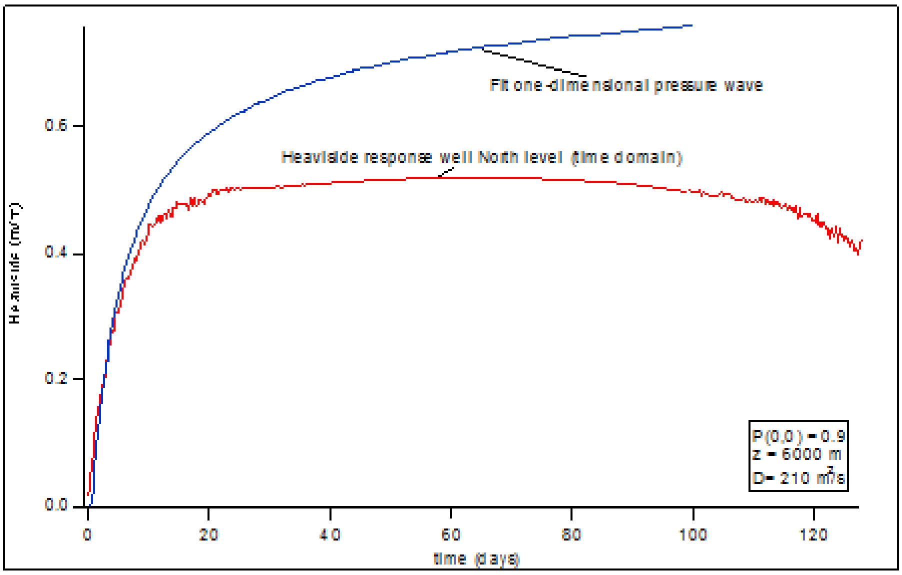

Figure 93. Best fit obtained to the estimated Heaviside response from a 1-D diffusion model that used a step-change in aquifer pressure equal to 90% of the unit step-change in sea level.

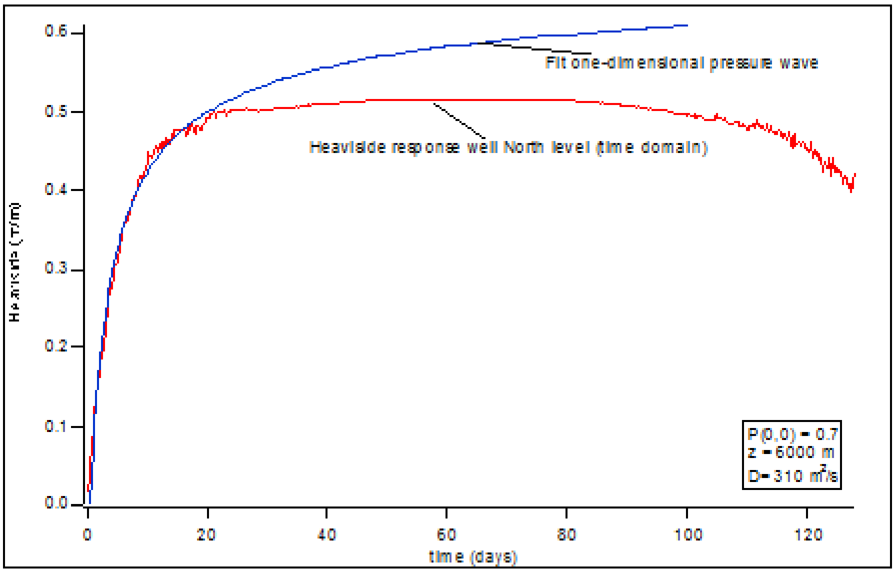

Figure 94. Best fit obtained to the estimated Heaviside response from a 1-D diffusion model that used a step-change in aquifer pressure equal to 70% of the unit step-change in sea level.

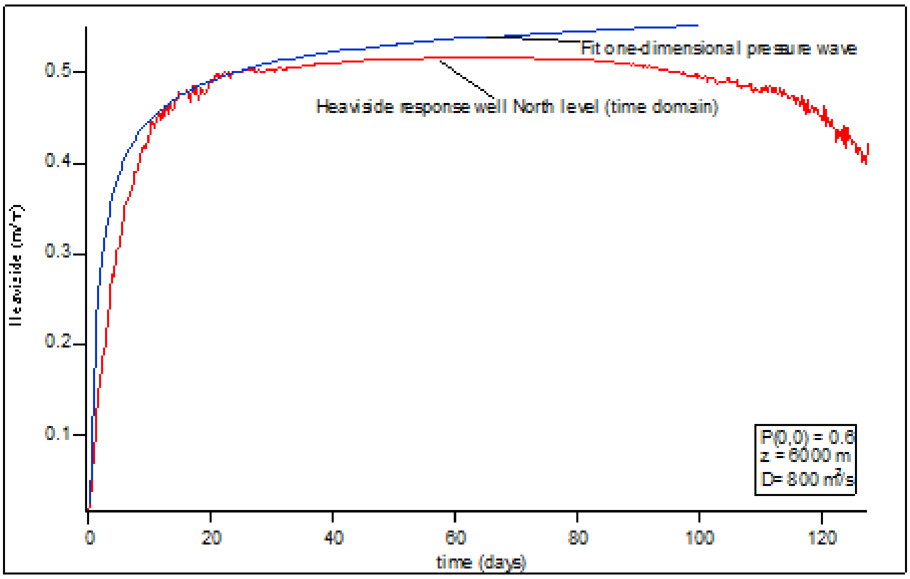

Figure 95. Best fit obtained to the estimated Heaviside response from a 1-D diffusion model that used a step-change in aquifer pressure equal to 60% of the unit step-change in sea level.

Work package number: 9
Monitoring sensors and methods

Objectives and input to work package :

(c) Design the optimal acquisition system and surface configuration for site-dependent deployment of a monitoring system based the hydro-electrical coupling principle,

(d) Study electrokinetic processes in shallow aquifers for diverse flow configurations during experiments conducted as part of WP 3,

(e) Set-up of a long-term monitoring system to document electrokinetic processes by long-term in-situ acquisition.

Partner 1 (ISTEEM – Montpellier - France)

In order to be operational in the context of the objectives of WP9, and prior to the finalization of the EXS and SWS, it was decided in 2003 to take advantage of the development of new experimental sites in the near vicinity of the city of Montpellier. The Maguelone site, located along the mediterranean shore (Figure 96), was further developped in 2004 with the design and first deployment of a downhole resitivity observatory.

Maguelone coastal experimental site

This site is located near the medieval Maguelone cathedral along the shore, between the Mediterranean and a coastal lagoon. It was developped by ISTEEM to study coastal sedimentary processes, and further developped in 2004 with the drilling of a new destructive hole (MAG4) drilled to 46 m, into the fresh water reservoir discovered with MAG1. MAG4 is located along the "Prevost" lagoon, 50 m North of MAG1, hence 150 m from shore, to the east of the cathedral. It was equiped with an intrumented PVC tubing down to 46 m.

Figure 96. Location of the MAG1 and MAG4 (50 m to the NE of MAG1) boreholes, between the city of Palavas (to the east) and the Maguelone cathedral (to the west), 10 km to the south of Montpellier, along the Mediterranean coast.

Surface electrical resistivity profiles (Figure 97) were recorded in a triangle with 64 electrodes spaced a meter appart from each other (Figure 98a), with one of the sides of the triangle relating MAG 1 and MAG4 (Profile 3). Near surface resistivities (> 1 m) are generally in excess of 20 Ω.m 10 to 15 m away from the Prevost lagoon. Below 3.0 m, the resistivity is always under 1.0 Ω.m, showing the presence of brackish water and conductive clays elsewhere found in the MAG1 core.

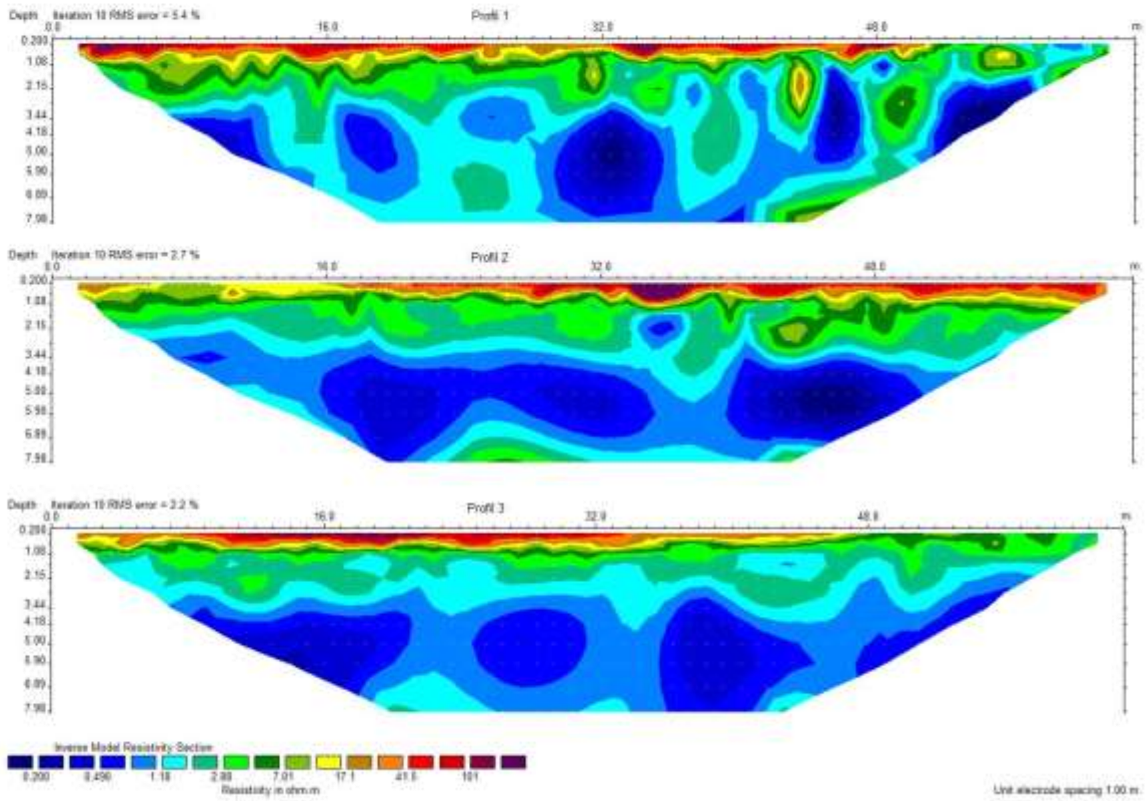

Figure 97. Surface electrical profiles obtained with a 64 electrodes array in a triangle oriented along a NE-SW strike from MAG1 (Profile 1), a S-N strike for the profile going from the SW tip of profile 1 to MAG4 (Profile 2), a NE-SW strike for that closing the triangle, from MAG4 to MAG1 (Profile 3). The surface equipment was supplied by the University of Pau and also used to record the downhole data. Vertical penetration does not exceed 8 m depth.

MAG4 was drilled destructively down to a depth of 46 m, 50 meters North of MAG1 (Figure 98c). A metallic pipe was lowererd gradually in the hole during drilling to avoid collapsing. Black fluids (Figure 98b) charged with products from the reduction of the iron drillpipe by H_2S were extracted from the hole every morning, when drilling resumed. The drilling progressed down to 36 m, where a natural gamma profile was obtained (Figure 99) to evaluate the lateral continuity of the sedimentary structure and whether the fresh water reservoir had been reached. It was consequently decided to drill down to 46 m. Unfortunatly, 4 meters of drillpipe unscrewed to the bottom of the hole while cleaning the hole, and could not be recovered. The hole was sidtracked back to 46 m to install the resistivity observatory.

The natural gamma record obtained in MAG4 down to 36 m compares well with that obtained in MAG1 (Figure 99), requesting a 80 cm shift to overlap the records in the Holocene section (from 7 to 16 m), indicating a one degree dip in the direction of MAG1, towards the shore, and demonstrating the lateral continuity of the sedimentary sequence at the site.

Figure 98. (a) Surface electrical surveys with a 64 electrodes array. (b) Fluid run-off of drilling fluid charged with H_2S reduction products of the iron casing left overnight into the hole for stability. (c) Drilling of MAG4, 50 m to the North of MAG1. (d) First deployment in MAG4 of an electrical monitoring array with 5 mm high gold plated copper electrodes spaced a meter appart from each other along the custom-made PVC casing observatory.

Equiped with 5 mm high gold-plated copper electrodes located downhole every one meter, the observatory with plain PVC (Figure 98d) reconstructs the hydraulic structure present prior to drilling. Each electrode is connected to surface with an individual wire, allowing for repetitive probing and imaging of the formation surrounding the hole with electrical resistivity. The observatory was lowered in 2.8 m-long sections, taking an overall time of 14 hours to deploy 46 m of instrumented tubing. Measurements were made on June 23, immediatly after deployment, and the next day (June 24) to check the repeatability of the system. The probing was done using the Wenner, dipole-dipole and pole-pole techniques, which gaves very similar results. Only the dipole-dipole measurements are presented here (Figure 100).

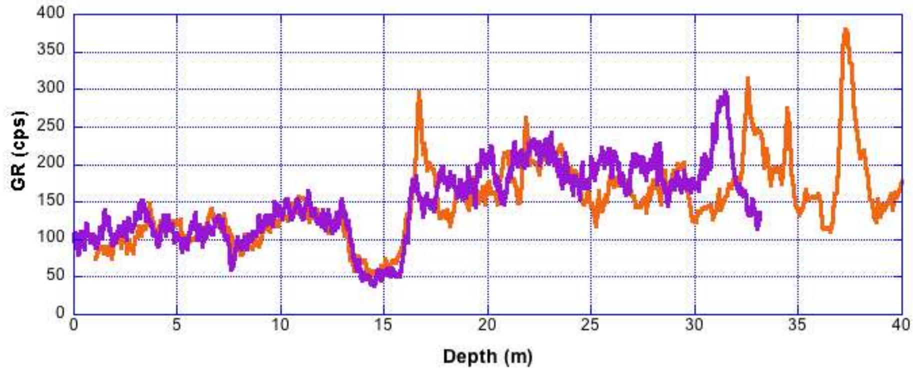

Figure 99. Natural gamma profiles recorded in MAG1 (orange) and MAG4 (purple), and fitted over the Holocene section (6 to 17 m), with a 80 cm shift of the MAG4 record.

The dipole-dipole measurements from the observatory in MAG4 compare very well with the medium induction resistivity from MAG1 (Figure 100; orange profile). Small changes are recorded in the more permeable intervals (with little clay content), while more clay-rich intervals give constant values overtime (19 to 23 m). The effect of near-surface desaturation during summer months is recorded in September (purple dots). The brackish water reservoir (down to 32 m), CH_4 and H_2S gases at about 15 m, and the fresh water reservoir (deeper than 36 m) are imaged by both electrical methods.

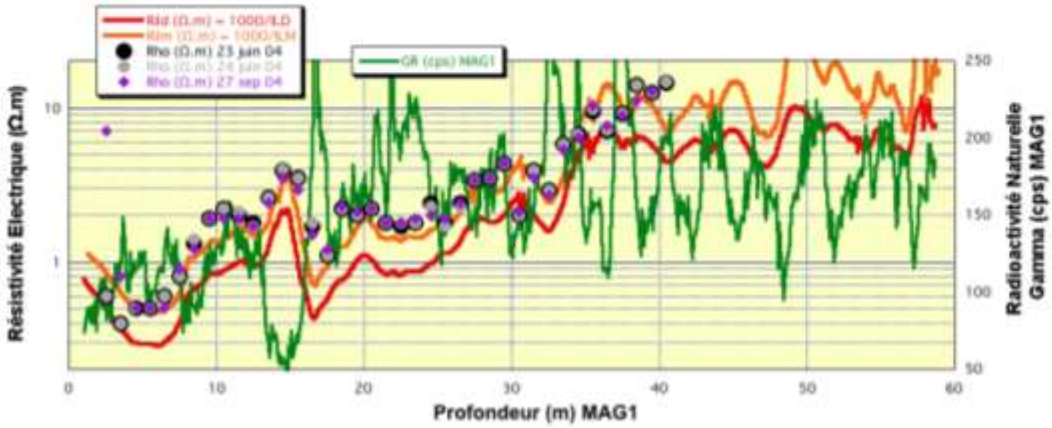

Figure 100. Natural gamma (green) and electrical resistivity (orange and red) profiles measured in MAG1. Dipole-dipole measurements from the observatory in MAG4 made on June 23 (black), June 24 (grey) and September 27 (purple) 2004.

This observatory for permanent downhole monitoring of electrical resistivity in a coastal aquifer is the first ever of this kind deployed in the subsurface. It provides a direct answer to the problem of long-term monitoring of coastal aquifer invaded with salted water.

Partner 3 (ETH – Zurich - Switzerland)

Task 2.4: Traditional monitoring and fluid sampling

To enable the large variety of performed and future possible investigations (long-term evaluation of water levels, active hydraulic testing, combined hydraulic/ geophysical/ hydrochemical experiments, comparison with data from wells outside Ses Sitjoles), a new monitoring system was designed and subsequently modified throughout the ongoing project according to the needs of the individual experiments and investigations. In the following section, results of water pressure measurements are summarized, the system was already described in the second year report.

Long-term time series of hydraulic head at and near Ses Sitjoles

To assess the long-term water level fluctuations at the Ses Sitjoles site, both available data from monthly manual observations of the government of the Balearic Islands together with our measurements starting in 2003 are explored. The time series of calculated hydraulic head is shown in Figure 101. Even thought the historical record has several gaps and uncertainty, the bandwidth of hydraulic head in between 1.45 m asl and 1.70 m asl (dh = 0.25 cm) is regarded as a good estimate of the water level variation. This finding is supported by two independent facts: (1) The farmer wells are tapping only the uppermost 1.5 m of the aquifer and have been operated successfully from the beginning of the 20^{th} century (2) the measurements taken with a high temporal resolution (not shown) do not show fast and extreme events, and hence such events are not expected for the gaps in the long-term record. The small fluctuation is explained by (1) the 40 m thick unsaturated zone that is acting as buffer against precipitation events, and (2) the hydrodynamic connection of the water table to the sea level that forms a stable boundary condition to hydrodynamic fluctuations.

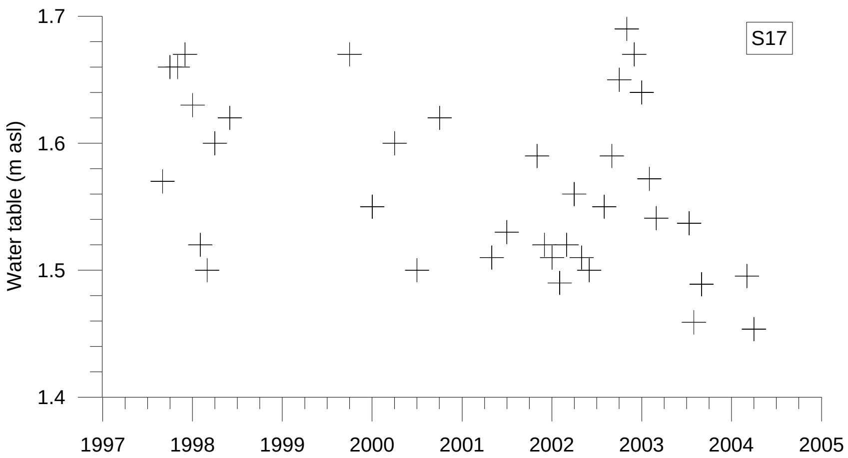

Figure 101. Long-term variation of the water level at Ses Sitjoles.

Data from other locations on the Llucmajor-Campos platform show similar fluctuations. As an example, Figure 102 shows data from S1, in the central part of the platform, approximately 8 km west of Ses Sitjoles. It can be concluded that the platform (10 km scale) has similar hydrodynamic parameters (permeability, storativity) and is subjected to similar excitations (recharge, sea level fluctuations, air pressure variations). This is true even though the water table is at different positions with respect to the reef architecture, i.e. the water table lies within the reefal unit or deeper within the slope deposits.

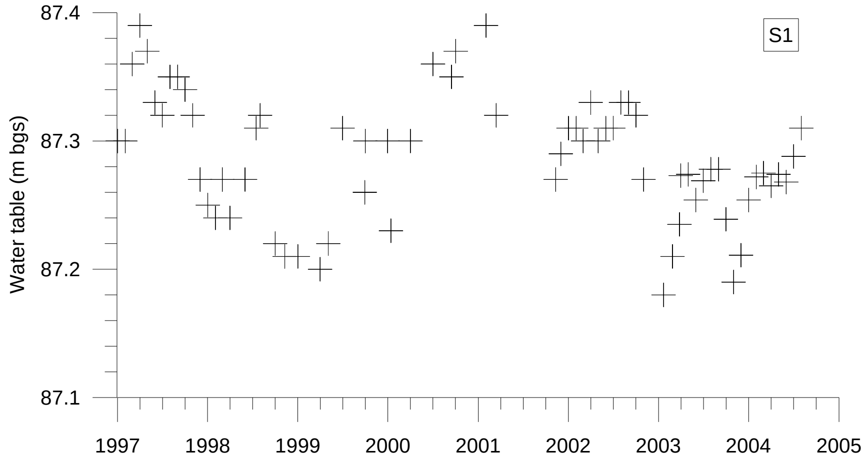

Figure 102. Long-term variation of the water level at the central part of the Llucmajor-Campos reefal platform.

Present status of the monitoring system

The monitoring system consists in the following devices (data are logged every two hours):

- 7 downhole absolute pressure transmitters at MC5, MC6 and S17,
- 1 downhole multi-parameter sonde (relative pressure, temperature, electrical conductivity, pH) at Well North,
- 2 independent air pressure transmitters in the field container,
- 1 downhole absolute pressure transmitter at S16 (outside Ses Sitjoles).

A schematic overview of this monitoring system at Ses Sitjoles is shown in Figure 103. Additionally, the following data from third-party sources are available for future evaluations:

- the government of the Balearic Islands is running several automatic data loggers for hydraulic head and performs monthly water table measurements at various boreholes,
- the oceanographic institute is continuously measuring the sea level at the port of Palma,
- climatic data (rainfall, temperature, humidity) are measured by three different stations at Llucmajor, Campos, and Porreres.

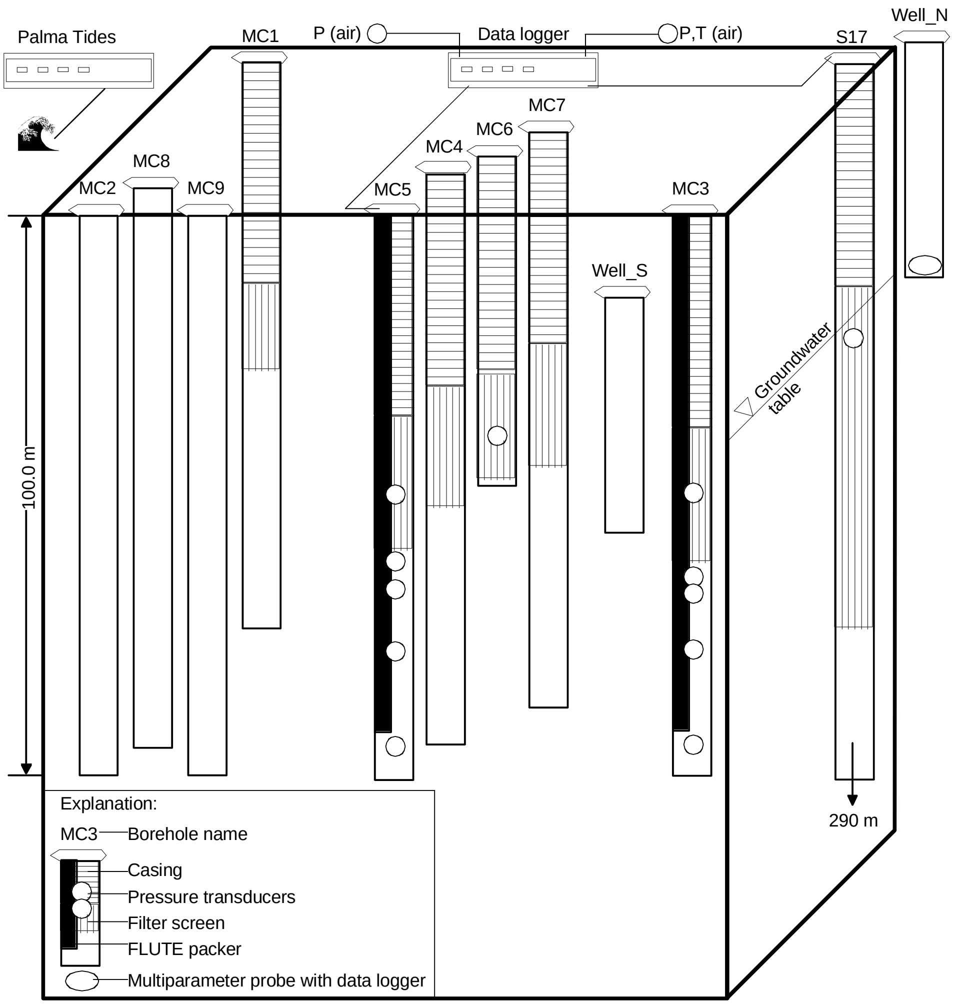

Figure 103. Schematic of the installation at SWS site Ses Sitjoles, view from the south-west.

Work package number: 10
Project management and results dissemination

Objectives and input to work package :

(a) Project management and dissemination of results to end-users and the scientific community via a regularly updated web site, meeting and scientific workshops, reports and scientific publications.

Partner 1 (ISTEEM - France)

The third year of ALIANCE as a whole was focussed on consolidating the work done in relation to the development of the two field sites, both from cores and downhole geophysical data. Particular attention was paid to the development of the "Medias France" database in relation with the H+ ORE project. Most of the management efforts during year 3 were dedicated to reducing the delays in new testing tools development (as part of WP5), leading to the completion and field testing in 2004 of CoFIS and MuSET in Montpellier (Lavalette) and Luxembourg, respectively. Further efforts to complete H2E and DopTV before the end of the ALIANCE extension will be deployed in 2005. Concerning the new set of downhole testing tools, difficulties remained only with the construction of SHyFT by partner 7, where no progress was made over the reporting period.

Monitoring at experimental sites continued at the Ploemeur EXS and Campos SWS sites, and began in Maguelone with the first deployment of a long-term resistivity monitoring array. Concerning the monitoring of electrical properties, pleminary studies have been made in Montpellier to prepare for deployment in 2004 at the EXS and SWS. Site description and the analysis of cores have progressed far beyond initial expectations. In the long run, the cores from Ploemeur (EXS) will be archived by the University of Rennes. The cores from the Campos (SWS) site will be split between Montpellier and ETH Zurich for archiving. Concerning site access in the future and associated data distribution, further progress were made in 2004 with the development of the MEDIAS-France "H+" database. This database will be accessible on-line for research by all scientists in Europe when ALIANCE is completed, including data from both EXS and SWS sites. In November 2004, the support of H+ for the next 10 years by the french Ministry of Research was confirmed.

In December 2004, a one day meeting was held in Paris (France) in order to synthesize the activity of 2004 and prepare for the program extension in 2005. In the final phase of the program (2005), the management activity will be threefold. It will be focussed first on the organisation of final field campaigns in Ploemeur (March) and Mallorca (April), including the downhole testing of new sensors and observatories. Second, a list of papers to report the results obtained as a consequence of ALIANCE will be further developped from the present one (see below). For this, a meeting will be held in Oviedo (Spain) in February 2005 to focus on core analyses. Also, particular attention will be paid to communicating the results of the project, both in the scientific domain and to the general public. Communications to the general public will be made via national media (newspapers and television), the shooting of a short movie showing the field deployment of ALIANCE new tools (partner 1 as part of WP10), and presentation of project results to end members partners (the City of Ploemeur in Brittany, and the Ministry of "Media Ambiante" in Mallorca).

Provisional publications plan for the **ALIANCE project; petrophysical, geological, geophysical and hydrogeological studies** (May 2005)

••• *Papers realted to the Campos and Pollenca sites (Mallorca)*

GEOLOGY (WP2)

MG1.**Aix**+Mop	Sr isotopes dating and geological implications (short paper)
MG2.**Aix**+Mop+VU	Sr isotopes dating and geological implications (detailed paper), with detailed geological description of a reefal structure from MC2 and MC4 holes, plus more from Campos.
MG3 **Aix**+Mop	Detailed diagenesis of a reefal column from MC2 core analyses

SURFACE GEOPHYSICS (WP2)

MS1 **ETH**(DJ)	Macroscopic porosity structure of a Miocene reefal carbonate, Mallorca (Spain)

PETROPHYSICS (WP4)

MP1 **OvU**+Mop+ETH	Pore space structure with hydraulic significance from MC2 cores
MP2 **OvU**+Mop	Hydraulic properties of core from MC2
MP3 **ETH**+OvU+Mop	Microscopic porosity structure of a Miocene reefal carbonate
MP4 **Mop**+OvU+ETH	Static petrophysical study of MC2 cores (Vp, Ø, FF, Cs, ρ_b, ...)
MP5 **Mop**+OvU	Dynamic petrophysical study of MC2 cores (K, zeta, ...)

BOREHOLE GEOPHYSCIS (WP3)

MB1 **Mop**(PhP)+ETH	Methodology; borehole geophysical approach for hydrogeophysics in reefal carbonates based on MC2 data.
MB2 **Mop**(PG)+ETH	Methodology – image analysis for mesoscale porosity analysis.
MB3 **Mop**(HB)+VU	Acoustic properties of reefal carbonates at Campos.
MB4 **Mop**(YMS)+ETH	Porosity structure of the reef at the Campos site (including comparison of logging techniques, core data and image analysis).
MB5 **Mop**(YMS)+ETH +Aix	Sedimentological facies and paleoenvironments of the Campos reefal carbonates from natural spectral gamma and core analyses.
MB6 **ETH**(DJ)+Mop	Mesoscopic porosity structure of a Miocene reefal carbonate, Mallorca (Spain).
MB7 **ETH**(DJ)+Mop	Downhole characterisation of fractured rhetian carbonates drilled near Pollenca, Mallorca (Spain).
MB8 **Mop**(YMS)+ETH +Aix+VU	Sedimentological facies and paleoenvironments of the Miocene carbonates platform from natural spectral gamma.

HYDROGEOPHYSICS (WP3-5)

MH1 **Mop**(TLB)	Detailed flowmeters study in MC2, MC8, MC9, S17
MH2 **Mop**(PhG)	CoFIS tracer experiments
MH3 **Mop**(GL)	Theoretical paper
MH4 **Mop**(PhP)+ALT	MUSET used as flowmeter

<u>DOWNHOLE MONITORING</u> (WP8-9)

MM1 **ETH**(NvM)	Spectroscopic analysis of water level data from a reefal carbonate aquifer, Mallorca (Spain).
MM2 **Mop**(PhP)+Pau	Electrical monitoring of tracer injection during SWIW with fresh water (calibrated with induction log in nearby hole).
MM3 **Mop**(PhP)+Pau	Electrical monitoring of seasonal changes in water table and structure of the transition zone between fresh and sea water.

••• *<u>Papers realted to the Ploemeur experimental site (Brittany)</u>*

<u>GEOLOGY</u> (WP1)

PG1 **Bham**	Site description

<u>PETROPHYSICS</u> (WP4)

PP1 **OvU**+Mop	Pore space structure with emphasis on transmissivity (B1 cores)
PP2 **OvU**+Mop	Rock matrix heterogeneity and anisotropy (B1 cores)
PP3 **Mop**(AB)+OvU	Petrophysical characterization of B1 cores (Vp, Ø, res, ...)
PP4 **Mop**(AB)+OvU	Dynamic petrophysical characterization of B1 cores (K, zeta, ...)

<u>BOREHOLE GEOPHYSCIS</u> (WP3)

PB1 **Mop**(PhP)+Bham	Methodology; borehole geophysical approach for hydrogeophysics studies in basement
PB2 **Mop**(PG)	Methodology – image analysis for fracture identification and lithological determination
PB3 **Mop**(AB)	Petrophysical properties of basement rocks from Ploemeur
PB4 **Mop**(AB)+Bham	Structural analysis (fractures, faults and schistosity) at Ploemeur
PB5 **Mop**(AB)+ALT	Spontaneous electrical potential in fractured granitic basement
PB6 **Mop**(?)+VU	Acoustic properties in fractured granitic basement

<u>HYDROGEOPHYSICS</u> (WP3_5)

PH1 **Mop**(TLB)	Detailed flowmeter study (including BHAM).
PH2 **Mop**(PhG)	CoFIS tracer experiments (including BHAM).
PH3 **Bham**(MR)	Discrete modeling of flow at site scale (including Mop)

<u>MONITORING</u> (WP7-9)

PM1	Bham	Influence of tides

••• *Papers realted to the Lavalette (Montpellier) site (WP5)*

LH1	**Mop**(PhG)	CoFIS tracer experiments.
LB1	**Mop**(FE)	Petrophysical and geophysical description of the site.

••• *Papers realted to the Maguelone (Montpellier) coastal site (WP9)*

CM1	**Mop**(PhP)+Pau	Downhole monitoring of electrical resistivity
CG1	**Mop**(FB)	Sedimentological structure of the MAG1 hole
CP1	**Mop**(CL)	Physical properties of sediments from the MAG1 hole

••• *Papers realted to acoustics studies related to DopTV (WP6)*

AL1	**LMA**	Doppler acoustic velocimetry of fluid flow from borehole fractures
AL2	**LMA**	Analysis of fluid flow from a borehole fracture with a pulsed Doppler system

***(*)** Acronyms used in the previous text* **:**

ALIANCE PARTNERS

Mop	CNRS - University of Montpellier (France)
ETH	ETH Zurich (Switzerland)
Bham	University of Birmingham (UK)
OvU	University of Oviedo (Spain)
LMA	CNRS, Marseille (France)
ALT	ALT (Luxembourg)
VU	Free University of Amsterdam (Holland)
Aix	CNRS - CEREGE, Aix-en-Provence (France)
Pau	University of Pau (France)
Ren	University of Rennes (France)
MFr	MEDIAS France, Toulouse (France)

PAPER LEADERS

PhP	Philippe Pezard
PhG	Philippe Gouze
SG	Stéphanie Gautier
GL	Gerard Lods
TLB	Tanguy Le Borgne
HB	Heindrik Braaksma
PG	Philippe Gaillot
FE	Florence Einaudi
CL	Christine Lauer
FB	Frédéric Bouchette
AB	Akram Belghoul
YMS	Yves Maria-Sube
DJ	David Jaeggi
NvM	Nathalie van Meir
SL	Simon Loew
MH	Martin Herfort
MM	Modesto Montoto
FM	Felix Mateos
JPS	Jean-Pierre Sessarego
RG	Régine Guillermin
TM	Thierry Monnier
MC	Marc Francius
MR	Mick Riley
PE	Paul Ellis
RG	Richard Gresswell

REFERENCES

ALIANCE scientific team, 2003. "2002 Scientific Report".

ALIANCE scientific team, 2004. "2003 Scientific Report".

Allan J. R. et Matthews R. K., 1977. Carbon and oxygen isotopes as diagenetic and stratigraphic tools: Surface and subsurface data, Barbados, West Indies. *Geol.*, 5, 16-20.

Allan J. R. et Matthews R. K., 1982. Isotopic signatures associated with early meteoric diagenesis. *Sedimentology*, 29, p. 797-817.

Angelsen B.A.J., 1980. A theoretical study of the scattering of ultrasound from blood, IEEE Trans. Biomed. Eng., BME-27: 61-67.

Batchelor G. K. and A.E. Gill, 1962. Analysis of the stability of axisymmetric jets, J. Fluid Mech., 14:529.

Bathurst R., 1975. Carbonate sediments and their diagenesis. *Developments in sedimentology* n°12, 658 p. Elsevier, New York.

Beavers G.S. and T.A. Wilson, 1970. Vortex growth in jets, J. Fluid Mech., 44:97-112.

Bonnefous O. and P. Pesqué, 1987. Time domain formulation of pulse-Doppler ultrasound and blood velocity estimationby cross correlation, Ultrason. Imag., 9:73-85, 1986.

Brand U. et Veizer J., 1981. Chemical diagenesis of a multicomponent carbonate system -2: stable isotopes. *Jounr. Sedim. Petrol.*, 51, p. 987-997.

Cohen J. and I. Wignansky, 1980. The evolution of instabilities in the axisymmetric jet. Part I. The linear growth of disturbances near the nozzle, J. Fluid Mech., 176..

Crow S.C. and F. H. Champagne, F. H., 1971. Orderly structure in jet turbulence, J. Fluid Mech., 48.

Ebren P., 1996. Impact des variations rapides du niveau marin sur le développement des atolls au quaternaire: Mururoa (Polynésie Française) – Dynamique récifale et diagenèse des carbonates. *Thèse/Doct. Univ. Aix-Marseille I.* p. 118-143.

Ferrara K.W. and R.V. Algazi, 1991a. A new wideband spread target maximum likelihood estimator for blood velocity estimation - Part I: Theory, IEEE Trans. Ultrason. Ferroelect. Freq. Cont., 38(1): 1-16.

Ferrara K.W. and R.V. Algazi, R.V. 1991b. A new wideband spread target maximum likelihood estimator for blood velocity estimation - Part II: Evaluation of estimators with experimental data; IEEE Trans. Ultrason. Ferroelect. Freq. Cont., 38(1):17-26.

Friedel, S., and Maurer, H.R., 2004, Single-hole geoelectrical tomography for characterization of a coastal aquifer. Exp. Abstracts SEG meeting, submitted.

Guillermin R. and J-P Sessarego, 2004. ALIANCE project – WP6 Report.

Hein I.A. and W.D. O'Brien, W.D., 1992. A flexible blood flow phantom capable of independently producing constant and pulsatile flow with a predictable spatial flow profile for ultrasound flow measurment validation, IEEE Trans. Biomed. Eng., 39:1111-1122.

Hess A.E., 1986. Identifying hydraulically conductive fractures with a slow velocity borehole flowmeter, Canadian Geotechnical Journal, 23:69-78.

Jensen J.A., J.A., 1993. Implementation of ultrasound time-domain cross-correlation blood velocity estimators, IEEE Trans. Biomed. Eng., 40, no 5:468-474.

Jensen J.A., 1994. Artifacts in blood velocity estimation using ultrasound and cross-correlation, Med. Biol. Eng. Comp., 32, no 4:165-170.

Kearl P.M., N.E. Korte, M. Stites and J. Baker, 1994. Field comparison of micropurging vs. traditional ground water sampling, *Ground Water Monitor. and Remed.*, 14:183-190.

Kerfoot W.B., G. Beaulieu and L. Kiely, 1991. Direct-reading borehole flowmeter results in field applications, Proceedings of the Fifth National Outdoor Action Conference on Aquifer Restoration, 1073-1084.

Kerfoot W.B., 1982. Comparison of 2-D and 3-D ground-flowmeter probes in fully-penetrating monitoring wells, Proceedings of the Second National Symposium on Aquifer Restoration and Ground Water Monitoring, 264-268.

Kerfoot W.B., 1990. Independent verification of heat pulse groundwater flowmeter results through long term observation and tracer tests on Superfund sites, Hydrocarbon Contaminated Soils, V:37-49.

Lai X., H. Torp, H. and K. Kristoffersen, K., 1997. An extended autocorrelation method for estimation of blood velocity, IEEE Trans. Ultrason. Ferroelect. Freq. Cont., 44(6):1332-1342.

Leeuwen G.H., A.P.G. Hoeks and R.S. Reneman, R.S., 1986. Simulation of real-time frequency estimators for pulsed Doppler systems, Ultrason. Imag., 8:252-271.

Loew S., C.F. Tsang, F. Hale and P. Hufschmied, P., 1991. The application of moment methods to the analysis of fluid electrical conductivity logs in boreholes, NAGRA Project LBL-28809.

Lohmann K. C., 1998. Geochemical patterns of meteoric diagenesis systems and their applications to studies of paleokarst. N. P. James and P. W. Choquette Eds, *Paleokarst*, Springer, New York, p. 58-80.

Loupas T., R.B. Peterson and R.W. Gill, R.W., 1992. Experimental evaluation of velocity and power estimation for ultrasound blood flow imaging, by means of a two-dimensional autocorrelation approach, IEEE Trans. Ultrason. Ferroelect. Freq. Cont., 42(4):689-699.

Loupas T., J.E. Powers and R.W. Gill, R.W., 1992. An axial velocity estimator for ultrasound blood flow imaging, based on a full evaluation of the Doppler equations by means of a two-dimensional autocorrelation approach, IEEE Trans. Ultrason. Ferroelect. Freq. Cont., 42(4):671-687.

Mattingly G.E. and C.C. Chang, 1974. Unstable waves on a axisymmetric jet column, J. Fluid Mech., 65,.

Meyers W. J. and Lohmann K. C., 1985. Isotope geochemistry of regionally extensive calcite cement zones and marine components in Mississippian limestones, New Mexico., Schneidermann an Harris Eds., *Carbonate Cements*, S.E.P.M. Special Publication, n°36, p.223-239.

Michalke A., 1984. Survey on jet instability theory, Prog. Aerospace Sci., 21.

Michalke A., 1965. On spatially growing disturbances in an inviscid shear layer, J. Fluid Mech., 23.

Mollendorf J.C. and B. Gebhart, 1973. An experimental and numerical study of the viscous stability of a round laminar vertical jet with and without buoyancy for symmetric and asymmetric disturbance, J. Fluid Mech., 61.

Molz F.J. and S.C. Young, S.C., 1993. Development and application of borehole flowmeters for environmental assessment, The Log Analyst, 34:13-23.

Molz F.J., G.K. Bowman, S.C. Young and W.R. Waldrop, 1994. Borehole flowmeters - Field application and data analysis, Journal of Hydrology, 163:347-371.

Monnier T., R. Guillermin and J.P. Sessarego, 2003a. Doppler Acoustic velocimetry of fluid flow from borehole factures, ALIANCE Project– WP6 Report.

Monnier T., R. Guillermin, J.P. Sessarego and P. Sanchez, P, 2003b. Doppler Acoustic velocimetry of fluid flow from borehole factures, WCU.

Morris P., 1976. The spatial viscous instability of axisymmetric jets, J. Fluid Mech., 77.

Newhouse M.W. and R.T. Hanson, 2000. Application of three-dimensional borehole flow measurements to the analysis of seawater intrusion and barrier injection systems, Proceed. The Minerals and Geological Logging Society.

Paillet F., 1998. Flow modeling and permeability estimation using borehole flow logs in heterogeneous fractured formations, Water Resources Research, 34:997–1010.

Paillet F., R. Crowder and A. Hess, 1994a. High resolution flowmeter logging. Part 1: Flowmeter techniques and equipment development, Proceedings of the Symposium on the Application of Geophysics to Engineering and Environmental Problems, 361-379.

Paillet F., R. Crowder and A. Hess, 1994High resolution flowmeter logging. Part 2: Borehole applications with the heat-pulse flowmeter, Proceedings of the Symposium on the Application of Geophysics to Engineering and Environmental Problems, 381-404.

Plaschko, P., 1979. Helical instabilities of slowly divergent jets, J. Fluid Mech., 92.

Pomar, L., 1993, High-resolution sequence stratigraphy in prograding carbonates: Application to seismic interpretation, in R. Loucks and R. Sarg. eds., Recent advances and applications of carbonate sequence stratigraphy: Tulsa. AAPG Memoir 57, p. 389-407.

Pomar. L. W.C. Ward. and D.G. Green, 1996, Upper Miocene reef complex of the Llucmajor platform. Mallorca. Spain. In E.K. Franseen. M. Esteban. W.C. Ward. and J.M. Rouchy. Eds., Models for carbonate stratigraphy from Miocene reef complexes of Mediterranean regions: SEPM Concepts in Sedimentology and Paleontology 5, p. 191-225.

Quinn T. M., 1991. Meteoric diagenesis of Plio-Pleistocene limestones at Enewetak atoll. *Journ. Sedim. Petrol.*, 61, p. 681-703.

Reynolds A.J., 1962. Observation of a liquid-into-liquid jet, J. Fluid Mech., 14.

Saito J. and H. Niitsuma, 2001. Development of a Doppler acoustic imaging system for borehole wall to evaluate fluid flow distribution around subsurfcace fractures, Jpn. J. Appl. Phys., 40: 3558-3561.

Saller A. H. and Moore C. H., 1991. Geochemistry of meteoric calcite cements in some Pleistocene limestones. *Sedimentology*, 38, p. 601-621.

Sato H. 1960. The instability and transition of a two-dimensional jet, J. Fluid Mech., 1:53-80.

SonTek, Inc., Modified ADV for 3D velocity measurements in boreholes, Final project report: U.S. Geological Survey Contract Number 1434-95-C- 40232, 39-404, 1996.

Tsang C.F., P. Hufschmied and F.V. Hale, 1990. Determination of fracture inflow parameters with a borehole fluid conductivity logging method, Water Resources Research, 26:561-578.

Touchard, 1999. Caractérisation hydrogéologique d'un aquifère fracturé; Site de Ploemeur, Morbihan. Thèse de 3ème cycle. Géosciences Rennes.

Viilu A., 1962. An experimental determination of the minimum Reynolds number for instability in a free jet, J. Appl. Mech., 29.

Wilson J.T. et al., 2001. An evaluation of borehole flowmeters used to measure horizontal ground-water flow in limestones of Indiana, Kentucky, and Tenessee, US Geological Survey Water-Ressources Investigations Report.

Young S.C., H.S. Pearson, G.K. Moore and R.B. Clapp, R.B., 1991. Application of the electromagnetic borehole flowmeter technique at the Oak Ridge Laboratory, Report WR28-1-900-247.